INVESTIGATION OF Te FOR DETECTION OF PULSED CO_2 LASERS

INVESTIGATION OF TELLURIUM FOR THE DETECTION OF PULSED CO_2 LASER RADIATION

by

Gennadijs Ribakovs, B.Eng., M.Eng.
Department of Electrical Engineering

INVESTIGATION OF TELLURIUM FOR THE DETECTION OF PULSED CO_2 LASER RADIATION

by

Gennadijs Ribakovs, B.Eng., M.Eng.

A Thesis submitted to the Faculty of Graduate Studies and Research in partial fulfillment of the requirements for the degree of Doctor of Philosophy

Department of Electrical Engineering
McGill University
Montreal, Canada

June, 1976

ABSTRACT

Comprehensive measurements are carried out in order to obtain and interpret all tensor components necessary to describe the fast emfs induced in intrinsic and extrinsic single crystal tellurium samples exposed to TEA CO_2 laser radiation in the temperature range between 115 to 300 K. Three distinct mechanisms for the generation of the fast signals are identified; namely, the photon drag effect, a carrier dependent optical rectification effect, and, a spurious signal predominant only at low temperatures in structurally imperfect crystals.

A theory for the photon drag effect based on a detailed microscopic discussion is developed and is found to be consistent with the obtained experimental results.

Of the different mechanisms discussed for the optical rectification effect, the non-linear acoustoelectric effect is proposed as the likely source.

Finally, the performance of tellurium detectors is shown to be superior in general to commercially available devices when ultrafast response times are desired.

EXTRAIT

Des mesures détaillées ont été effectuées, pour obtenir et interpréter tous les éléments tensoriels nécessaires pour décrire les forces életromotrices induites dans un cristal de tellure exposé à la radiation provenant d'un laser à CO_2-TEA, entre 115 et 300 K. Trois mécanismes distincts ont été indentifiés pour expliquer les signaux obtenus; un effet de redressement optique dépendant des porteurs de charges et un signal qui apparait aux basses températures et qui resulte des imperfections cristallines.

Une théorie conforme aux résultats expérimentaux, basée sur des considérations microscopiques détaillées a été dévelopée pour expliquer l'effet du train de photons.

Après avoir discuté plusieurs mécanismes pour expliquer l'effet de redressement optique, l'effet acoustoélectrique non linéaire est proposé comme la source la plus probable de cet effet.

Finalement les caractéristiques des detecteurs à tellure sont montrées être en général supérieures à celles de ceux commercialement disponibles dans le cas des signaux à très hautes fréquences.

ACKNOWLEDGEMENTS

The author wishes to express his appreciation to Dr. A.A. Gundjian for his guidance and assistance throughout the period of research.

Thanks are also due to Dr. E. Adler and Dr. G. Farnell for their participation in enlightening discussions and suggestions.

The efficient and fine typing of this thesis by Mrs. W. Aird is much appreciated.

Acknowledgements are due to the Quebec Department of Education and to the National Research Council of Canada for their financial support.

Finally, the author is ever grateful to his parents and wife for maintaining their patience and understanding during his years of academic study.

TABLE OF CONTENTS

LIST OF ILLUSTRATIONS

CHAPTER I

INTRODUCTION

One of the few laser systems devised since 1960 which is sufficiently efficient and powerful to be of technological importance is the CO_2 laser which operates at radiation wavelengths around 10.6 μm. In particular, the TEA (Transversely-Excited-Atmospheric) type of CO_2 laser {1} is capable of delivering short duration pulses with multi-megawatt peak-powers; even higher power versions of these lasers are now being developed for the prospect of initiating nuclear fusion.

With the advent of such lasers, the need arose for a simply manufactured, fast response, robust, and convenient room temperature detector. Due to the lack of strong sources, infrared detectors in the past were required to be of high sensitivity, that resulted in the necessity of cooling down to liquid helium or at best liquid nitrogen temperatures; normally these detectors have, in addition, limited response times. Within recent years, two types of simple and rugged fast room temperature detectors have been developed and are now in widespread use for the measurement of sub-microsecond CO_2 laser pulses: the pyroelectric detector generates an electrical signal when its spontaneous electric polarization is altered by the change in the crystal temperature upon absorption of the laser power; a

second type and fundamentally faster detector was developed utilizing the photon drag effect in germanium {2}, {3}, which involves the transfer of the photon momentum from the radiation in the laser beam to the charge carriers in this semiconductor; a fundamental consideration for an efficient photon drag device is the radiation absorption per free carrier, i.e., the absorption cross-section, at the wavelength of interest.

At the CO_2 laser radiation wavelength, tellurium from all known semiconductors, possesses the highest value for the absorption cross-section with a magnitude which is specifically fifty percent larger than that of germanium. This large absorption cross-section in tellurium is illustrated by the pronounced peak in the absorption spectrum of this material centered around 11 μ, resulting from the intervalence band transitions. Thus it was deemed natural to investigate this material as a potential CO_2 laser photon drag detector. This conclusion was confirmed concurrently by Moss {4}.

In the process of measuring and analysing the signals generated in tellurium by the radiation from a TEA CO_2 laser, additional emfs, which could not be attributed to the photon drag effect were observed.

This work constitutes a theoretical and experimental analysis of the different fast signals generated when

tellurium samples are illuminated with high power, short duration laser radiation pulses of 10.6 μ wavelength. The experimental results were obtained from measurements performed on tellurium samples with appropriate geometries in the temperature range of 300 K to 115 K. The different signals are identified according to their tensorial behaviour and analysed theoretically in terms of proposed physical mechanisms from both a phenomenological and microscopic point of view.

CHAPTER II

STATE OF THE ART ON PULSED CO_2 LASER RADIATION DETECTORS

II 1.0 Introduction

Although there exist many types of infrared detectors, this chapter presents a brief description of only those devices which have found commercial use in the detection of pulsed CO_2 laser radiation. A comprehensive review of all types of infrared detectors can be found in the report by Putley {5}. Specifically, the following devices are described in this chapter according to their physical mechanism of operation and performance characteristics.

a) Photon detectors

1. Intrinsic
2. Extrinsic

b) Pyroelectric

c) Photon drag

II 2.0 The Performance Parameters of Detectors

The performance of radiation detectors is conventionally described by the specification of the following parameters.

1) The Responsivity $R_v = \Delta V/\Delta W$, in volts/watts, where ΔV is the output voltage produced by a change ΔW in the incident radiation power.

2) The Noise Equivalent Power (NEP), in watts/$Hz^{1/2}$, which is the signal power required to give an output voltage equal to the noise output from the detecting system within unity bandwidth.

3) The Specific Detectivity D*, which is defined as the reciprocal of the NEP times the square root of the area A of the detector element, i.e., $D^* = NEP^{-1} \times A^{1/2}$.

4) The Response Time τ, which is a measure of the time necessary for the detector to react to an instantaneous change in the incident power flux.

II 3.0 Characteristics of Typical Detectors

II 3.1 Photon Detectors

II 3.1.1 Extrinsic

The first photon detectors useful at 10 μ employed the photoexcitation of carriers from impurity centers in semiconductors, such as Cu, Au, or Hg in Ge. In order to

avoid saturation due to thermal energy excitation, these detectors must operate at temperatures in the range 4-30 K which makes them inconvenient and bulky for industrial use.

Typical responsivities are of the order of 10 V/W with specific detectivity $D^* = 2 \times 10^{10}$ cm W^{-1} $Hz^{1/2}$. Usually the response time of such detectors is in the order of 100 ns. Specifically prepared, heavily compensated materials have, however, exhibited sub-nanosecond times of response. These detectors have minute element areas in the order of 10^{-4} cm^2 in order to achieve the quoted responsivities and response times.

II 3.1.2 Intrinsic

For the detection of radiation in the 8-13 μ spectrum, the previous extrinsic detectors are recently being replaced by new materials whose intrinsic band gaps are made small enough for the direct excitations of the electrons by these long radiation wavelengths. The materials presently being used are HgCdTe and PbSnTe in which the desired energy band separations are obtained by varying the Hg/Cd or Pb/Sn proportions. HgCdTe is used to manufacture both photoconductive and photovoltaic devices whilst PbSnTe is only employed to make photovoltaic detectors.

These detectors normally operate at 77 K; they have responsivities in the order of a few hundred V/W and

specific detectivities in the order of 10^{10} cm W^{-1} $Hz^{1/2}$ with typical response times of the faster photovoltaic devices of 50 ns. Special devices have also been fabricated to achieve approximately 1 ns response times. These intrinsic photodetectors have sample elements in the order of 10^{-4} cm^2; they are presently extremely expensive with prices in excess of $17,000 for the ultra-fast models.

II 3.2 Pyroelectric Detectors

Pyroelectric crystals such as TGS, SBN, and $LiTaO_3$ are found to be useful room temperature detectors of chopped or pulsed radiation over a wide range of the wavelength spectrum; they are in common use for the detection of pulsed laser radiation as they are capable of high frequency response with relatively large responsivity. The pyroelectric detection of radiation takes place in the following manner:

a) Radiation is absorbed and is converted into heat, which increases the temperature of the crystal.

b) The change in temperature alters the lattice spacings within the crystal, producing a change in the existing spontaneous electric polarization.

c) If electrodes are applied to the crystal surfaces normal to the axis of this polarization, a current is generated, through an external circuit, to balance the

change of the polarization effect. This current is proportional to the rate of change of temperature.

d) This current is allowed to produce a voltage change across an appropriate load resistor; the electrical bandwidth is determined by this load resistance and the effective capacitance of the detector element. Decreasing the load resistance thus increases the bandwidth, but also decreases the responsivity which is typically of the order of 7×10^{-6} V/W for the minimum rise time of 500 ps. The NEP under these conditions is approximately 10^{-1} W/Hz$^{1/2}$.

These pyroelectric detectors have, however, two main disadvantages which limit their use in the measurement of high power short duration laser pulses: they are normally limited to a maximum energy of 1 millijoule per radiation pulse in order to prevent thermal damage of the crystal element; secondly and more importantly, as these pyroelectric crystals also exhibit piezoelectricity, the detectors give a somewhat distorted reproduction of submicrosecond pulses as a result of several MHz frequency oscillatory signals produced by piezoelectric resonances of the detector elements at the end of the radiation pulse.

II 3.3 The Photon Drag Detector

The photon drag effect, which is being used for detecting and monitoring high power CO_2 lasers at room

temperature, results from the interaction between photons and free carriers such as conduction electrons and holes in a semiconductor. This mechanism consists essentially of the transfer of momentum from the photons to the free charge carriers consistent with the principle of conservation of energy and momentum during the interaction process. A laser beam will, therefore, impart in its direction of propagation a momentum component to the free carriers, resulting in a flow of an electric current in a closed electrical circuit or the establishment of a voltage under open circuit conditions; it is clear that the electrical signals generated through this mechanism have a fast speed of response with a fundamental upper limit determined by the free carrier momentum scattering time which is normally of the order 10^{-13}s. A detailed analysis of the photon drag effect will be presented in Chapter VII.

The photon drag effect in germanium has been first utilized in 1970 {2} for the detection of high power pulsed CO_2 laser radiation with a maximum detector responsivity of the order of 1 μV/W and a corresponding D* of $\cdot 10^3$ cm W^{-1} $Hz^{1/2}$; the response times are better than 0.1 ns and are limited by the R-C time constants of the electrical circuit. Appropriately prepared devices exhibit linearity with respect to incident power densities up to 20 MW cm^{-2}; the damage threshold levels for germanium surfaces are in excess of 100 MW cm^{-2}.

In order to make a practical detector, it is necessary to achieve near total absorption of the incident radiation with the lowest possible carrier concentration, as will be shown in Section VII 3.0; in order to realize this condition in a material of reasonable length such as a centimeter, an absorption coefficient $K \geq 2\ cm^{-1}$ is needed. An actual figure of comparison for different materials in this respect, is the absorption coefficient per carrier β, such that materials of highest β are the most attractive for photon drag detectors.

II 4.0 Conclusions

In comparing the different detectors presented in this chapter, it is apparent that only the pyroelectric and photon drag detectors are suitable for the detection of high power pulsed CO_2 lasers at room temperature. Of the latter two, the photon drag device is considered superior since its otherwise low responsivity becomes comparable to that of the pyroelectric detector when the measurement of subnanosecond radiation pulses is involved. On the other hand, the photon drag detector has the advantage of being capable of handling much higher laser pulse energies. Finally, it gives a true replica of the laser output without the annoying pulse distortions caused by the electromechanical resonances which occur in the response of the pyroelectric detectors.

It was stated in the previous section that materials possessing a large absorption cross-section β are the most attractive for photon drag detectors. Since tellurium was found to have a β, which is the highest of all known semiconductors, specifically equal to 90 which is fifty percent higher than that of germanium, and an absorption coefficient $\approx 5\ cm^{-1}$ at 10.6μ, it was decided to investigate the properties of tellurium as a promising and interesting photon drag material for the purpose of detecting TEA CO_2 laser pulses.

CHAPTER III

PROPERTIES OF TELLURIUM

III 1.0 Introduction

Tellurium, a member of the Group VI A of the periodic table of the elements, was discovered in 1782 from ores mined in the gold district of Transylvania by F.J. Mueller von Reichenstein, an Austrian chemist. Mineralogically, native tellurium crystals are only observed in small quantities; the largest commercial source of tellurium mineralization is thus found associated with copper, copper-nickel, lead sulfide ores in the form of tellurides such as tetradymite - Bi_2Te_2S, hessite - Ag_2Te, sylvanite - $AuAgTe_4$, and nagyagate - $Au\ (Pb, Sb, Fe)_3(TeS)_{11}$.

Since its discovery, tellurium has found numerous commercial applications as an additive element. It is added to steel and copper for improving machinability, to lead as a strengthening agent, and to iron to increase its malleability. Tellurium is also used in the formulation of such semiconductor compounds as bismuth telluride and lead telluride for producing thermoelectric devices. Since for the above applications, crystalline tellurium is not required, good quality single crystals of this material are at present only found in a few institutions which grow a limited number for their own research purposes.

III 2.0 Crystalline Structures

Single crystal tellurium has a hexagonal lattice, Figure 1, with atoms covalently held in helical chains spiraling around the [0001] direction or c-axis. Every third atom is directly above another atom in the same chain, Figure 1, so that a chain appears triangular on looking along the c-axis. Chains are stacked with hexagonal symmetry, each atom having four next-nearest neighbours in adjacent chains. The binding between the chains is weak and conventionally assumed to be mainly Van der Waals type, thus, tellurium cleaves easily on any of the six planes equivalent to $(10\bar{1}0)$, Figure 1. The tellurium single crystal structure is considered to belong to the trigonal class with 32 point group symmetry.

III 3.0 Mechanical Properties

Some important physical constants of tellurium are shown in Table 1.

Tellurium is a relatively soft and brittle material which can be damaged easily. During the study of the properties of perfect crystals, extreme caution must be taken in order to avoid dislocations which can be introduced, particularly on the surface, through the application of even a small amount of stress; it is for this reason that sample preparation entails great care in order to eliminate such

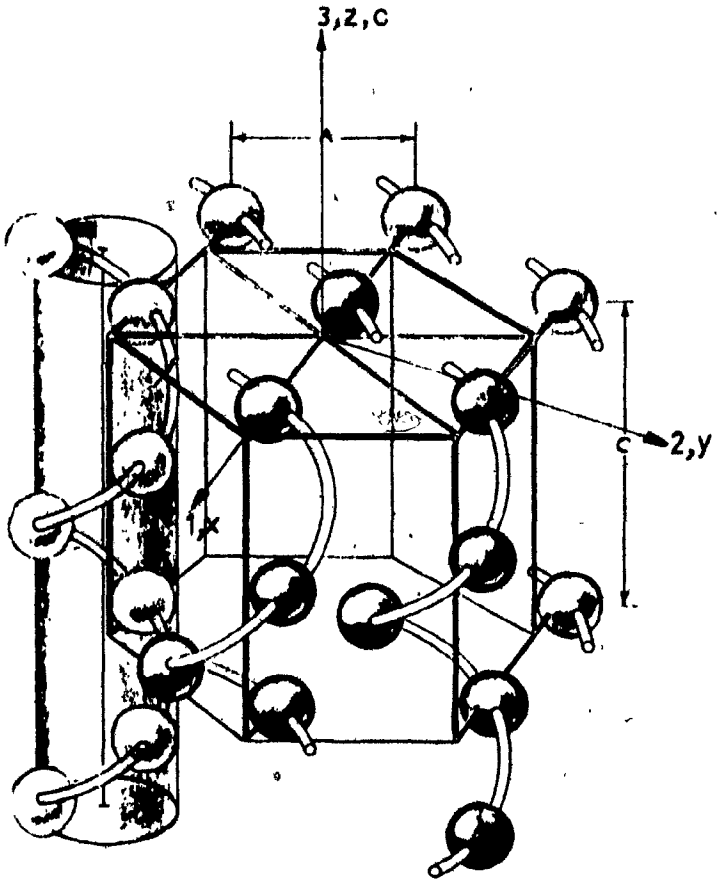

Figure 1. The Atomic Arrangement in Tellurium

From Blakemore et al., "Progress in Semiconductors," Vol. 6. (Wiley, 1962). Each atom makes covalent bonds with its nearest neighbours up and down the spiral chain. Interchain forces are weak. The sides of the hexagon are the (10$\bar{1}$0) equivalent planes.

TABLE 1

Physical Constants of Tellurium {6}

Property	Value
Atomic number	52
Atomic weight	127.60
Lattice constant A	4.4572 Å
Lattice constant C	5.93 Å
Density	6.245 gm $-cm^{-3}$ @ 25°C
Normal melting point	452°C
Normal boiling point	990°C
Latent heat of vaporization	106.7 cal/gm
Latent heat of fusion	20.5 cal/gm
Linear expansivity at 300°K:	$\|\|c$, -2.5×10^{-6} deg^{-1}
	$\perp c$, 30×10^{-6} deg^{-1}
Heat capacity at constant pressure	6.160 cal/gm-atom-deg
Mean thermal conductivity	$\kappa \approx 0.038$ watt-cm^{-1} deg^{-1}
Static dielectric constant	$\varepsilon_{\|\|} = 38.6$
	$\varepsilon_{\perp} = 22.7$

dislocations, consequently sawing, grinding, lapping, and even optical polishing are usually prohibited. Chemical etch cutting and polishing are normally employed to minimize bulk and surface damage.

III 4.0 Electric Conduction

(a) "Good" crystals

The electric resistivity for structurally perfect single crystal highest purity tellurium is about 0.5 Ω-cm at room temperature; mechanically heavily worked surface layers exhibit increased conductivity as dislocations tend to act as acceptor type levels, thus increasing the number of hole free carriers. In fact, it has been shown {7} that a lower limit of the hole density, $5 \times 10^{13} \rightarrow 10^{14}$ cm^{-3} exists which is related to the thermal breaking of covalent bonds at dislocations during the growth of single crystals; thus, while pure tellurium is intrinsic at room temperature with an intrinsic carrier concentration of 4.9×10^{15} cm^{-3} {8}, it automatically becomes p-type at lower temperatures. A characteristic feature of extrinsic tellurium is that it is always found to be p-type regardless of the impurity dopant present {8}.

The crystalline structure described in Section III 2.0 results in anisotropic physical properties of crystalline tellurium; the mobility of free carriers which is described

by a second rank tensor has two independent components corresponding to different mobilities parallel and perpendicular to the c-axis. At room temperature in pure crystals with the minimum of lattice imperfections, the electron and hole mobilities parallel to the c-direction are respectively approximately 2430 and 1321 $cm^2\ V^{-1}\ s^{-1}$ {45}, whereas these values are reduced by about a factor of 2 in directions perpendicular to the c-axis.

(b) Effect of imperfections

Published values of the hole mobility in pure tellurium samples are found to vary by as much as an order of magnitude. This discrepancy is attributed to the degree of crystal perfection, as the mobility is affected by the additional scattering processes at the crystal lattice defect and dislocation centers {9}, {10}, {11}. Experimentally it is shown that with the removal of imperfections by the annealing of tellurium samples, the mobility is increased substantially {12}.

(c) Nonlinearity

Tellurium is a piezoelectric semiconductor exhibiting strong deviations from ohmic behaviour when the drift velocity of carriers exceeds the velocity of sound {13}. The onset of the nonohmic behaviour is due to the evolution of acoustoelectric domains caused by the interaction of

electrons with phonons via the piezoelectric coupling {14}, {15}.

III 5.0 Optical Properties

This section presents those optical characteristics of tellurium which are relevant to the present work.

III 5.1 Dielectric Properties

It is known that the electric displacement $\vec{D}$ in a given material is related to the electric field $\vec{E}$ through the dielectric tensor $[\varepsilon]$, such that

$$\vec{D} = [\varepsilon]\ \vec{E} \qquad (1)$$

When nonlinearity is taken into account, the dielectric tensor coefficients are considered to be dependent on the electric field; expression (2) is then obtained, where the spatial components of $\vec{D}$ are related to those of $\vec{E}$ in terms of ε expressed as a power series in E;

$$D_i = \varepsilon_o\, \varepsilon_{ij}\, E_j + d_{ijk}\, E_j\, E_k + \ldots \qquad (2)$$

where ε_{ij} - are the second rank tensor components of the linear dielectric constant;

ε_o - is the dielectric coefficient of free space,

and d_{ijk} - are the third rank tensor components of the so called nonlinear optical coefficient.

III 5.1.1 The linear dielectric constant

The trigonal symmetry of tellurium, as described in Section III 2.0, dictates that the matrix representing the linear dielectric constant second rank tensor components, expressed with respect to the principal axes, consists of three diagonal terms where the two elements, associated with the directions perpendicular to the c-axis, are equal, see Figure (2a); the third element relates the electric displacement and field components parallel to the c-axis which is called the optical axis of tellurium. This particular type of anisotropy characterizes the single crystal tellurium as being uniaxial and birefringent. It is also found that the dielectric constant is appreciably frequency dependent in the optical range and, therefore, tellurium is said to be a dispersive medium.

The refractive indices n_{ii}, defined as the square root of the dielectric constants ε_{ii}, are relatively large in tellurium. At 10.6 μ wavelength, in directions perpendicular to the c-axis, the value of $\sqrt{\varepsilon_\perp} = n = 4.79$, while in a direction parallel to the c-axis $\sqrt{\varepsilon_\parallel} = n = 6.25$. It follows that the magnitude of the reflection coefficient R at an air-tellurium interface is given in terms of the refractive index as

$$R = \left(\frac{n-1}{n+1} \right)^2 \qquad (3)$$

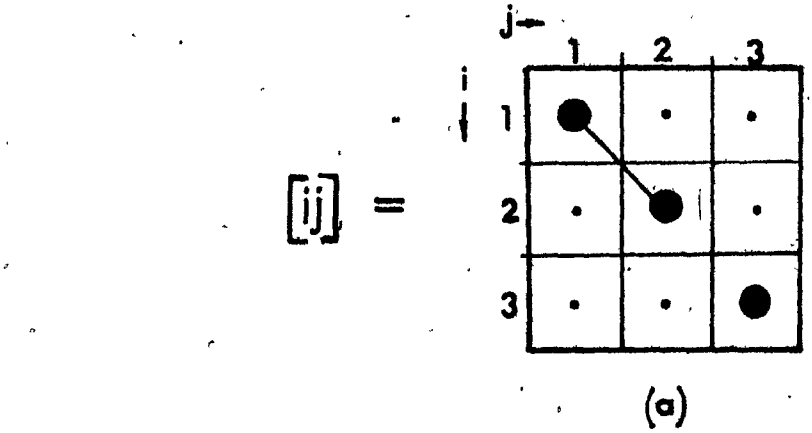

(a)

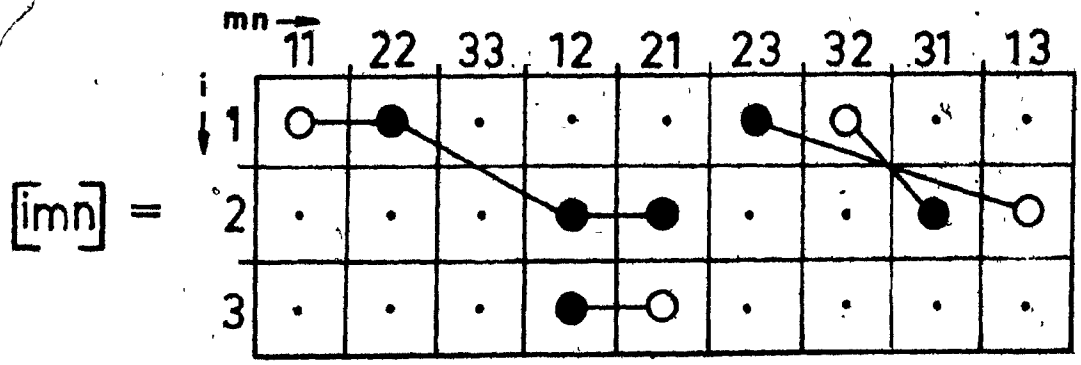

elements equal by symmetry

elements opposite in sign by symmetry

elements zero by symmetry

Figure 2. Finite tensor elements for tellurium

a) second rank tensor coefficients
b) third rank tensor coefficients

which takes the values of 0.43 and 0.53 respectively for the polarizations perpendicular and parallel to the c. or optical axis.

III 5.1.2 The non-linear dielectric property

Crystals of tellurium are of the trigonal class with 32 (D_2) point group symmetry and belong to the $P3_{1,2}2$ space group (Hermann - Mangain notation {16}) which correspondingly assures an absence of inversion symmetry necessary for the nonlinear third rank tensor optical phenomena to exist. Tellurium has the largest nonlinear optical coefficient $d_{111} = 1.6 \times 10^{-6}$ ESU of any known material {17}; thus it is presently of considerable interest as a frequency doubler {18}, and for possible parametric amplification {19} in the range of infrared wavelengths.

III 5.2 Natural Optical Activity

Due to the helical nature of the tellurium crystal structure, it is found that linearly polarized light, in the plane perpendicular to the optic axis, is rotated as the light beam travels along the c-axis. This effect, called natural optical activity {20}, is characterized by a quantity known as the "rotary power" which is defined as the amount of angular rotation per millimeter of travel length. The

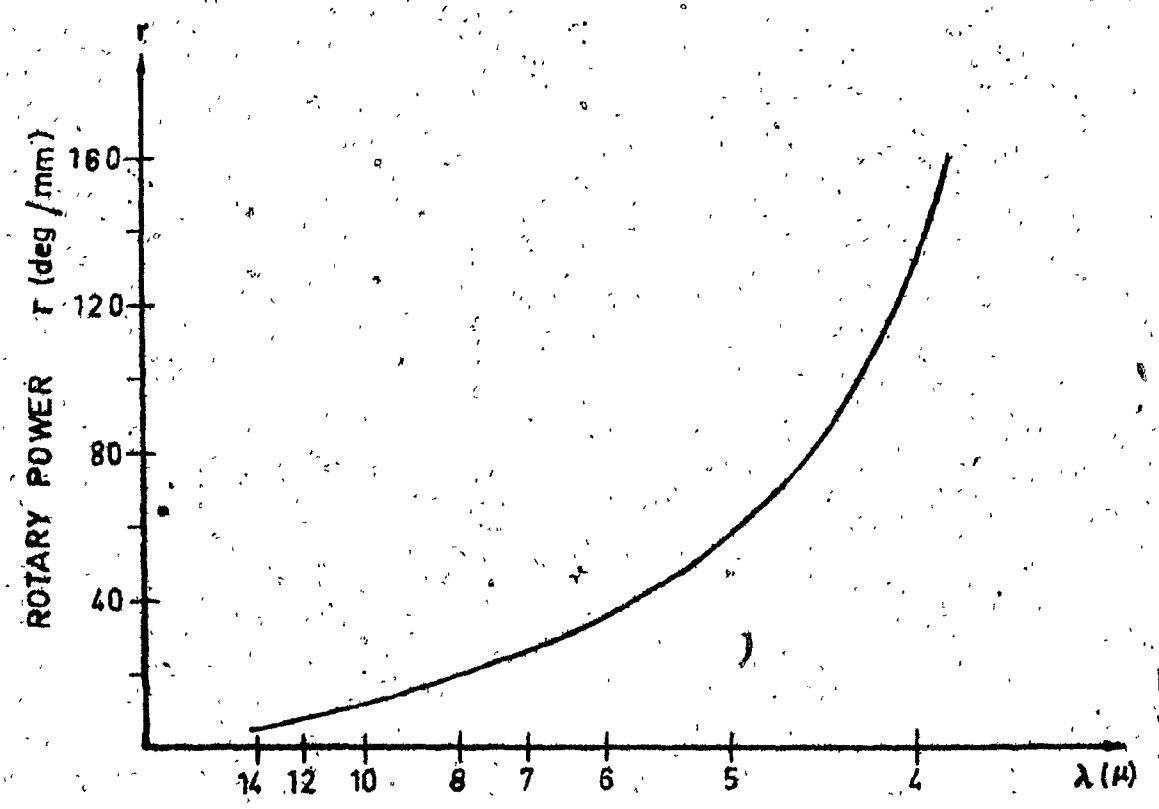

Figure 3. Rotary Power vs Radiation Wavelength λ in microns.
From S. Ades, M. Eng. Thesis, McGill University, 1975.

complete wavelength dependence of the rotary power in tellurium is shown in Figure 3, noting that at 10.6 μ, the electric field rotates at a rate of 11 deg/mm. This phenomenon is of particular importance when considering effects which depend on the exact polarization of the radiation field in the material.

III 5.3 Absorption

The infrared absorption spectrum of tellurium {21} is shown in Figure 4 and Figure 5 for polarizations parallel and perpendicular to the optical axis. It can be noted generally that for radiation parallel to the c-axis, there is a relatively strong absorption peak at 11μ, whereas for $E \perp c$, tellurium is essentially transparent from 5μ to wavelengths longer than 20μ. An additional observed dichroism is that the band gap absorption at wavelengths less than 4μ, is favoured for polarization perpendicular to the optical axis {22}. The mechanisms determining this absorption spectrum are discussed further in the next section in terms of electronic transitions in the energy bands.

III 6.0 Tellurium Band Structure

III 6.1 Introduction

As extrinsic tellurium is always found to be p-type, the information obtained from such experiments as the

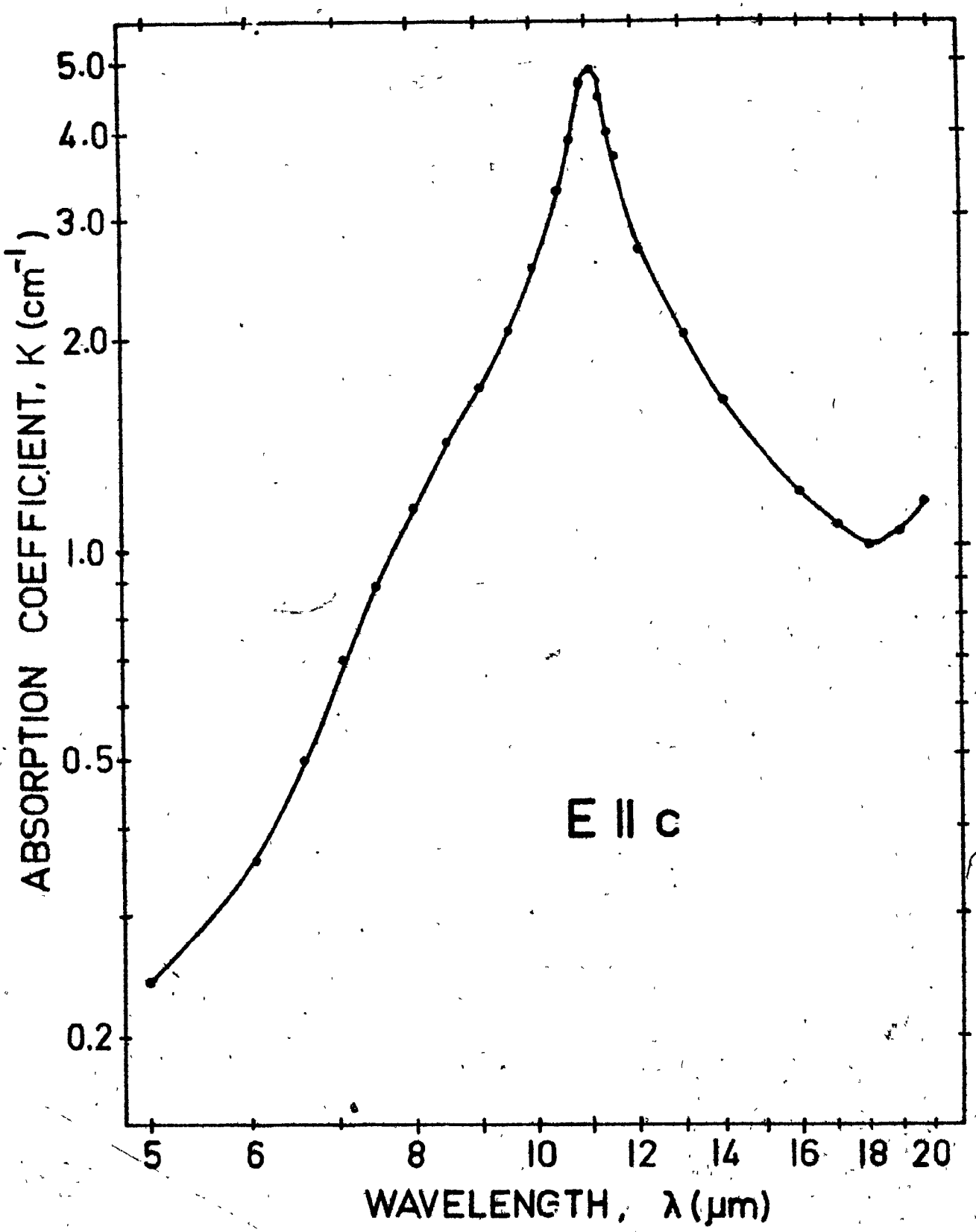

Figure 4. Absorption Coefficient vs Wavelength for E || c in Undoped Tellurium.

From S. Ades, M. Eng Thesis, McGill University, 1975.

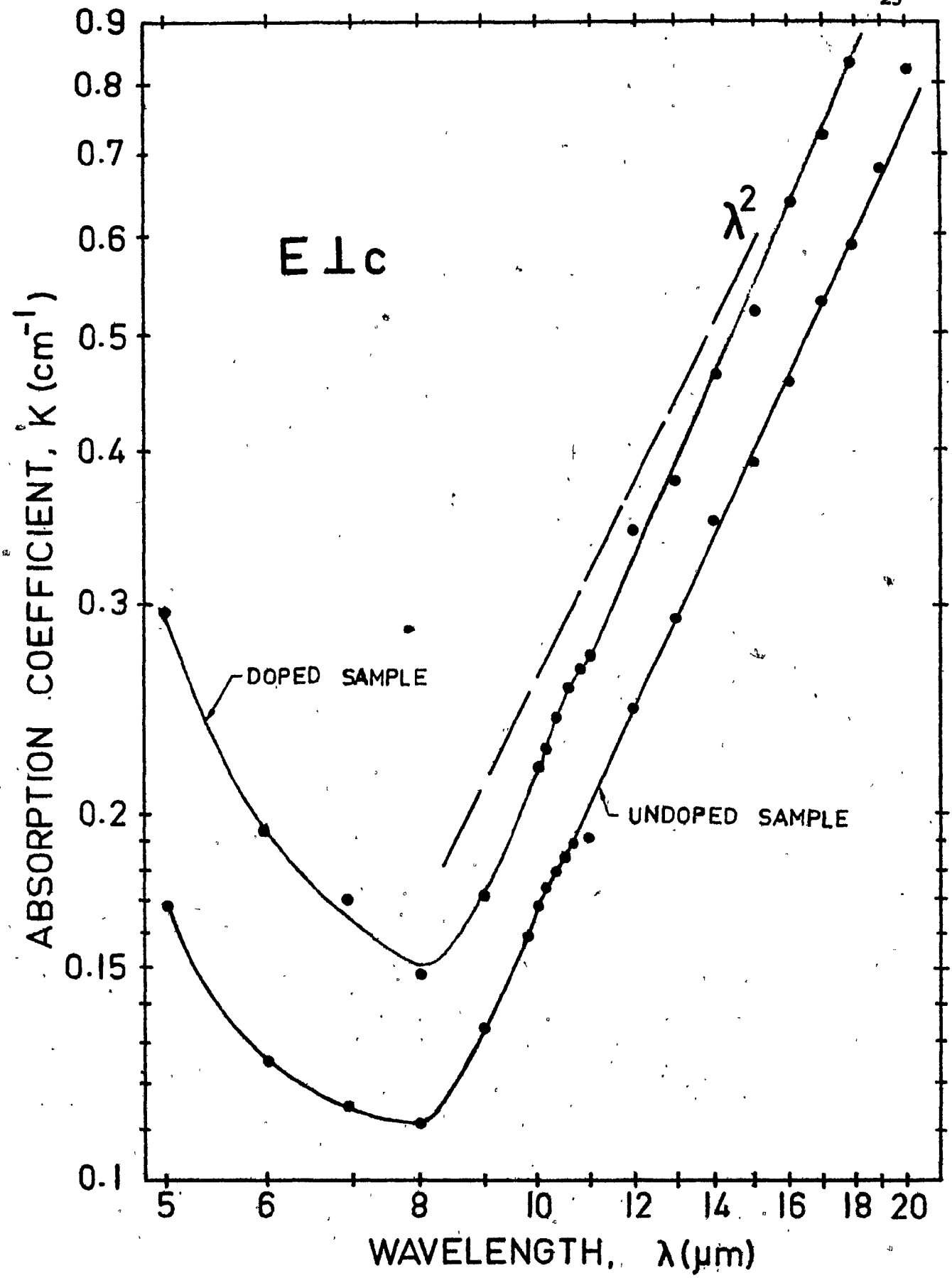

Figure 5. Absorption Coefficient vs Wavelength for E ⊥ c.
From S. Ades, M. Eng Thesis, McGill University, 1975.

infrared absorption spectrum, far infrared cyclotron resonances, magneto absorption, and the Shubinov - de Haas effect, mainly show the characteristic features and structure of the valence band; consequently, much remains unknown about the conduction band. In fact, until very recently, it was only known that the energy gap, obtained from fundamental absorption measurements, is about 0.34 eV, that this absorption shows a conspicuous dichroism {Section III 5.3}, and that the energy gap is direct and located in the neighbourhood of the point H of the Brillouin zone {23}, see Figure 6. The state of the art of the essential details of both band structures are presented in the following sections.

III 6.2 The Valence Band

III 6.2.1 Structure

The total valence band structure, shown in Figure 7, consists of a number of separate bands which are created by the splitting of degenerate states as a result of spin orbit coupling {24}. A particular feature of the uppermost valence band is its "camel-back" shape in the z or c direction with a central dip of the order of 0.002 eV.

Theoretically the generalized energy dispersion relations for the two uppermost bands, H_4 and H_5, are found to be {25}:

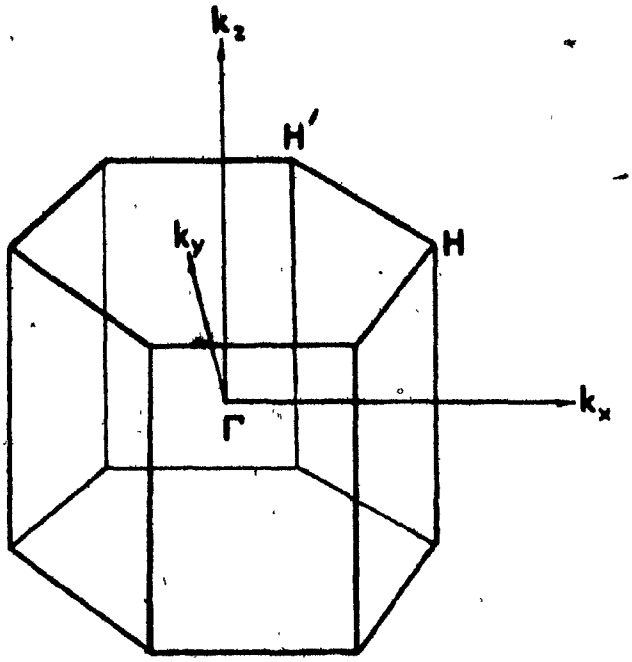

Figure 6. The First Brillouin Zone of Trigonal Tellurium.

Points H and H' are degenerate due to time reversal symmetry.

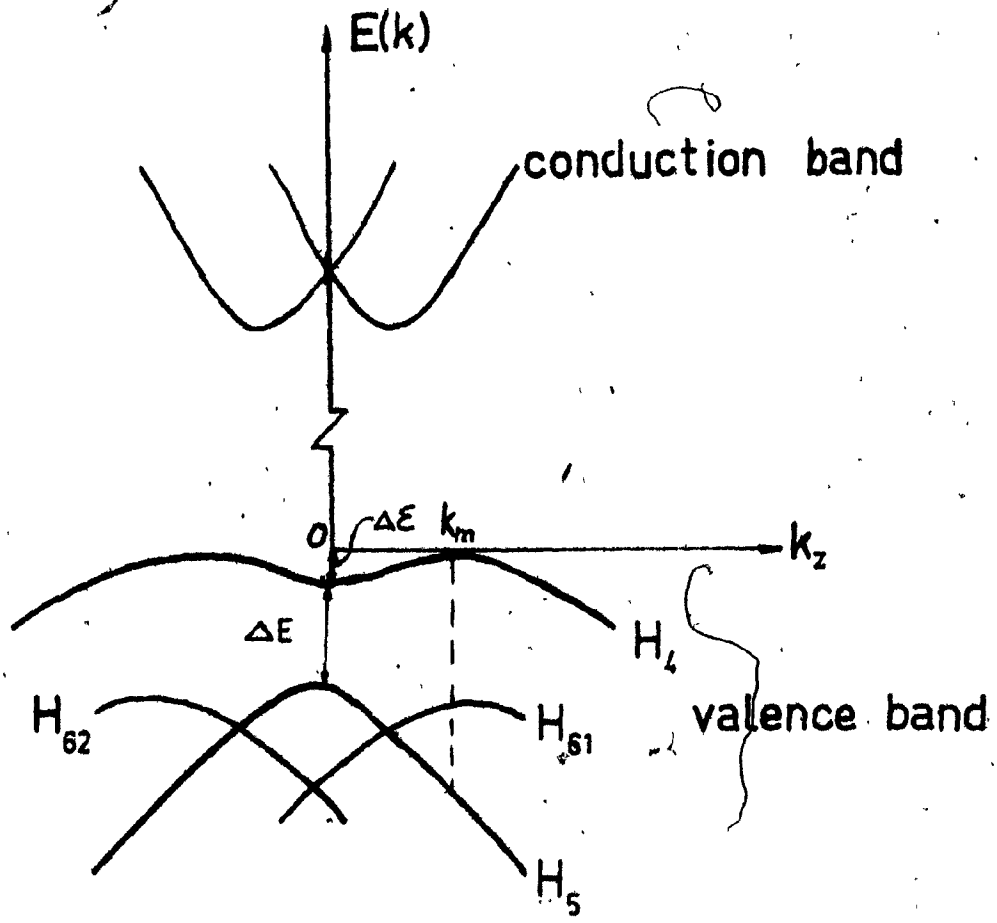

Figure 7. Conduction and Valence Bands in Tellurium.

$$E_{4,5}(\vec{k}) = Ak_\perp^2 + Dk_z^2 \pm \left[S^2 k_z^2 + (\Delta E/2)^2\right]^{1/2} - (\Delta\mathcal{E} + \Delta E/2)$$

$$+ Bk_\perp^4 + Qk_z^2 k_\perp^2 - C_1 k_x (k_x^2 - 3k_y^2) + C_2 k_z k_y (k_y^2 - 3k_x^2) \quad (4)$$

where $k_\perp^2 = k_x^2 + k_y^2$

The k-linear term, i.e. the third term in the above equation, produces the "camel-back" shape in the H_4 band. The experimentally found values for the various parameters in the energy dispersion equation are given in Table 2. This information on the energy band structure can be used to evaluate different physical parameters. Thus the effective mass of holes in the two uppermost bands are obtained from the following general formula,

$$m_{ii} = \left(\frac{1}{\hbar^2} \frac{\partial^2 E(\vec{k})}{\partial k_i^2}\right)^{-1} \quad (5)$$

For the valence band H_4 :

at $\vec{k} = 0$, $\begin{cases} m_\parallel = -.25\, m_0 \\ m_\perp = .13\, m_0 \end{cases}$; at $k_z = k_m$, $\begin{cases} m_\parallel = .17\, m_0 \\ m_\perp = .13\, m_0 \end{cases}$; $k_\perp = 0$

where $m_\parallel$ and $m_\perp$ are the effective masses parallel and perpendicular to the z or c direction respectively, and k_m is the position of the peak of the "camel back" on the k_z axis, see Figure 7.

For the valence band H_5 :

TABLE 2

Values of the parameters for the valence band {26}

Band parameter	Value
A	-3.26×10^{-15} eV cm^2
S	24.7×10^{-9} eV cm
$\Delta E/4$	.0315 eV at (20 K)
D	-3.67×10^{-15} eV cm^2
$\Delta\varepsilon$	0.0023 eV
B	$.06$ to $.07 \times 10^{-27}$ eV cm^4
Q	$.03$ to $.04 \times 10^{-27}$ eV cm^4
C_1	?
C_2	$.18 \times 10^{-29}$ eV cm^4
k_m	2×10^6 cm^{-1}

at $k = 0$, $\begin{cases} m_{\parallel} = .04\ m_0 \\ m_{\perp} = .13\ m_0 \end{cases}$

III 6.2.2 Electronic transitions

The detailed structure of the infrared absorption spectrum is explained by various transitions between and within the valence bands.

Direct transitions of holes between the H_4 and H_5 bands are allowed only for $E \parallel c$; the strong absorption peak at 11μ is due to hole transitions at $k = 0$, while the less pronounced bulge in the absorption curve in the vicinity of 7μ is a result of direct transitions at $k = k_m$.

Excluding the above mentioned peaks at 11 and 7μ for $E \parallel c$, the remainder of the absorption for $E \parallel c$ and essentially the entire absorption spectrum for $E \perp c$ between the fundamental absorption edge, at 4μ, and about 25μ is normally called the "background absorption" and is attributed to intraband transitions. These intraband transitions, shown in Figure 8, are indirect phonon assisted transitions of holes within the H_4 - valence band as well as of electrons within the conduction band, whose relative contribution to the total absorption for $E \perp c$ is found to be comparable in magnitude. Direct electronic transitions between the H_6 and H_4 valence bands, allowed only for $E \perp c$, contribute the small additional observed absorption near 10μ for this radiation polarization {27}.

III 6.2.3 The temperature variation of the energy separation of the valence bands.

It is found that the energy separation ΔE of the two valence bands H_4 and H_5 is temperature dependent having a coefficient {24},

$$\frac{\partial \Delta E}{\partial T} \equiv \alpha = 4 \times 10^{-5} \text{ eV/deg}$$

At room temperature $\Delta E = .114$ eV, on the other hand, at a temperature of 225 K, $\Delta E = .117$, the energy equivalent to the CO_2 laser 10.6 μ radiation. According to radiation absorption data {24}, below the latter temperature, there is still considerable absorption of the 10.6 μ radiation even though the energy separation of the two valence bands becomes larger than the CO_2 laser photon energy. Electronic transitions between the bands is still possible because the energy levels are unsharp, due to the Heisenberg uncertainty principle, by at least an amount equal to .004 eV assuming an energy relaxation time of 10^{-12}s. The electronic transitions probably occur near or at $k = 0$ for radiation wavelengths corresponding to photon energies smaller than the energy separation of the valence bands.

III 6.3 The Conduction Band

The conduction band structure has recently been discussed by Shinno et al {28} and is shown in Figure 7. The

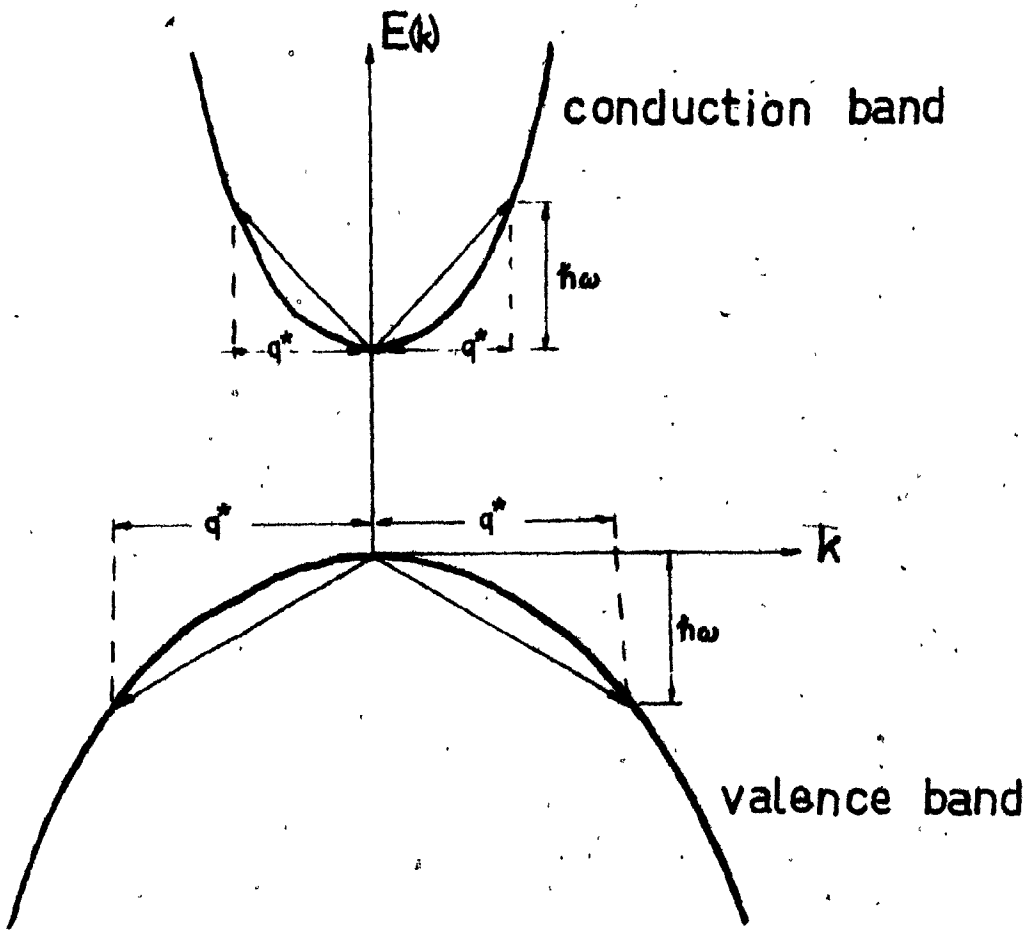

Figure 8. Intraband Transitions.

Electrons and holes must interact simultaneously with photons of energy $\hbar\omega$ and phonons with momentum $\hbar q^*$ in order to satisfy conservation of energy and momentum laws.

above authors have derived theoretically the following E - k relation for the conduction band up to terms quadratic in k.

$$E_c(k) = A_c k_t^2 + B_c k_z^2 + \Delta_c \pm \sqrt{M^2 k_t^2 + N^2 k_z^2} \qquad (6)$$

It is seen that again a k-linear term exists which in this case produces two overlapping conduction bands with their minima offset from k = 0. The experimentally found parameter values of Equation (6) are presented in Table 3 {28}.

From these given energy band parameters, the effective masses of the conduction electrons in directions parallel and perpendicular to the c-axis at the band minimums are obtained as:

$$m_{\parallel} = 0.070\ m_0$$

and

$$m_{\perp} = 0.104\ m_0 .$$

III 7.0 Conclusions

This chapter has presented the essential information on the structure and properties of tellurium from the point of view of their relevance to the present work. It is expected that the analysis and interpretation of the laser induced electric signals in the course of the present investigation will allow the confirmation of some known parameter values as well as the determination of some new properties.

TABLE 3

Value of parameters for the conduction band [28]

Band parameters	Value
A_c	3.65×10^{-15} eV cm^2
B_c	5.47×10^{-15} eV cm^2
Δ_c	.337 eV
$\|N\|$	7.12×10^{-9} eV cm
$\|M\|$	2.25×10^{-9} eV cm

CHAPTER IV

EXPERIMENTAL PROCEDURE FOR THE OBSERVATION OF SIGNALS INDUCED IN TELLURIUM BY A TEA CO_2 LASER

IV 1.0 The Experimental Set-Up

IV 1.1 Introduction

The object of the experimental set-up is to provide the possibility of measuring the electric signals induced in tellurium samples subjected to the radiation from a TEA CO_2 laser under varying and controlled configurations of the sample orientation relative to the laser beam propagation and polarization directions, from room down to approximately liquid nitrogen temperatures. The main components of this experimental set-up consist of a CO_2 laser, a pyroelectric detector, different tellurium crystals, and electronic signal measuring apparatus. Provisions are made to cool the tellurium crystals down to near liquid nitrogen temperatures.

IV 1.2 The Source of Radiation

A Lumonics series 101 TEA CO_2 laser is used as a source of the 10.6 μ pulsed high power radiation. The TEA laser operates by the method of transverse excitation of a lasing gas, in this case a 1 : 2 : 10 mixture of N_2, CO_2,

and He gases. The transverse excitation allows a large amount of energy to be dumped into a gas at relatively high pressure (atmospheric) while keeping the excitation voltages within practical limits of about 40 kV.

The laser output power density is measured to be approximately 400 kW/cm^2 with a beam area of about 2.5 cm^2, thus giving a total peak power in the vicinity of 1 MW. The radiation pulse, Figure 9, has a half power width of 180 ns with a rise time of 70 ns. The tail of the pulse, the magnitude of which can be controlled by varying the proportion of the N_2 content in the laser gas mixture, shows a slow component with microsecond decay times. In addition, due to random partial self-mode locking of the laser, a fine structure is added to the main energy pulse exhibiting typical rise times of 10 ns with a duration of about 30 ns; this structure is especially observed with small area detectors. The laser is capable of a trouble free operation with repetition rates up to 5 pulses per second.

IV 1.3 The Pyroelectric Detector

The laser output pulse shape and power is measured with a Molectron model P3 pyroelectric detector, having a known responsivity of 0.15mV/W, with a rise time of 5 ns, and an element area of 1 mm square. This detector is mainly used to monitor the incident laser beam power so that the

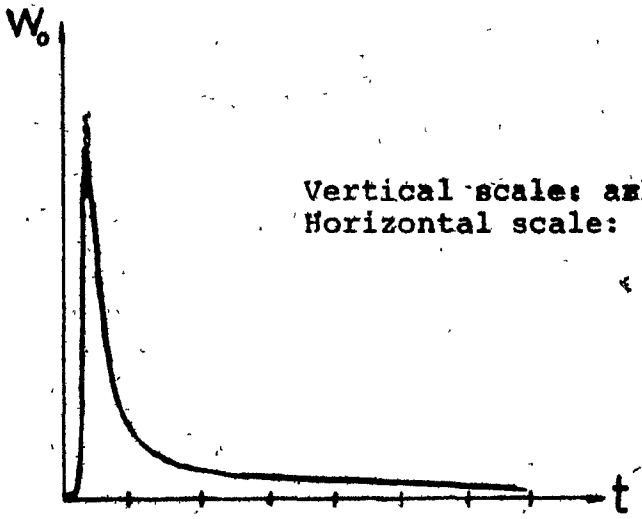

Figure 9. Laser Radiation Pulse Power Output measured with a Te sample.

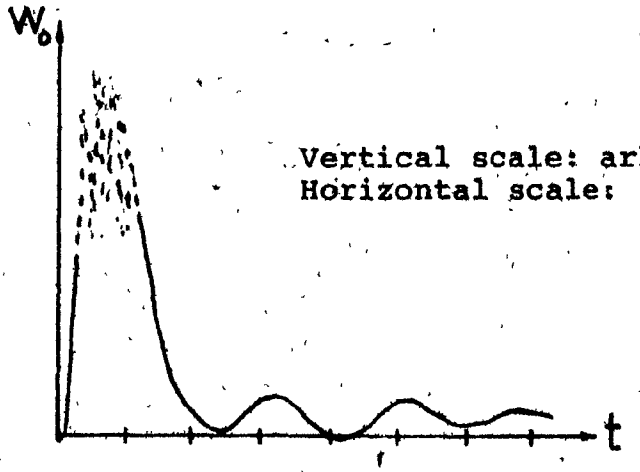

Figure 10. Response of the Pyroelectric Detector.

Note: Figures are tracings from actual oscillogram photographs.

responsivity corresponding to the various tellurium sample configurations can be determined. A typical output signal from the pyroelectric detector is shown in Figure 10.

IV 1.4 Signal Measuring Apparatus

The induced electric signals in the tellurium samples are monitored on a 100 MHz Tektronix 465 oscilloscope. A Hewlett-Packard 462 preamplifier with a 40 db gain and a 4 ns rise time is coupled via a 50 Ω load to the oscilloscope enabling the measurement of signals down to 40 μV.

IV 1.5 The Tellurium Crystals

Good quality tellurium single crystals were grown in the Department of Electrical Engineering by the Czochralski method from high purity zone refined polycrystalline tellurium material. Large ingots with up to 2 cm cross-sectional diameters and up to 6 cm in length were grown along the c-axis; the crystals exhibited good trigonal symmetry. While most of the crystals were grown to exhibit intrinsic properties down to the lowest possible temperature by attempting to minimize their acceptor impurity concentration, some antimony doped p-type crystals were also grown and used in this work. A typical tellurium crystal ingot is shown in Figure 11a. Samples with the desired crystallographic

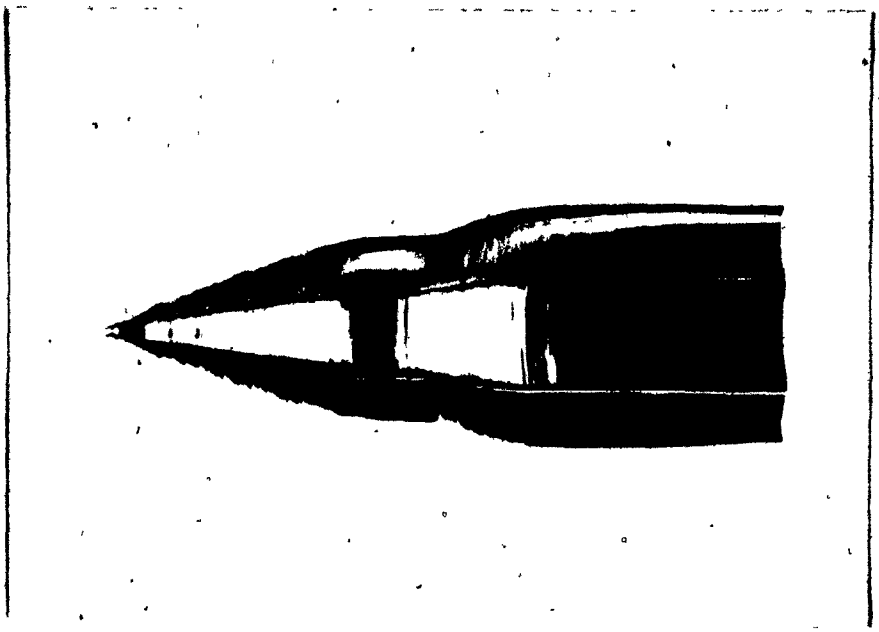

Figure 11a. A Tellurium Ingot

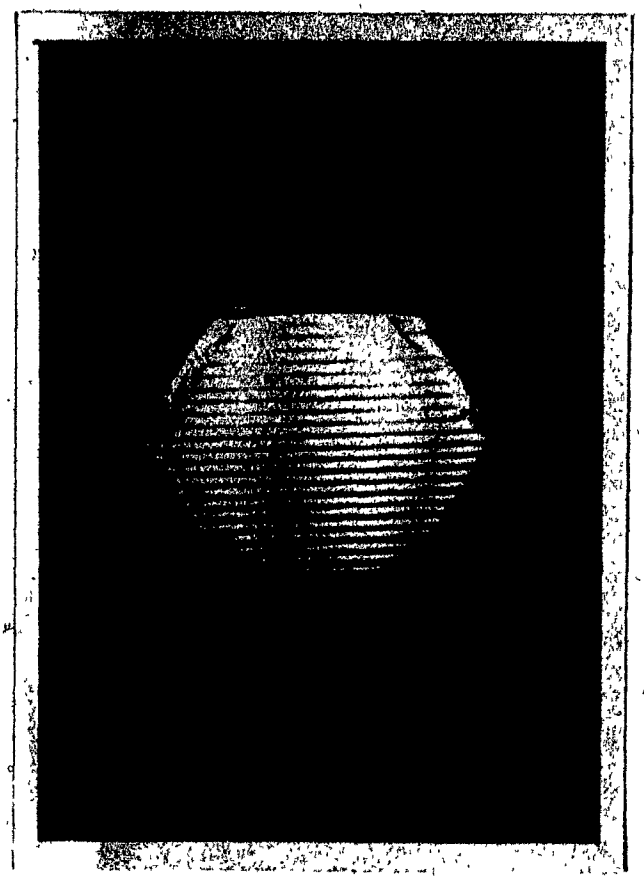

Figure 11b. A Typical Tellurium Cross-Section after Acid Saw Cutting.

orientations and geometries were cut from these large single crystals by making use of specially constructed acid saws.

IV 2.0 Sample Preparation

IV 2.1 Introduction

As previously stated in Section III 2.0, as a result of the weak binding forces between the atomic chains, tellurium single crystals are readily damaged mechanically; slip fracture, deformation, and formation of dislocations are commonly observed in tellurium single crystals. Thus it was attempted to minimize the necessity of excessive mechanical handling by eliminating entirely the use of abrasive cutting and polishing processes.

IV 2.2 Sample Cutting

All cutting of the tellurium crystals was accomplished by using a specially constructed acid saw which essentially consisted of a polyester thread which continuously extracts fresh acid from a reservoir and brings it into contact with the crystal surface so that only a chemical action is used to remove the semiconductor material under the thread. The acid solution employed for cutting perpendicular to the c-axis consisted of a mixture of chromic trioxide, hydrochloric acid, and distilled water in 1:1:2 proportions

by weight. It was found that although this solution could also be used for cuts parallel to the c-axis, an acid solution with the HCl acid replaced by nitric acid in a 1:2:4 proportions produced smoother surfaces in those directions. A typical surface after acid cutting is shown in Figure 11b.

IV 2.3 Sample Polishing

The surface after cutting shows small undulations which are removed by chemically polishing the samples in the chromic nitric acid mixture mentioned above. The resulting surface has a mirror like finish, well suited for the measurement of CO_2 laser generated signals in tellurium.

IV 2.4 Sample Dimensions

For longitudinal measurements, i.e., for voltages measured in the direction of light propagation, the crystals were cut into rectangular rods having typical cross-section dimensions of 5 mm square with lengths varying from 1 to 3 cm, see Figure 12a.

For transverse signals, i.e. for voltages measured in a direction perpendicular to the light propagation, the samples are 1-2 mm thick and have either the natural hexagonal cross-section of the ingot for devices which are cut in a plane perpendicular to the c-axis, or, they are typically

of a rectangular 1 x 1.5 cm cross-section containing the c-axis; see Figures 12c and 12d.

IV 2.5 Electrical Contacts

Ohmic contacts were made to the tellurium sample surfaces by alloying small strips of a specially prepared solder containing antimony, lead, and indium in 1.7 Sn: 1.3 Pb:In proportions onto the sample surfaces. The melting point of this solder is approximately 150°C. Fine copper wire is then soldered to the alloyed strips to complete the contact fabrication process.

IV 3.0 Preliminary Observations

IV 3.1 Introduction

As stated in Chapter 1, the original aim of this work was the search and analysis of the photon drag effect in tellurium. Initial measurements of the generated electric signals were made in the longitudinal directions by illuminating the rectangular rods of tellurium single crystals {see Section IV 2.4}, from either end by radiation from the TEA CO_2 laser; the repetition rates were normally kept below one pulse per second in order to insure good pulse to pulse reproducibility and laser stability over extended periods of time. The resulting electric voltages were monitored on the oscilloscope with particular attention

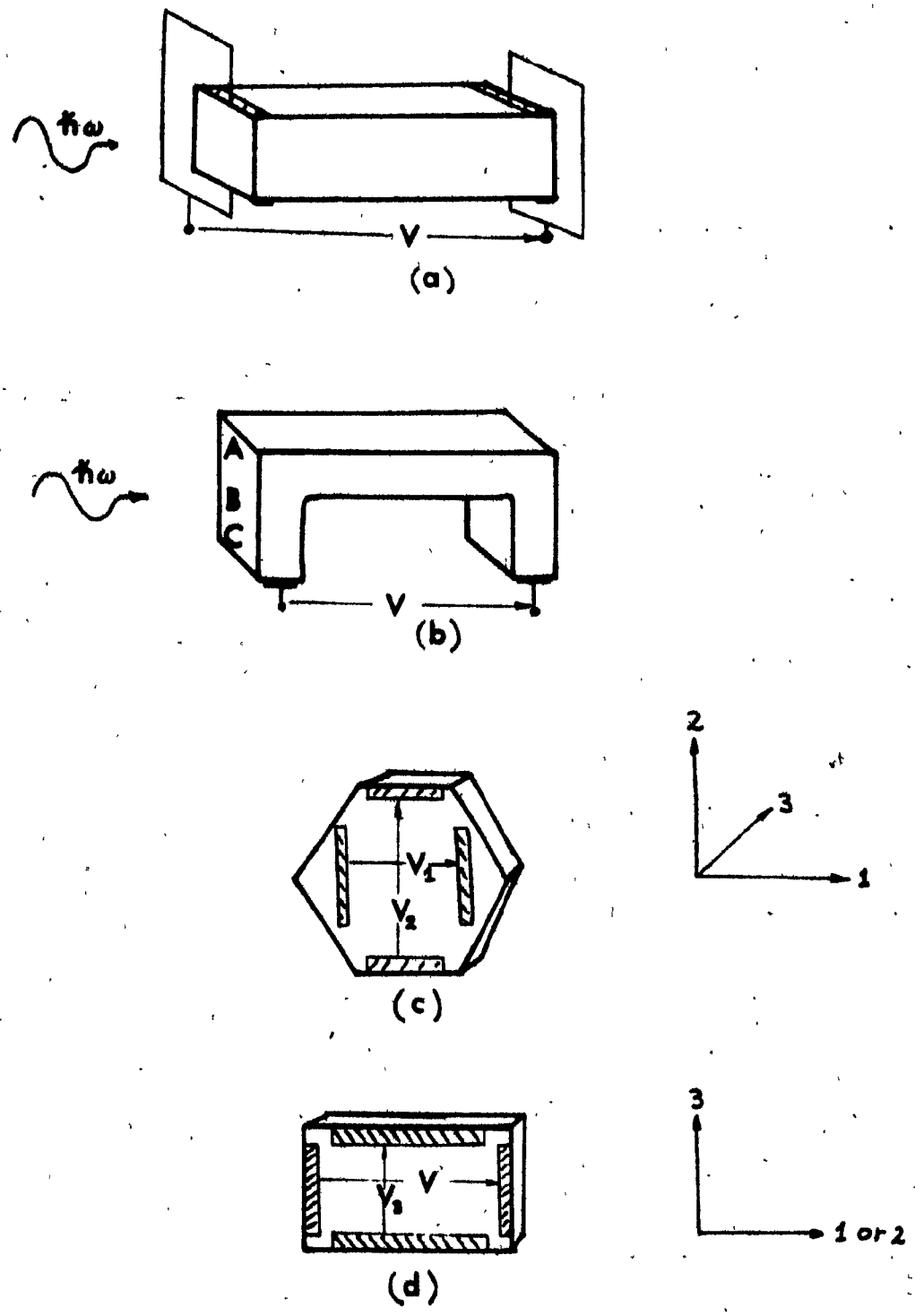

Figure 12. Sample Configurations.

(a), (b) used for longitudinal measurements;

(c), (d) used for transverse measurements.

being focused on the magnitude, polarity, and shape of the pulses as a function of propagation and polarization directions of the incident radiation. Measurements were performed first at room temperature, and later at temperatures down to approximately 115 K with the use of a liquid nitrogen dewar.

IV 3.2 Initial Results

The preliminary measurements were performed at room temperature on the rectangular samples whose long dimension was first oriented in an arbitrary direction perpendicular to the c-axis. The following is a description of the observed behaviour of the generated longitudinal signals in these samples according to the polarization relative to the c-axis of the radiation electric field E and with respect to the reversal in the direction of light propagation. It is to be noted that all situations where the radiation electric field E is parallel to the crystallographic c direction will be referred to $E \parallel c$, while $E \perp c$ corresponds to the case of the electric field E being perpendicular to the c-axis.

(a) With $E \parallel c$, a relatively large fast signal was observed, with a magnitude equal to 10 mV/MW cm^{-2}, which was considered to be a true reproduction of the laser pulse. The polarity of this voltage corresponded to a generated

short circuit current in the direction of light propagation. A reversal in the light propagation direction, obtained by illuminating the opposite end of the sample and keeping the light polarization unchanged, only resulted in a reversal in the polarity of the monitored signal.

(b) With $E \perp c$, a fast emf of generally the same order of magnitude as for $E \parallel c$ was observed, but it was interesting that in this case, no polarity inversion occurred when the propagation direction was reversed.

(c) Thus, as the polarization was rotated from $E \parallel c$ to $E \perp c$, one end of the sample exhibited signals of continually varying magnitudes of the same polarity, whereas with the illumination from the opposite end, the signal decreased in magnitude, passed through zero, and then increased once again, with an inverse polarity.

(d) Furthermore, when attention was begun to be focused on the particular crystallographic direction of the sample's longitudinal orientation conjunctly with the light propagation direction, it was discovered that the magnitude of the $E \parallel c$ signals remained constant, while the magnitude of the $E \perp c$ voltages were largest for measurements in the 1, i.e. $[1\bar{2}10]$ and equivalent directions, and were essentially zero in the 2, i.e. $[10\bar{1}0]$ and equivalent directions.

(e) Some samples were cut into the U-shape shown in Figure 12b; when the incident beam diameter was reduced and localized by a pin hole less than 2 mm in diameter, it was found that as the illuminated area was swept from points A to C, the fast signals decreased reaching a minimum at point B, then as the area adjacent to the contact C was illuminated, a much slower, (microsecond decay time), signal became dominant. It was also discovered that this slow signal was largest for polarizations perpendicular to the c-axis; the magnitude of this signal increased nonlinearly with the increase of the incident radiation intensity.

These series of results were consistently observed in all samples prepared for these preliminary measurements.

IV 4.0 Interpretation of Preliminary Results

The following important conclusions were drawn from the previously stated observations and experiments.

(1) Observation "e", shows that the origin of the fast signals cannot be attributed to any diffusion type effects caused by thermal or carrier gradients, because the fast signals decrease as the illuminated area approaches the contacts which is contrary to the expected behaviour of diffusion induced voltages. Also, since the fast emfs are obtained only when the radiation illuminates the elongated part of the samples it is concluded that the measured voltage is a result

of an emf induced along the radiation propagation path.

The slow signals, which become dominant with the illumination of the contact area, are on the other hand believed to correspond to a Dember diffusion type voltage caused by the presence of nonequilibrium electron-hole pairs generated by the relatively large three-photon absorption process in tellurium {29} which is preferential with $E \perp c$; the observed decay times are generally consistent with those found in photoconductivity experiments {30}.

(2) Having ruled out diffusion effects as the source of the fast signals, and the fact that the fast signal with $E \parallel c$ reverses its polarity with a reversal in the light propagation direction, (see observation "a"), clearly illustrates the basic feature of the photon drag effect corresponding to the linear dependence of the latter on the direction of the photon momentum. Furthermore, the magnitude of the induced emf agrees very favourably with the generally accepted theoretical expression for photon drag which is derived later in Chapter VII.

(3) Observations "b" and "c" led to the conclusion that, as the signal with $E \perp c$ remained unchanged with the reversal in the propagation direction, implying independence from the photon momentum, an effect other than photon drag is involved in this case which, according to observation "d", exhibits crystallographic orientation dependent characteristics.

IV 5.0 Conclusions

The previous observations have led to the necessity of establishing a phenomenological basis for the interpretation of the various obtained results. For this purpose the development of the tensorial representation of all possible types of generated signals which can be induced in a semiconductor by the electric field of the laser beam is given in the next chapter as the first step toward the quantitative characterization of the different observed fast signals.

CHAPTER V

PHENOMENOLOGICAL CHARACTERIZATION OF RADIATION INDUCED SIGNALS

V 1.0 Introduction

We propose that the current density vector generated in a semiconductor material by the laser radiation can in general be considered to be a function of the electric field and the momentum vector of the radiation beam; therefore, it can be written phenomenologically in terms of the following Taylor series expansion:

$$J_i = \sigma_{im} E_m + \beta_{ijm} \hat{q}_j E_m + \chi_{imn} E_m E_n + T_{ijmn} \hat{q}_j E_m E_n + \ldots \quad (7)$$

where

J_i is a component of the current density vector.

E_m is a component of the radiation electric field vector.

$\hat{q}_j$ is a component of the unit photon momentum vector.

σ_{im} is a second rank tensor component.

β_{ijm}, χ_{imn} are third rank tensor components.

T_{ijmn} is a fourth rank tensor component.

The first and fourth terms in the above expression for J_i correspond to the well established mechanisms of linear

conductivity and the photon drag effect {31}, respectively. The third term represents a quadratic response to the radiation electric field and thus leads to optical rectification; this latter non-linearity may be either due to free carriers, in which case it is referred to as non-linear conductivity, or it is due to bound charges in which case it corresponds to non-linear polarization. No known physical mechanism is associated with the second term and is only included for the sake of completeness.

It must be noted that, the first two terms of this equation are linearly related to the radiation electric field, and therefore, correspond to signals at the optical frequency of the laser radiation which are practically unobservable; the square law nature of the third and fourth terms, on the other hand, lead to the rectification of the excitation, resulting in measurable signals proportional to the envelope of the pulsed output of the laser. In this chapter, the exact tensorial characteristics of these third and fourth rank tensors are investigated in the specific case of the point group 32 symmetry associated with the tellurium crystal.

V. 2.0 The Third Rank Tensor Components

The trigonal symmetry of tellurium is described by the generation operations consisting of a 3-fold rotation

around the c-axis, also known as the z or 3-axis, Figure 1, and a 2-fold rotation about the x or 1-axis; the resulting invariance of all tensors subjected to such rotations, leads to the existence of only two finite and independent third rank tensor terms associated with the parameter χ in Equation (7) consisting of the tensor components {32},

$$\chi_{111} = -\chi_{122} = -\chi_{212} \tag{8}$$

and

$$\chi_{123} = -\chi_{213} \tag{9}$$

In the above components, the first subscript represents the measurement direction, and the remaining two subscripts correspond to the electric field components which therefore are naturally interchangeable. Thus in general

$$\chi_{imn} = \chi_{inm} \tag{10}$$

It is known that the electric field E is always perpendicular to the propagation direction; it naturally follows that if the propagation directions are considered only along the major axes, the χ_{122} component can in principle be experimentally determined by using both longitudinal and transverse measurements with respect to the propagation direction; on the other hand, χ_{123} and χ_{213} can only be determined by employing a longitudinal measurement with respect to the laser beam propagation direction, and χ_{111} and χ_{212}, in

turn, can only be obtained by measurements transverse to the direction of propagation.

V 3.0 Fourth Rank Tensor Components

The symmetry properties of tellurium lead to twenty-five finite elements for the fourth rank tensor T_{ijmn} {see Equation (7)} of which only ten are independent as shown in Table 4a {32}. Since the radiation electric field E is perpendicular to the light propagation direction, it can be easily seen that when the laser propagation direction is confined to those of the major axes, the generated and measured signals will never involve the tensor components with $j = m, n$. On the other hand, when an off major axis direction is chosen to propagate the laser beam, the generated and measured signals always involve several tensor components rendering the isolation of the contribution from any one component practically impossible.

The twenty-five tensor components are thus classified into two distinct groups corresponding to whether or not they appear in measurements confined to the major crystalline axes. Those non-zero components, henceforth called "major axes" components, which are measurable along the major axes can be further divided into subgroups called longitudinal and transverse components according to whether they are obtainable from longitudinal or transverse measurements respectively {see Section IV 2.4}.

Table 4a: Fourth Rank Tensor Matrix [32]

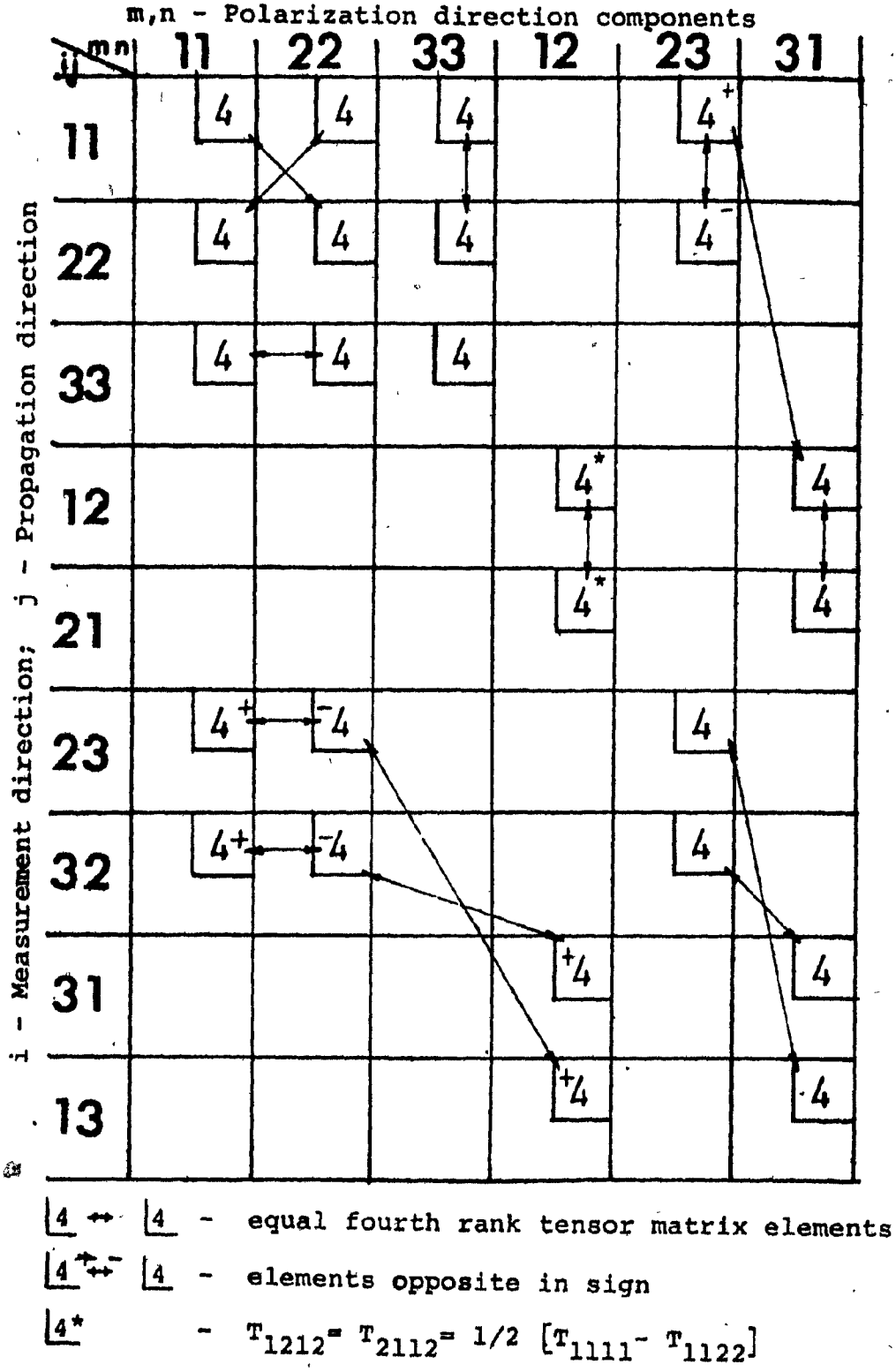

Table 4b: Fourth and Third Rank Tensor Matrix

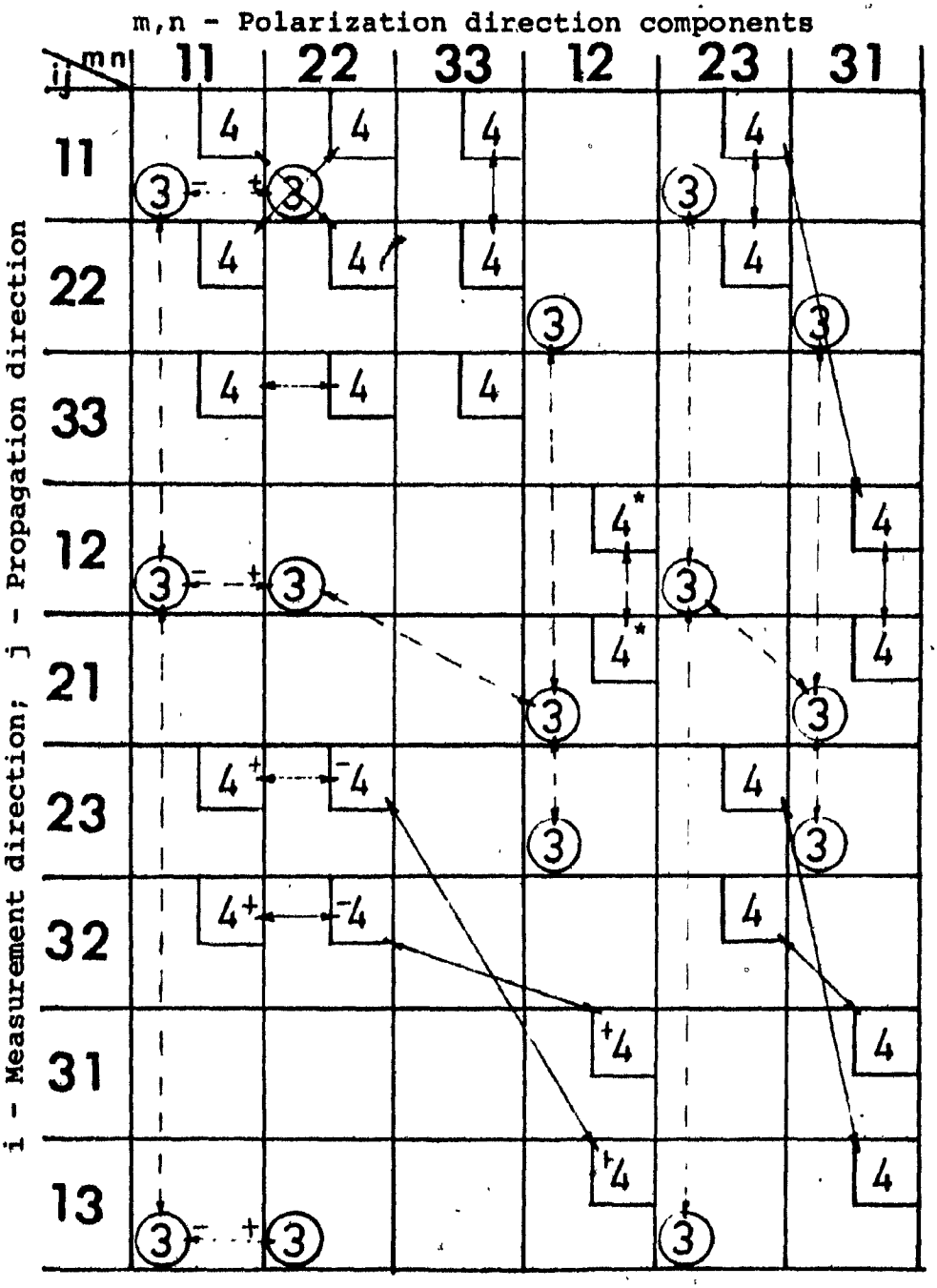

(3) - third rank tensor with the "j" direction implicitly assumed.

(a) The "major axes" tensor components

The twelve "major axes" tensor components are characterized by indices $j \neq m,n$; only six of these components are independent (see Table 4a) corresponding to the following sets of equal terms.

Set 1 : $T_{1133} = T_{2233}$

Set 2 : $T_{1122} = T_{2211}$

Set 3 : $T_{3311} = T_{3322}$

Set 4 : $T_{2311} = -T_{2322} = T_{1312}$

Set 5 : T_{3211}

Set 6 : $T_{1123} = T_{1231}$

(b) The longitudinal components

Since for longitudinal measurements, $i = j$, the longitudinal components are those of Sets 1, 2, 3 and element T_{1123} of Set 6. These components are determined by using longitudinal type samples {see Section IV 2.4}.

(c) The transverse components

The remaining elements with $i \neq j$ found in Sets 4, 5, and 6 are the transverse components; they are obtained with transverse type of measurements {see Section IV 2.4}.

(d) The components of Set 6

It should be noted that when attempting to measure the tensor component T_{1123}, the generated signal would

always include as well the contributions of the elements T_{1122} and T_{1133}; the component T_{1123} can, therefore, not be determined separately. On the other hand, T_{1231} appears to be measurable independently from the other fourth rank tensor components.

In summary, it is apparent that from the original ten independent components of the photon drag tensor, there exists at least one combination of the measurement, propagation and polarization directions which allows the separate determination of six independent components, represented by the six sets defined in the above paragraph (a). On the other hand, T_{1123} and the other finite tensor components can only be evaluated by taking differences of at least two separate measurements.

It is pointed out that the photon drag effect, as represented by the fourth rank tensor in Equation (7), is explicitly a function of the photon momentum, and thus has the unique feature that the corresponding induced signal must reverse its polarity with a reversal in the light propagation direction.

V 4.0 Separation of Signals due to Third and Fourth Rank Tensors

The measured signal which is induced in tellurium by the laser electric field is in general composed of contributions

from a combination of third and fourth rank tensor components as shown in Equation (7). Nevertheless, by carefully selecting an appropriate set of measurement, propagation, and polarization directions, the resultant signals will be solely due to only one third or fourth rank tensor component.

In order to facilitate the process of choosing the appropriate measurement condition which will lead to the determination of a particular tensor component separately, the third rank tensor components are incorporated into the fourth rank tensor component representation matrix of Table 4a using the following procedure:

It is considered that, although the third rank tensor components are defined independently from the laser beam propagation direction {see Section V 2.0}, nevertheless, a propagation direction necessarily exists in an actual measurement. Thus, one may attach to each of the third rank tensor components, a fourth subscript j which defines all three possible propagation directions. In this manner, all the finite third rank tensor components which are now appended with four indices are introduced into Table 4a. For example, in the case of the third rank tensor component χ_{122}, three equivalent fourth rank tensor components are generated when j runs from 1 to 3, namely χ_{1122}, χ_{1222}, χ_{1322}, it is noted that only χ_{1122} and χ_{1322} are "major axes" components which appear in measurements where the

laser beam propagation direction is in the 1 or 3 directions respectively. Table 4b, which now contains both the third and fourth rank tensor components, can conveniently be used in this form to choose the necessary measurement conditions in order to obtain the various tensor components separately.

It is thus found by inspection of Table 4b that the following tensor components can be measured separately:

1) Fourth rank tensor components

Set 1 : T_{1133}, T_{2233}

Set 2 : T_{2211}

Set 3 : T_{3311}, T_{3322}

Set 4 : T_{2311}, $-T_{2322}$

Set 5 : T_{3211}

2) Third rank tensor components

χ_{111} as χ_{1211} or χ_{1311} in the equivalent fourth rank tensor representation

χ_{122} as χ_{1322} in the equivalent fourth rank tensor representation

χ_{212} as χ_{2312} in the equivalent fourth rank tensor representation.

In summary it is seen that at least one component from each of the Sets 1 to 5 (see Section V 3.0a) of the

fourth rank tensor components are separately measurable; however, no component of Set 6 is separately measurable, as the induced signal J_1 {see Equation (11)} associated with the measuring conditions corresponding to T_{1231} always has the additional contribution from the third rank tensor component χ_{111},

$$J_1 = \chi_{111} E_1 E_1 + 2 T_{1231} \hat{q}_2 E_3 E_1 \qquad (11)$$

Similarly it is discovered that only one of the two independent components of the third rank tensor, consisting of the equivalent matrix elements χ_{111}, χ_{122} and χ_{212} can be obtained separately; indeed in a typical measurement {see Equations (12) and (13)} the matrix elements χ_{123} or χ_{231}, associated with the other independent third rank tensor component, appear always in combination with at least one fourth or third rank tensor component, e.g.,

$$J_2 = 2 \chi_{231} E_3 E_1 + T_{2211} \hat{q}_2 E_1 E_1 + T_{2233} \hat{q}_2 E_3 E_3 \qquad (12)$$

and

$$J_1 = 2 \chi_{123} E_2 E_3 + \chi_{122} E_2 E_2 + T_{1122} \hat{q}_1 E_2 E_2 + T_{1133} \hat{q}_1 E_3 E_3 \qquad (13)$$

V 5.0 Conclusion

A phenomenological tensorial analysis is given in this chapter which defines the measurable radiation induced signals as combinations of two effects which are characterized

by third and fourth rank tensor components; the latter will naturally comply with the symmetry properties of tellurium. The conditions of measurement where the different tensor components can be obtained are discussed and specifically, the particular combinations of the measurement, propagation, and polarization directions where third and fourth rank tensor components can be measured separately, are deduced.

CHAPTER VI

EXPERIMENTAL RESULTS

VI 1.0 Introduction

The object of the experimental programme was to measure the expected finite components of both the third and fourth rank tensorial coefficients described in the previous chapter. The results of the analysis of Chapter V were used to choose the optimum measuring conditions for the determination of the various tensor components separately. The experiments consisted essentially in the simultaneous measurement of the fast induced open circuit voltages and the sample resistance in samples of geometries given in Section IV 2.4, over the temperature range 115 K to 300 K; the temperature dependence of these measured parameters is expected to provide an important basis for the determination of the physical mechanisms underlying the observed signals. Experiments were performed on samples cut from undoped tellurium crystals which exhibit intrinsic properties at room temperature, becoming extrinsic and p-type only below 200 K; extrinsic samples from antimony doped ingots with an estimated room temperature hole density of approximately $1 - 2 \times 10^{16}$ cm^{-3} were also used in order to investigate the dependence of the observed signals on the carrier concentration.

The accuracy in determining the values of the tensor components, taking into account the intrinsic errors in the measuring apparatus and in the laser power output, is estimated to be better than 10%.

VI 2.0 General Remarks on the Sample Parameters Affecting the Measured Signals

VI 2.1 Measurement of Open Circuit Voltages

As shown by Equation (7), the radiation electric field E generates locally an electric current J in a semiconductor; only the components of J which are quadratic in E are expected to result in observable signals (see Section V 1.0). These latter components of the current, under open conditions, clearly manifest themselves as an induced local electric field $\mathcal{E}_i$ which is related to J_i through the sample resistivity ρ_{ii}, i.e.

$$-\mathcal{E}_i = \rho_{ii} J_i = \chi^* W e_m e_n + T^*_{ijmn} \hat{q}_j W e_m e_n \qquad (14)$$

where we have used the appropriate transformation to express the square of the radiation electric field in terms of the laser power density W and e_m, e_n, the components of the unit polarization vector $\hat{e}$; therefore,

$$\chi^*_{imn} \equiv [\ 754\ \rho_{ii}/n\ ]\ \chi_{imn} \qquad (15)$$

and

$$T^*_{ijmn} \equiv [\ 754\ \rho_{ii}/n\ ]\ T_{ijmn} \qquad (16)$$

where n is the appropriate refractive index.

The measured open circuit voltage is then

$$V_i = -\int \mathcal{E}_i \, dx_i \qquad (17)$$

where the integration is carried over the illuminated part of the measuring contact separation; thus the tensor coefficient χ, T or χ^*, T^* can be evaluated using Equations (14) and (17). When computing the tensor components from Equation (17), the effects of the appropriate finite radiation absorption, and multiple reflections at the sample surfaces must be taken into account as follows:

(a) For longitudinal measurements

It should be noted that for measurements longitudinal with respect to the radiation propagation direction, the power density W varies along the sample length L as exp-Kx due to the finite radiation absorption coefficient K. Consequently, for longitudinal measurements, using Equation (14) and taking into account multiple reflections at the boundaries of the sample, relation (17) becomes

$$V_i = \frac{(1-R)W_0(1-\exp-KL)}{K}\left\{\frac{\chi^*_{imn}}{1-R\exp-KL} + \frac{T^*_{ijmn}\hat{q}_j}{1+R\exp-KL}\right\} e_m e_n \qquad (18)$$

where W_0 is the incident radiation power density, and R is the reflection coefficient at the air-tellurium interface.

(b) For transverse measurements

In the case of signals measured transverse to the radiation propagation direction, short samples are normally used such that the effect of absorption can be neglected and

the power density is essentially uniform throughout the sample; thus Equation (17) becomes

$$V_i = (1-R)W_0\, d \left\{ \frac{\chi^*_{imn}}{1-R} + \frac{T^*_{ijmn}\, \hat{q}_j}{1+R} \right\} e_m\, e_n \qquad (19)$$

where d is the illuminated distance between the electrical contacts.

Thus one can see from Equations (15), (16), (18), and (19) that even for measurements which involve in principle the same χ or T, the actual magnitude of the measured voltage can vary from sample to sample depending on its particular resistivity and contact separation.

VI 2.2 Effect of Natural Optical Activity

Natural optical activity is the rotation of the radiation electric field polarization direction as the light travels through a material, independent of birefringence effects if the latter exist. This effect is described by the quantity called the "rotary power" r (in degrees per mm) which is a function of the light propagation direction. For light propagation parallel to the optical axis, where clearly no birefringence exists, the effect of the rotary power results in the rotation of linearly polarized light in the plane perpendicular to the optical or c-axis by rz degrees, where z is the distance travelled along the c-axis in millimetres; on the other hand, for light propagating transverse

to the optical axis, optical anisotropy due to the anisotropic refractive index in such materials as tellurium dominates the optical activity, which does not lead in this case to a rotation of the plane of polarization, but produces small changes in the planes of polarization of the ordinary and extraordinary rays {20}.

Thus the effect of optical activity on the measured signals is considered relevant only for experiments where the light propagation direction is parallel to the c or 3-axis.

Considering now specifically those measurements where the light propagation is in the 3 or c direction, for longitudinal measurements in the 3 direction {see Section IV 2.4}, the induced electric field $\mathcal{E}$, using Equations (7), (14), and Table 4b with i = j = 3 and correspondingly m, n = 1 or 2, is found to be independent of the polarization as,

$$\mathcal{E} = - \rho \, [T_{3311} \, \hat{q}_3 \, E_1^2 + T_{3322} \, \hat{q}_3 \, E_2^2] \qquad (20)$$

but since $T_{3311} = T_{3322} \equiv T_3$

$$\mathcal{E} = - \rho \, T_3 \, \hat{q}_3 \, E^2 \qquad (21)$$

where $E^2 = E_1^2 + E_2^2$ is the magnitude of the radiation electric field. It is clear that in this case, optical activity can have no effect on the measured induced signal.

On the other hand, for measurements in a direction transverse to the radiation propagation direction j = 3, it will be shown that a typical contribution to the total induced signal is of the form

$$\mathcal{E} = 2\ A\ E_1\ E_2 = A\ E^2 \sin 2\theta \qquad (22)$$

where $\theta = \tan^{-1} \frac{E_2}{E_1}$ is the angle of the polarization direction with respect to the 1-axis.

Thus, if a linearly polarized plane wave is incident on a tellurium sample of the geometry shown in Figure 12c, such that the radiation polarization direction makes an arbitrary angle θ_0 with the 1 axis at the sample entry face, then, after propagation through a distance z in the crystal having a rotary power r, the angle of polarization θ will become $\theta_0 + rz$ and the induced electric field given in Equation (22) is modified to

$$\mathcal{E}(z) = A\ E^2 \sin 2(\theta_0 + rz) \qquad (23)$$

The average transverse induced electric field over the thickness L of a sample in the direction of light propagation, is

$$\mathcal{E}_{av} = \frac{1}{L} \int_0^L \mathcal{E}(z)\, dz \qquad (24)$$

Since for polarizations perpendicular to the c-axis, absorption may in general be neglected (see Figure 5), it follows that

$$\mathcal{E}_{av} = A\,E^2\,\frac{\sin rL}{rL}\,\sin 2(\theta_0 + rL/2) \qquad (25)$$

For thin samples, i.e. where $rL < 1$ which will be the case in our measurements, $\sin rL/rL \simeq 1$ and

$$\mathcal{E}_{av} \simeq A\,E^2 \sin 2(\theta_0 + rL/2) \qquad (26)$$

Thus it is clearly seen that the effect of optical activity is to displace the normal dependence of the measured induced signal on the angle of polarization by rL/2 degrees.

VI 3.0 Measurement of the Third Rank Tensor Coefficients

VI 3.1 Measurement of χ_{111}, χ_{122}, χ_{212} in Undoped Samples

(a) Magnitude and temperature dependence

The analysis of Section V 4.0 shows that, of the two independent third rank tensor components, only one, represented by the equivalent matrix elements χ_{111}, χ_{122}, and χ_{212}, can be measured separately. It is clear that since the signals associated with the third rank tensor coefficient {see Equation (7)} are independent of the direction of propagation, the measured electrical signals are expected to be independent of the direction of propagation of the laser beam and more specifically they are expected to remain unchanged as a result of the reversal of the beam propagation direction. It follows that the sample geometry shown in Figure 12c, with the laser beam set parallel to the 3 or c-axis, is most suitable for measuring separately all

three equivalent components where the measurement and polarization directions are specified {see Section V 2.0} by the indices of each particular tensor component.

Figure 13 shows a typical variation of the voltage and resistance, obtained in undoped crystals, measured across the shown sample contacts as a function of temperature. For the case when $E \parallel 1$, the signal is clearly proportional to the tensor component χ^*_{111}; the polarity of the signal is found to be, as expected, invariant with respect to the reversal of the beam propagation direction.

Figure (13) for $E \parallel 2$ and Figure (14) show respectively the corresponding results obtained in measuring the matrix elements χ^*_{122} and χ^*_{212}; it is clearly seen that the temperature variation of the magnitude of the signals in all these cases are similar as expected from equivalent third rank tensor components. Also, the polarities of the signals corresponding respectively to χ_{111} and χ_{122} are observed to be opposite in sign, as expected {refer to Section V 2.0}. It is understood that the actual magnitudes of the measured voltages in each experiment depend on such parameters as sample and electric contact geometries, sample resistivity, and incident radiation power density {see Section VI 2.0}. When all the results are normalized to the same conditions of measurement they yield, from Equation (19), essentially equal magnitudes of χ^*_{111}, χ^*_{122}, and χ^*_{212} corresponding to a room temperature value of 0.25×10^{-7} cm/A.

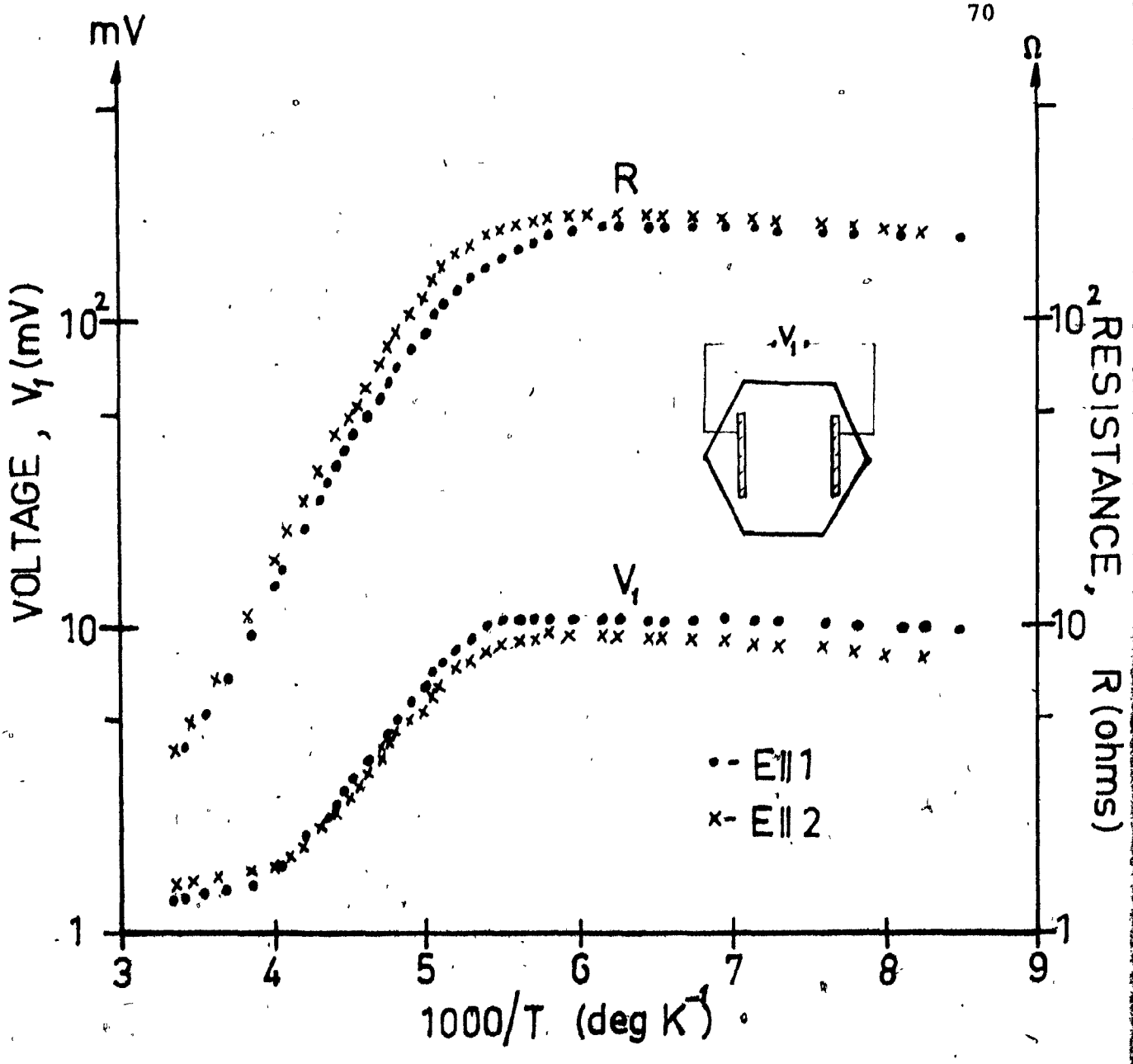

Figure 13. Voltage and Sample Resistance vs Temperature in the measurement of χ^*_{111} and χ^*_{122}.

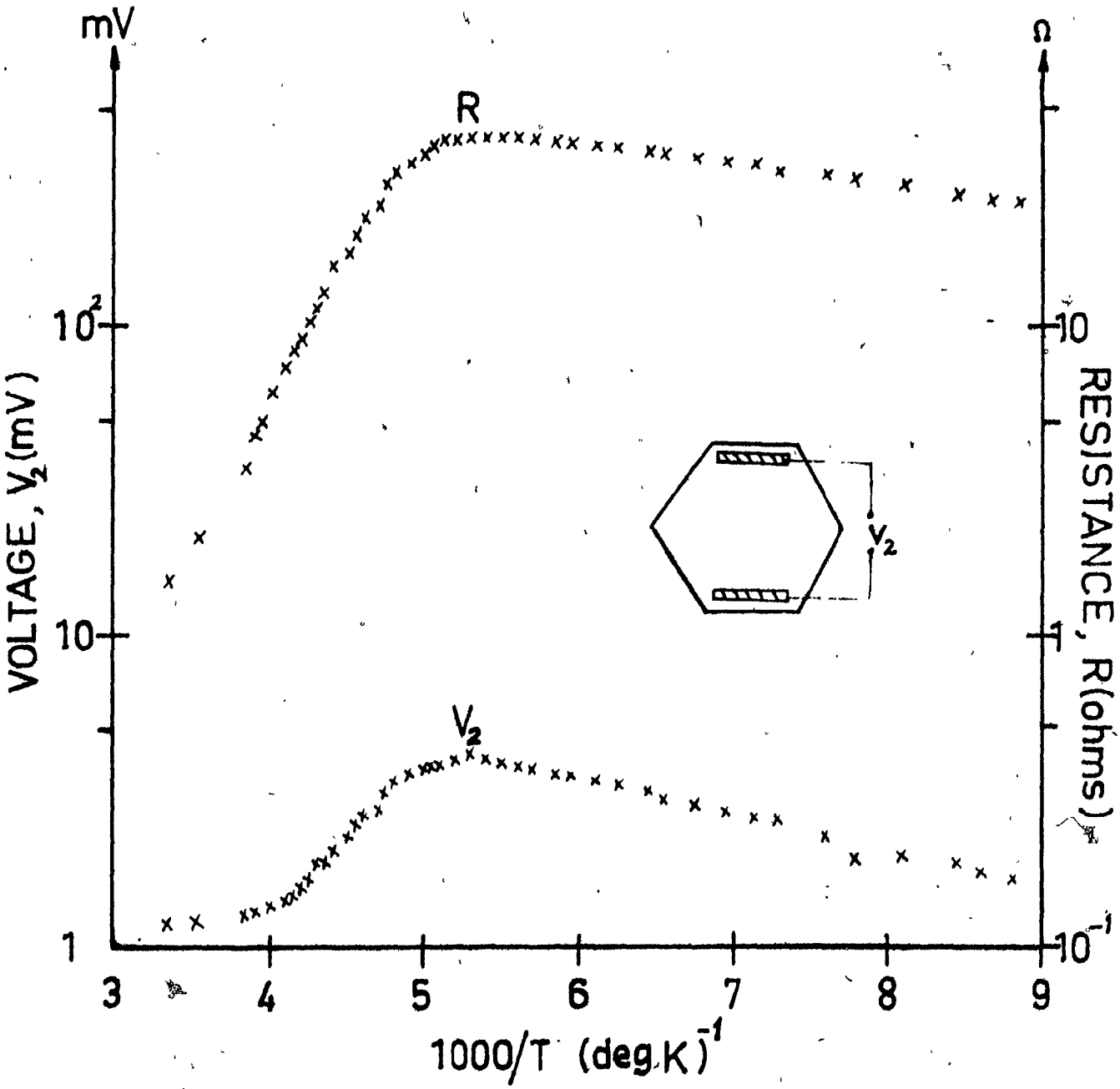

Figure 14. Voltage and Sample Resistance vs Temperature in the measurement of χ^*_{212}.

(b) Variation of the induced voltages with variation of the incident polarization direction θ_0

When the laser beam is linearly polarized in the plane perpendicular to the c-axis and thus is propagating parallel to the 3 or c-axis in a sample with the contact geometry shown in Figure 12c; Equation (7), for the rectified measured signal in the 1 direction, becomes,

$$J_1 = \chi_{111} E_1 E_1 + \chi_{122} E_2 E_2 + 2 T_{1312} E_1 E_2 \quad (27)$$

$$= \chi_{111} E^2 \cos^2 \theta + \chi_{122} E^2 \sin^2 \theta + 2 T_{1312} E^2 \cos \theta \sin \theta \quad (28)$$

Since from symmetry (refer to Section V 2.0) $\chi_{111} = -\chi_{122} = -\chi_{212} \equiv -\chi$ and $T_{1312} = T_{2311} = -T_{2322} \equiv T$, Equation (28) reduces to

$$J_1 = \chi E^2 \cos 2\theta + T E^2 \sin 2\theta \quad (29)$$

Similarly for measurements in the 2 direction

$$J_2 = \chi E^2 \sin 2\theta + T E^2 \cos 2\theta \quad (30)$$

Figure 15 shows a typical variation of the measured signals on the same sample corresponding to J_1 and J_2 as the polarization direction of the radiation electric field is rotated about the c-axis. This measured polarization dependence of the induced signals clearly follows closely the angular dependence of the χ terms in Equations (29) and (30);

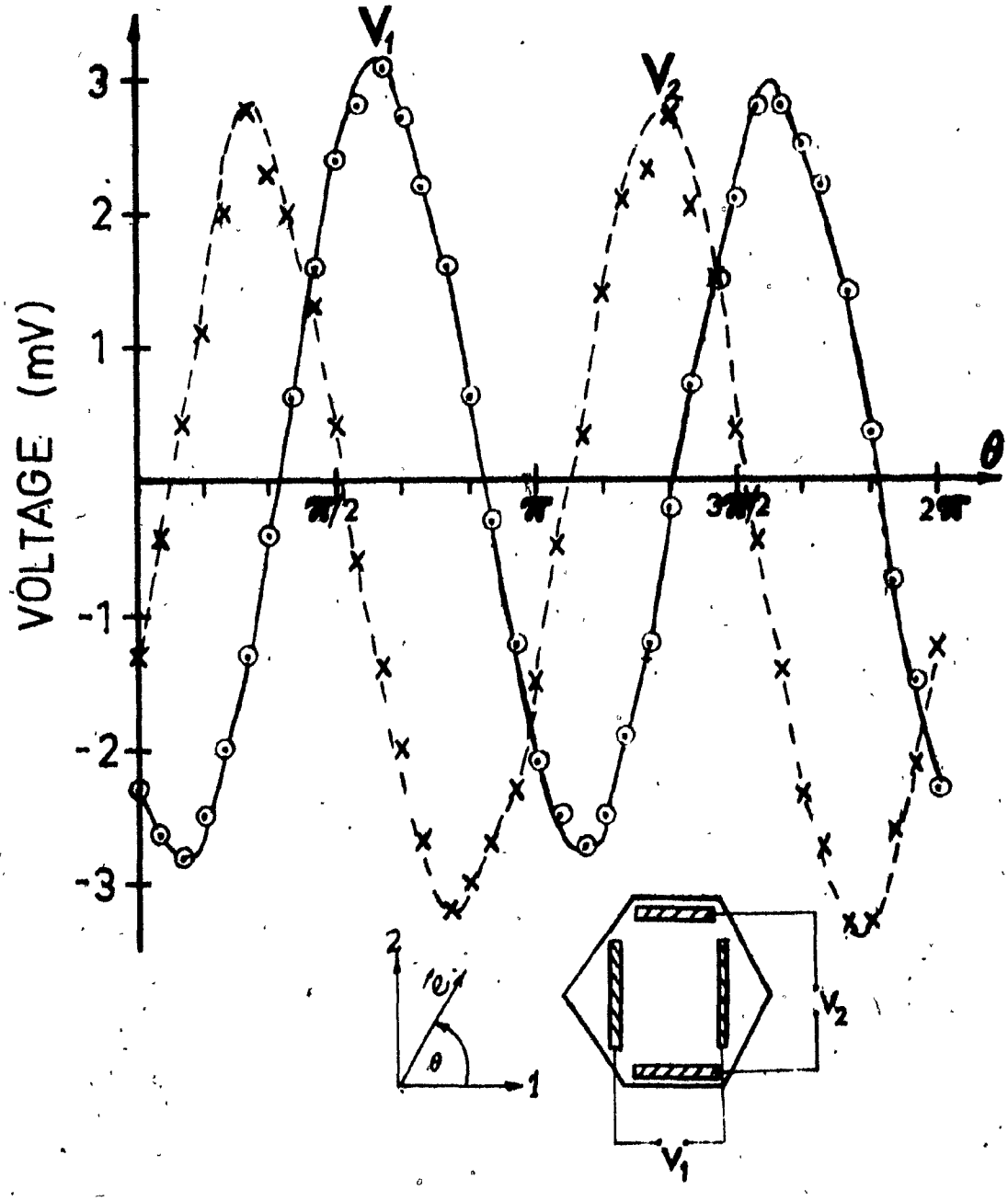

Figure 15. Variation of the Third Rank Tensorial Signal with Angle of Polarization θ.

this implies that the contributions to the measured signals from the terms proportional to the fourth rank tensor component T are relatively small. In fact, it is found that for the angles $\theta = (2n + 1)\frac{\pi}{4}$ and $n\frac{\pi}{2}$, $n = 0, 1, 2...$ Equations (29) and (30) predict respectively that the contribution of the fourth rank tensor terms, if finite, would be maximum and correspondingly the third rank tensor terms zero; since the measured induced signals at these angles are found not to reverse their polarity with a reversal in the light beam propagation direction, it is concluded that within experimental accuracy, the equivalent fourth rank tensor components T_{2311}, T_{2322} which correspond to the transverse photon drag effect for the measurement conditions specified by their indices, are essentially zero.

On the other hand, the shifting of the observed maxima and minima points from the angles of θ equaling the expected values $n\pi/4$ where $n = 0, 1, 2....$ is readily explained by considering the effect of optical activity on the measured signal as described in Section VI 2.0. Using the results of the latter section, Equations (29) and (30), when modified to include the rotary power and eliminating the negligible term T, yield the following expressions:

$$J_1 = \chi E^2 \cos 2(\theta_0 + rL/2) \tag{31}$$

and

$$J_2 = \chi E^2 \sin 2(\theta_0 + rL/2) \tag{32}$$

The shifting in the angular dependence, obtained from Figure 15, is about 15^{o} which yields, for the sample thickness L = 2.5 mm, a rotary power of -12^{o}/mm which agrees favourably with the optical activity data obtained in tellurium from independent measurements presented in Section III 5.2.

VI 3.2 Measurement of χ_{111}, χ_{122}, χ_{212} in Doped Samples

A typical temperature variation of the resistance and induced voltage in doped samples corresponding to the equivalent matrix elements χ^{*}_{111}, χ^{*}_{122} and χ^{*}_{212} is shown in Figure 16. It is clearly seen that the temperature characteristics of the measurements are vastly different from those obtained in the undoped samples (Figure 15). Furthermore the magnitude of this coefficient χ^{*} in doped crystals at room temperature is evaluated to be 0.7×10^{-7} cm/A, which is approximately three times larger than that measured in undoped samples.

VI 3.3 Measurement of χ_{123} and χ_{231}

The other independent third rank tensor component, represented by the equivalent matrix elements χ_{123} and χ_{231}, will be evaluated following the presentation of the fourth rank tensor coefficient measurement, since as shown by Equations (12) and (13), these elements always appear in combination with at least one fourth rank tensor component.

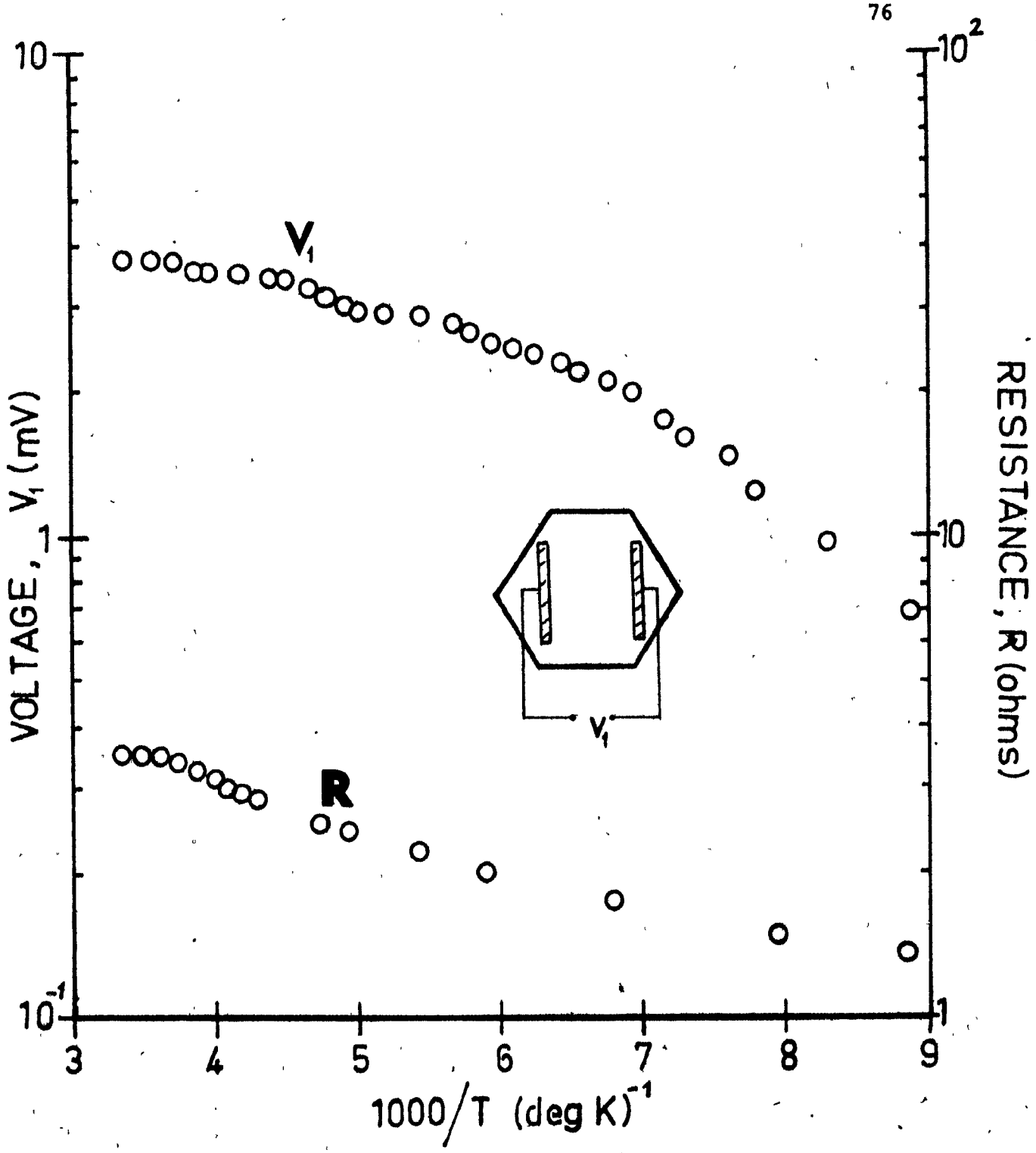

Figure 16. Voltage and Sample Resistance in Extrinsic Samples for the Measurement of χ.

VI 3.4 Conclusions

In summary, the results of the measurements presented in this section, clearly indicate the existence of radiation induced electric signals which are generated by an effect characterized by a third rank tensor coefficient; one of the two independent components has been measured and found to be consistent with the symmetry properties of tellurium. In the process, it has also been established that the transverse photon drag effect in tellurium for light propagation parallel to the c-axis is, within experimental accuracy, essentially zero.

VI 4.0 Measurement of the Fourth Rank Tensor Coefficients: The Photon Drag Effect

VI 4.1 Introduction

In the following section the measurement of the fourth rank tensor coefficients which describe the Photon Drag effect will be presented; in particular the magnitude and the temperature variation of the induced voltages arising from the coefficients, which were previously {see Section V 3.0} classified into Sets 1 to 6, will be investigated.

It was found that in the course of these measurements, fast signals from a source other than the photon drag effect and that characterized by the coefficient χ may also

appear; in the following sections such signals, when present, will be identified, but their detailed discussion will be undertaken in Section VI 8.0.

VI 4.2 The Fourth Rank Tensor Components of Set 1, $T_{2233} = T_{1133}$: The Longitudinal Photon Drag Signals with E || c

VI 4.2.1 Measurement in undoped samples

The induced voltages were obtained on rectangular samples (see Figure 12a) in which the long dimension was appropriately oriented either parallel to the 2 direction for measuring T_{2233}, or parallel to the 1 direction to obtain T_{1133}. A typical temperature variation of the measured voltage, corresponding to the induced signal associated with the longitudinal fourth rank tensor component T^*_{2233} or equivalently T^*_{1133}, and the sample resistance in undoped tellurium, is shown in Figure 17.

The polarity of these signals corresponds to a generated short circuit current in the direction of light propagation, thus a reversal in the laser beam propagation direction results in a reversal in the polarity of the monitored voltage consistent with the expected behaviour of the photon drag effect. It may be noted that the variation of both the photon drag signal and the sample resistance with temperature are initially identical as the temperature

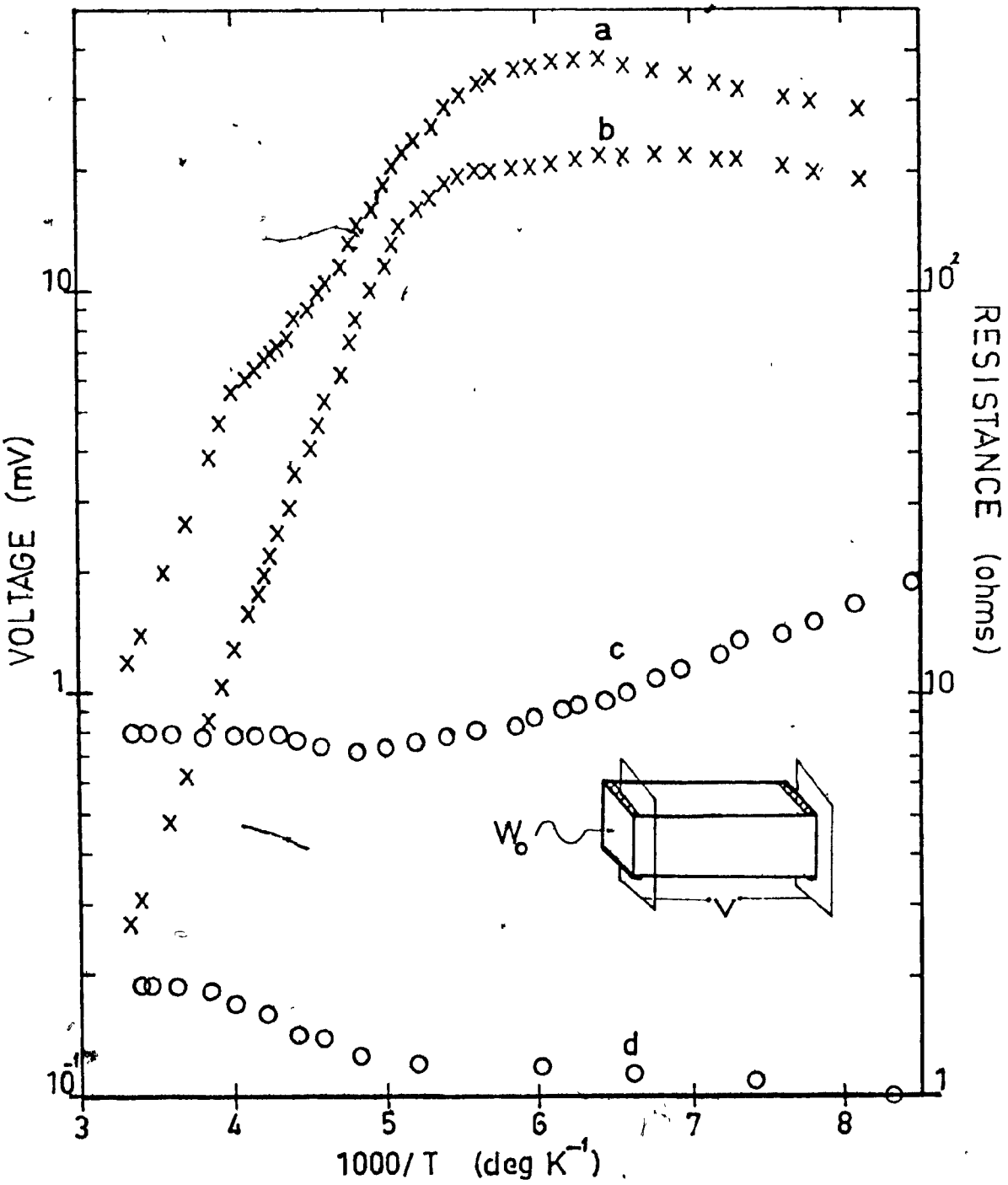

Figure 17. Measured Longitudinal Photon Drag Signals with E || c

a) open circuit voltage in undoped material
b) sample resistance in undoped material
c) open circuit voltage in extrinsically doped material
d) sample resistance in the doped material.

is lowered below 300 K. At room temperature, these measurements are clearly equivalent, with identical results, to the preliminary observations presented in Section IV 3.2a with E || c . For samples of more than 5 mm in length, the longitudinal open circuit voltage with E || c at room temperature is consistently found to be 10 mV for an incident power density of 1 MW cm^{-2}; this responsivity, using Equation (18), leads to a value of $T^*_{2233} = T^*_{1133} = 0.85 \times 10^{-7}$ cm/A.

VI 4.2.2 Measurement in doped samples

The variation with temperature of the generated longitudinal photon drag signal and of the corresponding sample resistance with E || c in extrinsically doped p-type samples, is shown in Figure 17c,d. Clearly it is seen that, in comparison with the corresponding signals induced in undoped intrinsic samples, the generated voltage in extrinsically doped samples is relatively constant over the entire temperature range. It should be noted, however, that for both undoped and doped samples, Figure 17a and 17c respectively, show a noticeable increase in the measured voltages at the same temperature of about 220 K. The magnitude of the generated longitudinal voltage for E || c in our extrinsically doped tellurium crystals is found, at room temperature to be slightly lower than the corresponding measured signal in undoped samples; $T^*_{2233} = T^*_{1133}$ is evaluated in this case to be 1.1×10^{-7} cm/A.

VI 5.0 The Observation of an Additional and Unexpected Generating Mechanism

VI 5.1 Introduction

At this point, the existence of an unexpected signal source, which also reproduces faithfully the laser output pulse, must be reported as it is found to appear in many of the further measurements to be presented in this chapter. The various characteristics of this unexpected signal are observed best in transverse measurements with the light propagation direction being parallel to the 2-direction. Thus in the following paragraph a series of measurements are prescribed which establish definitely that in the observed signals there exists a contribution from a mechanism other than the fourth rank and third rank tensorial effects. This mechanism will be further investigated in Section VI 8.0.

VI 5.2 Measurements With the Light Propagation in the 2-direction

VI 5.2.1 Measurements in undoped samples

(a) Measurement in the 3-direction; polarization in the 1-direction

The attempt to obtain in undoped samples the induced signal corresponding to the transverse fourth rank tensor

T_{3211} of Set 5, using the sample geometry shown in Figure 12d, results in an observed voltage whose magnitude varies as a function of temperature according to Figure 18. It is established, most importantly, that this generated electrical signal does not reverse its polarity with a reversal in the laser beam propagation direction; thus this signal can definitely not be attributed to the photon drag effect.

The magnitude of this signal is seen to increase rapidly by several orders of magnitude as the temperature is decreased from room temperature to approximately 125 K, after which the magnitude becomes relatively constant down to the lower temperature limit of the cooling apparatus. The general temperature characteristics of this induced signal is distinctly different from the third rank tensorial and longitudinal photon drag signals described in Sections VI 3.1a and VI 4.2 respectively. For completeness, measurements were also performed for the remaining combinations of measurement and polarization directions that are possible for this sample geometry.

(b) Measurements in the 3 and 1-directions with polarization in the 3-direction

The measurements which were performed on the same and other identically cut samples for the conditions described by the fourth rank tensor component index combination 3233 and 1233 {see Section V 2.0}, revealed similar signals

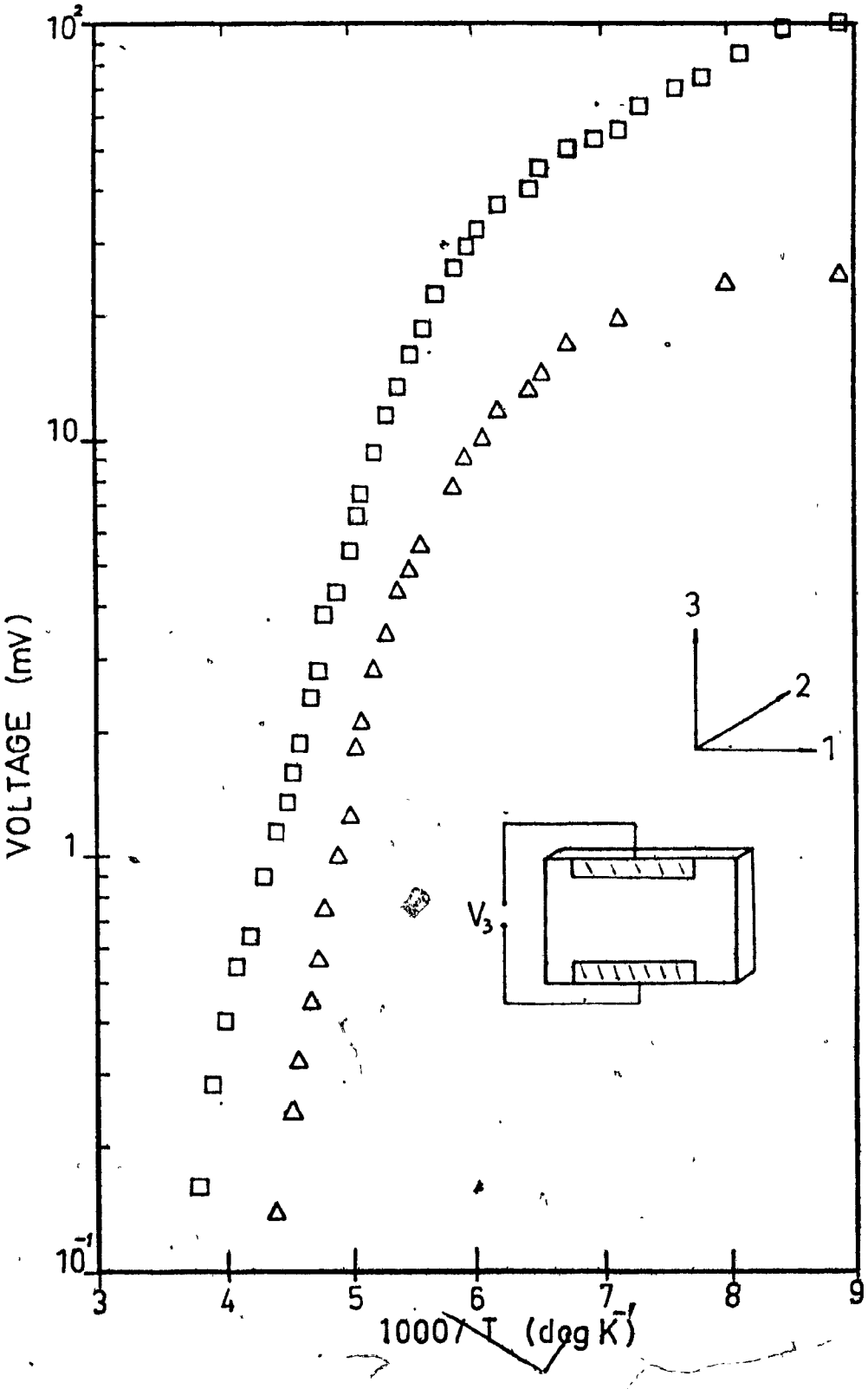

Figure 18. Temperature Dependence of the Spurious Signal.

□ - for polarization E || 3,

△ - for polarization E || 1.

of the same polarity; in these measurements where the light is polarized parallel to the c-axis, the induced signals at low temperatures are found to be four or five times larger than those generated with $E \perp c$, see Figures 18 and 19.

It is noted that these signals appear in conditions where the combination of measurement, propagation, and polarization directions require that, from symmetry considerations, both the corresponding third and fourth rank tensor components such as χ_{333}, T_{3233}, χ_{133} and T_{1233} be identically zero {refer to Table 4b}; therefore, it can be definitely concluded that the presence of this signal is due to an entirely different and additional mechanism which cannot be simply characterized by either third or fourth rank tensorial behaviour.

(c) Measurement and polarization in the 1 direction

This combination of measurement and polarization directions is expected to produce signals proportional to the third rank tensor coefficient χ_{111} while the corresponding fourth rank tensor coefficient T_{1211} is identically zero, {see Table 4b}. In the results of this measurement shown in Figure 19 for $E \parallel 1$, one observes, a finite signal at room temperature which remains at first essentially constant as the temperature is lowered, then, decreases in magnitude, eventually passes through zero, reverses its polarity and subsequently increases once again to a relatively large magnitude.

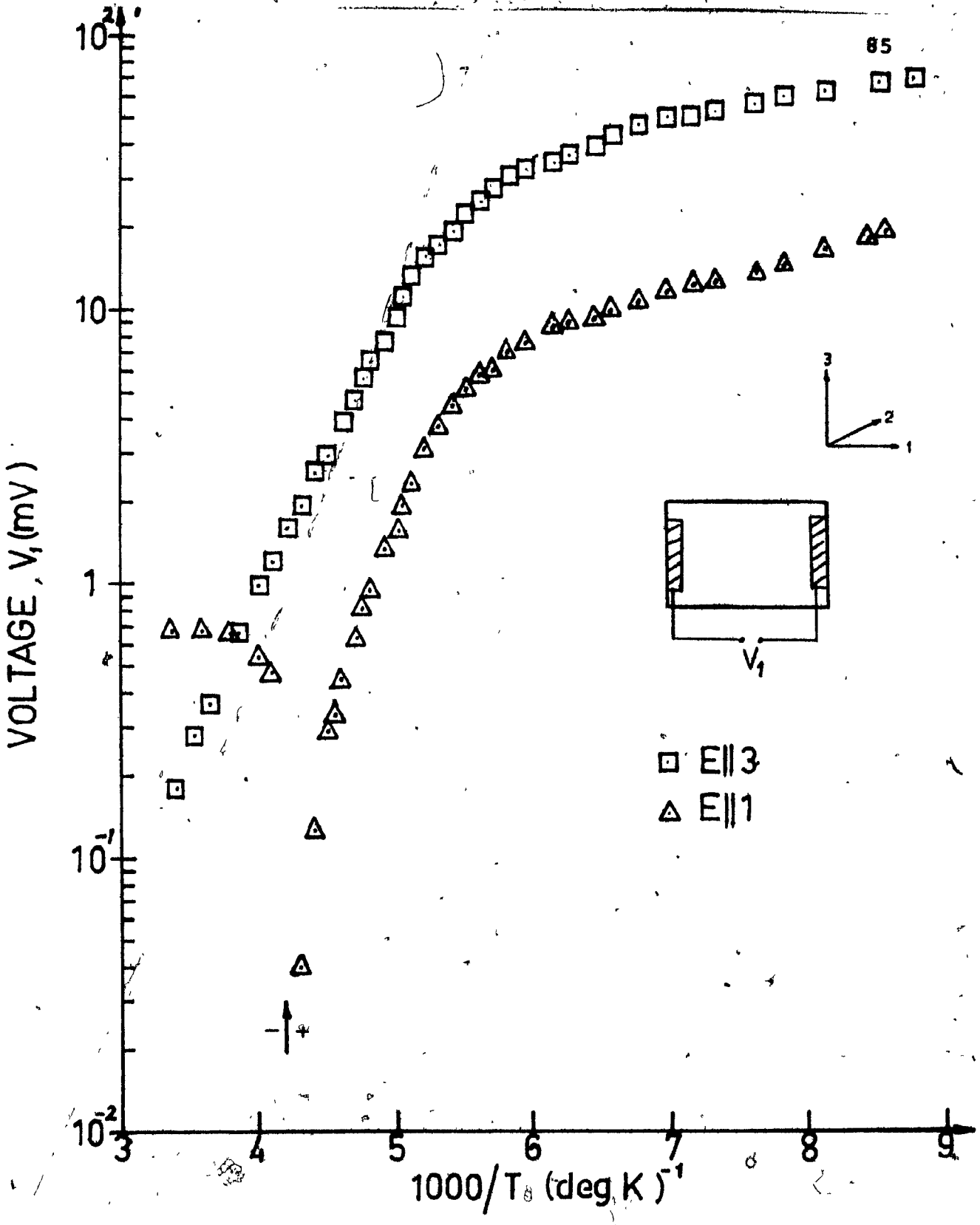

Figure 19. Transverse Measurements in the 1 direction.

Radiation propagation is in the 2 direction.

Arrow indicates polarity inversion temperature when E || 1.

It can be easily surmised that, originally near room temperature, the observed signal is the one which is associated with the effect described by the third rank tensor component χ_{111}, as expected from Table 4b; but as the temperature is further decreased, a different signal of opposite polarity dominates the total response. In fact, a careful examination of the results, shows that the observed signal, in this case, is the algebraic sum of two different signals, one of which corresponds to the mechanism described by the third rank tensorial coefficients. When the temperature behaviour of the magnitude of the signal associated with the expected component χ_{111}, originally established in the measurements with the laser beam propagation in the 3-direction {see Section VI 3.0}, is subtracted from this present complex signal, the resulting signal's temperature characteristic is clearly identical to the one described in the previous paragraphs and Figure 18, or Figure 19 for E || 3 .

5.2.2 Measurement in doped samples

For the transverse measurements with the laser beam propagating in the 2-direction in doped samples, no evidence of the large additional and unexpected signal is observed at any temperature for all the combinations of measurement and polarization directions. The only finite signal is observed under the condition associated with the component χ_{111}; its

magnitude and temperature behaviour is identical as expected to the corresponding measurement with the light propagation direction in this case in the 3-direction, described for doped samples in Section VI 3.2; this confirms that the third rank tensors components are independent of the actual light propagation direction.

Having introduced and established the existence of a third generating mechanism, the experiments performed to obtain the remaining fourth rank tensor components are now described.

VI 6.0 The Fourth Rank Tensor Components of Set 2

VI 6.1 The Longitudinal Photon Drag Component T_{2211}

This longitudinal measurement was performed on samples with the geometry shown in Figure 12a in which the long dimension is up to 1.7 cm in length and is parallel to the 2-direction.

With an incident power density of 300 KW cm^{-1}, the magnitude of the induced voltage corresponding to T_{2211}, the only fourth rank tensor component of Set 2 which is measurable separately {Section V 4.0}, is found at room temperature to be below 50 μV, the lower limit of the experimental measurement capability. At temperatures below approximately 250 K, only spurious signals were observed; they are considered to

originate in part from fractional contributions from the large signals associated with the components T_{2233}, χ_{212}, and, in undoped samples, particularly from the additional signal described in Section VI 5.0, all of which may appear due to the unavoidable sample, measurement, propagation, and polarization directions misalignment, in an actual experiment, with respect to the true crystallographic axes of the tellurium crystal. Is is thus evaluated that, at room temperature where $K \simeq 0.2\ cm^{-1}$, T_{2211} is less than 1.5×10^{-9} cm/A for both intrinsic and extrinsic samples.

VI 6.2 The Longitudinal Component T_{1122}

VI 6.2.1 Measurement in undoped samples

When using the measurement conditions applicable for obtaining the other equivalent component T_{1122} of Set 2, Equation (7) and Table 4b predict that the induced signal has an additional contribution from the third rank tensor component χ_{122}. In fact, one observes a relatively large signal which does not reverse in polarity with a reversal in the light propagation direction; furthermore, its magnitude is consistent with the measurements of the χ_{122} component described in Section VI 3.1 where the measurement of this component was obtained with the laser beam propagating in the 3-direction. Consequently this agreement confirms that within experimental accuracy, the longitudinal photon drag

effect in the 1 and 2 directions with polarizations $E \perp c$ is negligible. In addition, this measurement further confirms the fact that the induced signal due to the third rank tensor coefficients is independent of the light propagation direction and depends only on the measurement and polarization directions.

VI 6.2.2 Measurement in doped samples

The longitudinal photon drag signal corresponding to the tensor component T^{*}_{1122} in doped samples is found to be completely masked by the large signal generated by the effect characterized by the third rank tensor coefficient χ_{122}; this fact prohibited the determination of the magnitude of T_{1122}.

VI 6.3 The Fourth Rank Tensor Components of Set 3, $T_{3311} = T_{3322}$

VI 6.3.1 Measurements in undoped samples

The equivalent fourth tensor components T_{3311} and T_{3322} of Set 3 correspond to longitudinal signals measured along the 3- or c-axis with the radiation polarized perpendicular to the c-axis. Experimentally, no signals which could be attributed to the photon drag effect were observed in undoped crystals over the entire temperature range. However, spurious signals were observed which were sensitively dependent on the exact alignment of the sample relative to the incident laser beam and thus were considered as

remnants of the other larger signals previously described. Thus within experimental accuracy and for undoped crystals the components T^*_{3311} and T^*_{3322} are estimated to be below 1.5×10^{-9} cm/A.

VI 6.3.2 Measurement in doped samples

In a doped sample, a finite signal was obtained whose magnitude variation with temperature is shown in Figure 20. It is seen that the magnitude of the signal is fairly constant over the entire temperature range. At room temperature with $W_0 = 330$ KW cm^{-2}, the induced voltage is found to be 0.7 mV; in this case $K = 0.27$ cm^{-1}, $R = 0.43$, therefore Equation (18) gives $T^*_{3311} = 0.4 \times 10^{-8}$ cm/A $= T^*_{3322}$.

IV 6.4 The Fourth Rank Tensor Components of Set 4

In both undoped and doped samples, the three equivalent transverse fourth rank tensor elements of Set 4, T_{2311}, T_{2322}, T_{1312}, were found in the process of measuring the third rank tensor components χ_{212}, χ_{111}, χ_{122}, as described in Section VI 3.1b, to be, within experimental accuracy, essentially zero.

VI 6.5 The Fourth Rank Tensor Components of Set 6

As stated in Sections V 3.0d and V 4.0, the two components of Set 6, T_{1123} and T_{1231} always appear in a linear

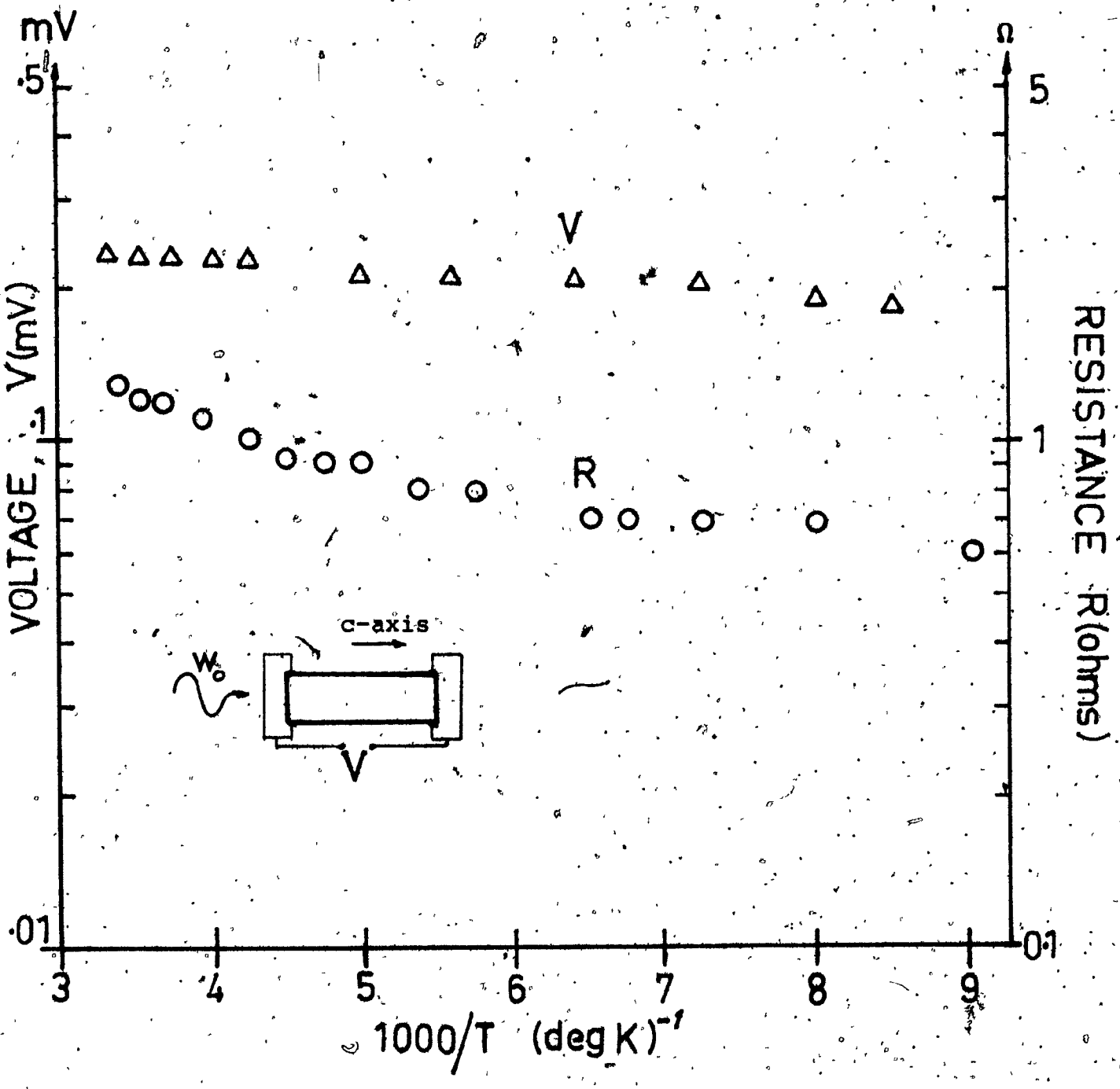

Figure 20. Measured Sample Resistance and Longitudinal Photon Drag Voltage Parallel to the c-axis in an Extrinsic Sample.

combination with either another fourth or third rank tensor component and thus cannot be measured separately, but can only be obtained, in principle, by taking differences of at least two sets of measurements.

In the case of the element T_{1123}, the simultaneous presence of the signals originating from both the large components T_{1133} and χ_{122}, account completely for the obtained response; on the other hand, one observes only the expected contribution of the χ_{111} component when attempting to measure T_{1231}. Thus within experimental accuracy, the two components of Set 6, T_{1123} and T_{1231}, are estimated to be zero in both undoped and doped crystals.

VI 7.0 The Third Rank Tensor Components χ_{123}, χ_{231}

As shown by Equations (12) and (13) in Section V 4.0, both the equivalent matrix elements χ_{123}, χ_{231} of the second of only two independent third rank tensor components, always appear, in appropriate measurements, in linear combination with signals originating from at least one fourth or the other third rank tensor component. When attempting to measure signals due to χ_{231}, it is found that the contribution from the fourth rank tensor component T_{2233} dominates entirely the response; while in the case of χ_{123}, both the T_{1133} and χ_{122} components affect the total measured voltage. Within experimental accuracy, the χ_{123} and χ_{231} equivalent

components are evaluated to be of zero magnitude for both doped and undoped tellurium crystals.

VI 8.0 The Spurious Low Temperature Signal

VI 8.1 Introduction

The experimental results presented in Section VI 5.0 clearly indicate the existence of a third mechanism by which the radiation generates a fast emf in tellurium. We now present the observed characteristics and behaviour of this additional and originally unexpected effect, called from now on the spurious signal, as a function of the direction of measurement, radiation polarization and propagation; the magnitude variation with temperature will also be presented.

VI 8.2 General Characteristics

1) The emf induced by this third mechanism is within experimental accuracy instantaneously and linearly related to the laser radiation pulsed output power.

2) It must be emphasized that the magnitude of the spurious signal differs from sample to sample; the magnitude at low temperature ranges from essentially zero to in excess of 3V/MW cm^{-2} depending on the sample used. This variation in magnitude is in sharp contrast to the case of the photon drag effect and the third rank tensorial

effect both of which give consistent results in all samples.

3) It is always found, on the other hand, that the magnitude of the spurious signal is largest at low temperatures and has always the temperature dependence shown in Figure 18, i.e. its magnitude starts from essentially zero and increases rapidly by several orders of magnitude from room temperature down to approximately 125 K, below which temperature it becomes relatively constant.

4) The polarity of the induced signal does not invert with a reversal in the direction of light propagation.

5) For a given measurement and propagation direction, the measured voltage for radiation polarized parallel to the c-axis is always 4 to 5 times larger than for $E \perp c$; the polarities of the generated emfs are identical for both polarizations.

6) In doped crystals, the signal has essentially not been observed.

VI 8.3 Variation with the Crystal Orientation Relative to the Incident Beam

The results from the complete set of measurements, consisting of all the combinations of directions of measurement, polarization, and propagation along the major axes of

the crystal indicate that the behaviour of the spurious signal cannot be characterized by a tensor of any rank consistent with the symmetry properties of tellurium. In addition, experiments performed on different samples of identical geometry and orientation with respect to the laser beam, do not necessarily produce similar results.

We report in the following paragraphs the observations recorded concerning the dependence of this spurious low temperature induced signal on the orientation of the crystal sample relative to the incident beam.

1) With the sample geometry shown in Figure 12d, in which the laser beam is propagating parallel to the 2 direction, a substantial induced transverse emf has always been observed in all samples for measurements made along the 1 or 3 directions. The signal, as stated earlier, is preferential for polarizations parallel to the c-axis. For a usual contact separation of 5 mm and with an incident power density of 120 KW cm^{-2} the transverse measurements with E || c at temperatures lower than 150 K resulted in a voltage signal varying from 40 to in excess of 300 mV depending on the sample used.

2) On the other hand, using a similar sample geometry in which, in this case, the radiation is propagating along the 1 axis and the transverse emfs are measured in

either the 2 or 3 directions, some samples have exhibited signals while others have not. The measured voltage on the different samples have ranged from essentially zero to approximately 50 mV. In a number of these cases where finite emfs have been observed, the magnitudes are found not to be linear functions of the incident power and furthermore, in some instances, the monitored pulse is very structured {refer Section IV 1.2} indicating perhaps that only a small area of the sample is active in producing the induced signal.

3) This spurious signal has not been observed when the radiation propagation direction is in the 3 direction, i.e. parallel to the c-axis: for this propagation direction, in the case of transverse measurements, only the signal with the third rank tensorial behaviour is observed as reported in Section VI 3.0 and whose temperature dependence is shown in Figure 13; on the other hand, in longitudinal measurements, at low temperatures, signals that do not exceed a few millivolts and which cannot be identified with this spurious effect, are monitored; therefore, it is considered that the spurious signal is essentially not induced when the radiation is propagating parallel to the c-axis.

4) This spurious signal appears also in conjunction with other signals found in longitudinal measurements along

the 1 or 2 directions with the radiation polarized both parallel and perpendicular to the c-axis. The above conclusion has been arrived at due to the following observations:

a) In the case $E \parallel c$, occasionally the temperature dependence of the measured induced voltage across the sample is observed to be as shown in Figure 21; the two shown curves from experimental points are obtained by illuminating in turn each of the two ends of the sample. It is seen that the two sets of results, corresponding respectively to radiation propagation in opposite directions, demonstrate that within approximately 60^{o} of room temperature, the measured voltages are of equal magnitude but of opposite polarity; then as the temperature is further lowered, one signal continuously increases in magnitude, whilst the other decreases in magnitude passing through zero, and finally increases once again, but with a reversed polarity.

The temperature at which one of the signals reverses its polarity varies from sample to sample from as high as 250 K to lower than our lowest temperature of measurement where no such assymetry in the measured signal for the two ends of sample is observed as is seen in Figure 17a.

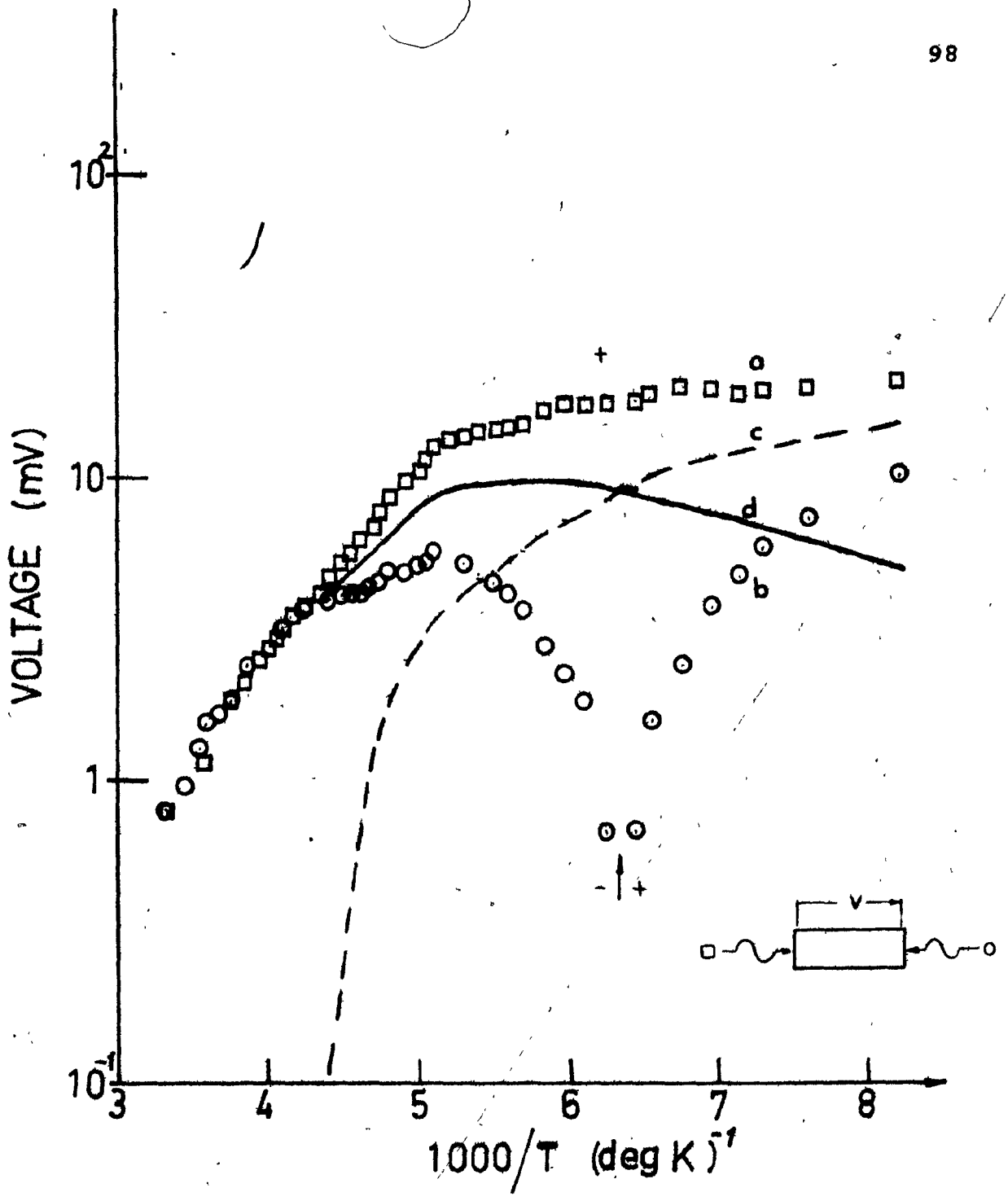

Figure 21. Temperature Dependence of the Combined Photon Drag and Spurious Signal.

a - corresponds to light propagating in a given direction, and

b - corresponds to the reverse direction; arrow indicates signal polarity inversion for this light propagation direction.

c - algebraic sum of curves a and b.

d - algebraic difference of curves a and b.

In order to facilitate the interpretation of these results, the sum and difference of the two sets of experimental points in Figure 21 are taken and the corresponding results are represented respectively by the two line curves in the same figure. By inspection it is clear that the measured signals are composed of two separate signals, one reverses its polarity with a reversal in the propagation direction and is the expected photon drag signal characterized by the equivalent fourth rank tensor components T^*_{1133}, T^*_{2233}; the other signal is independent of radiation propagation direction reversal and furthermore has a temperature dependence identical with that of the low temperature spurious signal (see Figure 18) reported in Section VI 5.

b) In the case of longitudinal measurements with $E \perp c$, the spurious signal is observed at the low temperatures, with amplitudes that vary from essentially zero to approximately 40 millivolts depending on the sample measured. When the longitudinal measurement is made in the 1 direction, the spurious signal appears in combination with the expected emf generated by the mechanism characterized by the third rank tensor component χ_{122}.

VI 8.4 Dependence of the Signal on Sample "Aging"

In many cases, it is important to note that the spurious signal is observed to increase in magnitude after the tellurium sample under test has gone through repetitive cooling cycles, called herewith "aging". The "aging" process is characterized in our experiments by a noticeable increase in the sample resistance, normally in the order of a ten percent change for each cooling cycle. This effect has been also previously reported by Caldwell {33}. During "aging", it is believed that non-uniform thermal expansion or contraction of the sample probably introduces internal stresses of sufficient magnitude to incur defects and or dislocations in the relatively weak tellurium crystal structure which lead to a decrease in the carrier mobility and even, in extreme cases, we have observed the presence of visual minute fractures or cracks in the sample.

VI 8.5 Discussion and Conclusions Concerning the Low Temperature Spurious Signal

We have presented in Section VI 8 a set of careful experimental observations and hence the characteristics of the unexpected signal which is considered to be spurious in nature since its occurrence and magnitude for the same sample measurement geometry, vary substantially from sample to sample.

The main features of this spurious signal are that it has been observed only in undoped tellurium samples; its magnitude is largest at temperatures below 150 K being essentially zero at room temperature; the signal is preferential for polarization E || c. This signal is always prevalent in transverse measurements having the radiation propagation direction parallel to the 2-direction, whereas its presence is not apparent for propagation direction along the c-axis.

Attempts to characterize or associate phenomenologically this signal with a third or fourth rank tensorial effect fails since it appears in many situations where the latter effects are expected to be identically zero due to crystal symmetry conditions. Furthermore, this signal cannot be related to any of our measured third and fourth rank tensorial effects, since its temperature dependence is distinctly different from the latter. In fact, in some instances, as shown by Figures (19) and (21), it has been shown that this spurious signal appears in combination with the expected third and fourth rank tensorial emfs. Also, our results for this emf do not fit phenomenologically the tensorial behaviour of fifth rank tensor coefficients, nor the two and three step processes involving third and fourth rank tensor coefficients, such as would be associated with the physical mechanisms dealt with in References {34} and {35}.

It is important to note that this low temperature spurious signal was often observed to appear in samples, which originally did not exhibit such a signal, after they were subjected to a damage mechanism such as cooling and heating cycles; the latter are known to introduce in the relatively weak tellurium single crystal structure, internal stresses and consequently dislocations and defects which manifested themselves by an observed sample resistivity increase as well as by the appearance of microcracks in extreme cases. It is therefore concluded that it is most likely that the signal results from crystalline imperfections in the tellurium single crystal structure.

VI 9.0 Conclusions

In this chapter we have presented the results of a comprehensive set of measurements designed to obtain the expected third and fourth rank tensor coefficients describing respectively the optical rectification and photon drag emfs induced in tellurium by TEA CO_2 laser pulsed radiation. In the process, the existence of an unexpected low temperature spurious signal has clearly been established and its characteristics described.

Specifically it has been found, that for the photon drag effect, the only tensor components of significance are $T^*_{1133} = T^*_{2233}$ which in undoped and doped crystals, at room

temperature, are respectively equal to 0.85×10^{-7} cm/A and 1.1×10^{-7} cm/A. In the case of the third rank tensor coefficient, only the equivalent components $\chi^*_{122} = \chi^*_{212} = -\chi^*_{111}$ are large and, at room temperature, have the magnitude of 0.25×10^{-7} cm/A and 0.7×10^{-7} cm/A in undoped and doped tellurium crystals respectively.

CHAPTER VII

THE SIGNAL WITH THE FOURTH RANK TENSOR BEHAVIOUR

THE PHOTON DRAG EFFECT IN TELLURIUM

VII 1.0 Introduction

When radiation is absorbed by free carriers in a semiconducting material, photon momentum as well as energy is transferred to the free electrons and holes consistent with the principle of conservation of energy and momentum during the interaction process. Consequently the directionality of the photon beam from a laser source causes the system of electrons of the radiation absorbing semiconductor to acquire translational motion relative to the crystal lattice which results in the so called "photon drag" signal in the form of a flow of electric current or the generation of a voltage under short or open circuit condition respectively. As this effect is directly proportional to the photon momentum, the photon drag signal inverts its polarity with a reversal in the direction of propagation of the laser beam, and this unique feature is used to distinguish it from other possible competing signals generated concurrently in the material (see Chapter V).

The phenomenological behaviour of the photon drag effect as a fourth rank tensor was presented in Chapter V; in Chapter VI a series of carefully performed experimental observations have allowed the measurement of the actual

magnitude of this signal in tellurium, as well as its variation with different physical parameters associated with the samples under investigation.

In the present chapter a detailed analysis of the different physical processes involved in the generation of the photon drag signals in tellurium will be presented; this will allow the discussion later of the experimentally observed results and to derive, from the latter, information on certain relevant physical parameters in tellurium.

VII 2.0 General Remarks

The photon drag effect results from an interaction between the photons in the laser beam and the free carriers in the semiconductor corresponding to a photon absorption process; thus the exact nature and type of absorption is expected to be important in determining the magnitude and behaviour of the photon drag signal. Absorption of photons, in general, occurs as a result of photon energy induced electronic direct interband transitions as well as indirect intraband transitions; in general, it has been shown that a photon drag signal can arise from any type of photon induced electron transitions such as, either electron {36} transitions across the energy band gap of a semiconductor, or, absorption due to the ionization of deep impurity centers {37}; however, the photon drag effect is only attractive as a detection mechanism for relatively long wavelength, short

duration laser radiation pulses, this is why this work investigates the consequences of absorption of sub-band gap energy photons by free carriers where only intervalence band or intraband transitions are dominant {see Section III 6.2.2}.

The development of the theory of the photon drag effect in a semiconductor such as tellurium under excitation by a sub-energy gap photon beam will be presented in this chapter by three consecutive steps: The macroscopic description of this effect will first be summarized in order to specify the important parameters governing the magnitude and behaviour of this effect; then a simple microscopic treatment is given where the basic electronic transitions are described in detail. We note, that treatments, equivalent to the level of our simple microscopic theory, have been developed concurrently with our work by other investigators {38}, {39}, {40} whose derived expressions depend on often conflicting assumptions such as equal light and heavy hole momentum scattering times {38}, or vastly different scattering times {39}, as well as restricting the photon energy to an exact equality with the energy separation of the valence bands {40}. Our analysis, however, is general with respect to radiation wavelength, carrier scattering time, and band energy separation. Finally, a rigorous mathematical derivation of the photon drag current, applicable to tellurium, is presented for the first time based on the solution of Boltzmann's transport equations, where the exact formulation of the absorption and carrier

momentum scattering processes are taken into account.

The three successive stages of increasingly detailed analysis of this effect constitute a self consistent development of the theory of the photon drag effect in tellurium.

VII 3.0 A Macroscopic Approach

The photon drag voltage, which is induced in a semiconductor due to the transfer of photon momentum to the electrons and holes, has been derived by Moss {4} from a macroscopic point of view without considering the exact details of the interaction process between the photons and free charged carriers. This analysis takes into account the effects of diffusion and the generation and recombination of carriers. For laser pulses shorter than the carrier recombination time (a few microseconds), the carrier generation and recombination effects are shown to be negligible and the resulting expression for the photon drag voltage, generated in a sample length L, is

$$V = \frac{(1 - R)\, W_0\, (P - aN)}{ec\ (P + aN).(P + N)} \left\{ \frac{1 - \exp - KL}{1 + R\ \exp -KL} \right\} \qquad (33)$$

where W_0 is the incident power density

P,N are the hole and electron concentrations, respectively.

a is the ratio of the radiation absorption coefficients for electrons and holes respectively.

K is the total absorption coefficient.

R is the reflection coefficient at the material surface.

e is the electronic charge.

c is the speed of light.

Relation (33) can be interpreted as follows:

(a) The term (P - aN) shows that electrons and holes produce signals of opposite polarity; this fact is easily seen from physical considerations since the transfer of photon momentum tends to push both types of carriers in the same direction which results in oppositely flowing induced currents. This result naturally leads to the conclusion that to increase the induced signal only one type of carrier should be dominant in the absorption process; this may be accomplished by either using doped semiconductors possessing a larger concentration of one type of carrier, or by utilizing materials where the absorption cross-sections are vastly different for the two types of carriers, i.e. $a \gg 1$ or $a \ll 1$.

(b) The magnitude of the induced voltage is inversely proportional to the total number of carriers. Therefore, it appears that low carrier concentrations are desirable for greatest voltage responsivity.

(c) The exponential terms in Equation (33) imply that a maximum voltage signal is obtained when total absorption is achieved, i.e. when $KL \geq 2$, so that the exponential terms become negligible.

(d) It is known, however, that the absorption coefficient K is directly proportional to the concentration of carriers {8}, {33}. Thus, if one lowers the carrier concentration to maximize the induced voltage according to paragraph (b), then K is correspondingly reduced and L must be made proportionally larger to satisfy the conditions of total absorption of the previous paragraph. It follows then, that if L is limited by practical considerations, materials with large absorption cross-sections β would in general, be more attractive as photon drag detectors.

In the case of tellurium, the magnitude for the photon drag signal is obtained by using the appropriate values for the parameters in Equation (33). For undoped intrinsic tellurium crystals at room temperature, in which $N = P = 4.8 \times 10^{15}$ cm^{-3}, and for CO_2 laser radiation polarized parallel to the c-axis $R = 0.53$, $K = 4$ cm^{-1}, and $a << 1$ {see Figures 4 and 5}, then an incident laser beam with a peak power density of 1 KW cm^{-2} is expected to generate in a tellurium sample of length greater than 0.5 cm, a peak voltage of 10^{-5} V; it is thus implied that for a sample with a 1 mm^2 cross-sectional area, the responsivity of this detector would be 1 mV/KW.

VII 4.0 A Simple Microscopic Analysis

VII 4.1 Introduction

In this analysis the photon drag signal is derived by considering the possible direct electronic transitions in k-space that occur when photons with energy $\hbar\omega$ and with momentum $\hbar\vec{q}$ are absorbed by holes in the valence bands of a semiconductor. The allowed direct optical transitions of holes between two hole bands, V_h and V_ℓ, are those which satisfy the condition of simultaneous conservation of energy and momentum, i.e.

$$E_h + \hbar\omega = E_\ell \tag{34}$$

and

$$\vec{k}^h + \vec{q} = \vec{k}^\ell \tag{35}$$

where E_h, E_ℓ in tellurium are associated with bands H_4 and H_5 respectively. The energy dispersion relations in the case of tellurium as given by Equation (4) do not lead readily to manageable solutions of Equations (34) and (35). A good approximation to the band structure is obtained by considering only the terms up to k^2, i.e.

$$E_{\substack{h \\ \ell}} = A(k_x^2 + k_y^2) + Dk_z^2 \pm \sqrt{S^2k_z^2 + (\Delta E/2)^2} - (\Delta\mathcal{E} + \Delta E/2) \tag{36}$$

As stated in Section III 6.2.2, direct transitions between the valence bands in tellurium, H_4 and H_5, are allowed only for radiation polarized parallel to the z or c-axis. Thus, the corresponding radiation propagation direction, characterized by $\vec{q}$, is confined to a plane perpendicular to the z-axis,

i.e. typically say $\vec{q} = q_y$. It follows that the solution of Equations (34) and (35) using Equation (36) yields that hole transitions take place for any k_x^h, k_z^h, and for the values of k_y^h given by

$$k_y^h = \frac{\sqrt{\Delta E^2 + 4S^2 k_z^2} - \hbar\omega}{2A\, q_y} - \frac{q_y}{2} \qquad (37)$$

Thus, it is important to see that the allowed transitions are scattered throughout all of k-space. It should be noted, however, that since the energy dispersion curve is anisotropic in k-space, the effective mass is also anisotropic and consequently, the hole mass associated with each possible transition depends entirely on the particular set of k_x, k_y, k_z chosen.

In order to eliminate the co-ordinate dependence of such parameters as the hole effective mass, so as to render the subsequent calculations for the photon drag signal analytically possible, both energy bands are assumed to be parabolic and isotropic characterized respectively by effective masses m_h and m_ℓ which are given by the commonly used average of the longitudinal (parallel to the c-axis) and transverse effective masses, $m_\parallel$ and $m_\perp$, i.e.

$$(m_{h,\ell})^{-1} = \frac{1}{3}\left(\frac{1}{m_\parallel} + \frac{2}{m_\perp}\right) \qquad (38)$$

It is emphasized that the present approach of assigning

to all transitions, an effective mass which corresponds to the average of the anisotropic effective mass over all directions, is justified by recognizing that the overall photon drag effect results from the total sum of transitions which individually are affected by effective masses corresponding to the entire range of values of the latter derivable from the combination of Equations (36) and (37).

VII 4.2 Evaluation of the Photon Drag Current

The conservation laws for both energy and momentum for parabolic and isotropic valence bands result in Equations (39)

$$\frac{\hbar^2 k_h^2}{2m_h} + \hbar\omega = \Delta E + \frac{\hbar^2 k_\ell^2}{2m_\ell} \qquad (39a)$$

$$\hbar k_h + \hbar q = \hbar k_\ell \qquad (39b)$$

where ΔE is the energy separation between the valence sub-bands at $k = 0$; ΔE can vary from zero in materials such as germanium to a finite value which is the case of tellurium.

Figure 22 shows the general schematic structure of a valence band consisting of two sub-bands in a plane passing through a local maximum which is chosen as the shifted origin $k = 0$; in this figure, the allowed direct optical transitions of holes between the heavy and light hole bands, V_h and V_ℓ respectively, which satisfy the conditions of the conservation

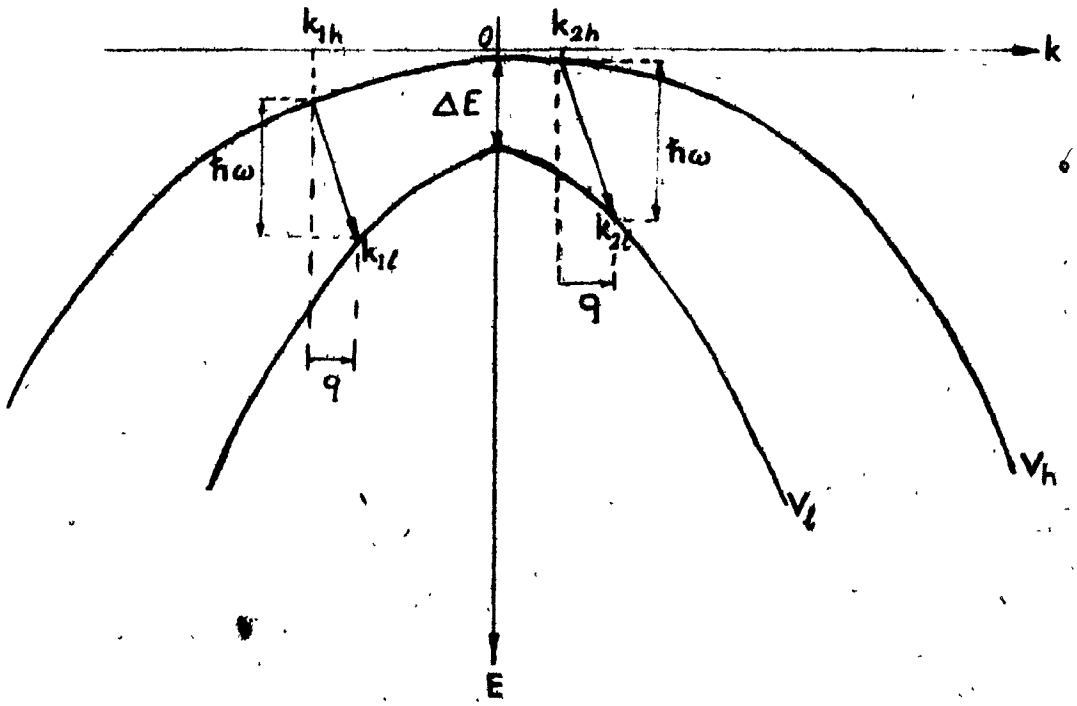

Figure 22. The Transitions of Holes Interacting with Photons of Energy $\hbar\omega$ and of Wave Vector q.

laws, are indicated by the corresponding arrows.

Equations (39a) and (39b) are found to be satisfied by only two sets of holes originating in band V_h with momentum k-vectors,

$$k_{1h} = \frac{-q}{1-z} - \left[\frac{2m_\ell(\hbar\omega - \Delta E)}{\hbar^2(1-z)} + \frac{q^2}{(1-z)^2} \right]^{1/2} \tag{40a}$$

and

$$k_{2h} = \frac{-q}{1-z} + \left[\frac{2m_\ell(\hbar\omega - \Delta E)}{\hbar^2(1-z)} + \frac{q^2}{(1-z)^2} \right]^{1/2} \tag{40b}$$

which upon transfer into band V_ℓ have the corresponding momentum vectors,

$$k_{1\ell} = \frac{-z}{1-z} q - \left[\frac{2m_\ell(\hbar\omega - \Delta E)}{\hbar^2(1-z)} + \frac{q^2}{(1-z)^2} \right]^{1/2} \tag{41a}$$

$$k_{2\ell} = \frac{-z}{1-z} q + \left[\frac{2m_\ell(\hbar\omega - \Delta E)}{\hbar^2(1-z)} + \frac{q^2}{(1-z)^2} \right]^{1/2} \tag{41b}$$

where $z \equiv m_\ell/m_h$.

If $\hbar\omega >> \Delta E$, the second term in the brackets can be neglected compared to the first, and Equations (40) and (41) can be approximated by

$$k_{1h} = - k_o - q/1-z \tag{42a}$$

$$k_{2h} = k_o - q/1-z \tag{42b}$$

and $$k_{1\ell} = - k_o - zq/1-z \tag{43a}$$

$$k_{2\ell} = k_o - zq/1-z \tag{43b}$$

where $k_o \equiv \left[\frac{2m_\ell(\hbar\omega - \Delta E)}{\hbar^2(1-z)} \right]^{1/2}$ (44)

The special case where $\hbar\omega \leq \Delta E$ will be dealt with later in Section VII 4.3.

As a result of these two transitions which occur at different k-values, the net momentum distribution of the holes in each of the bands is no longer symmetrical about $k = 0$. This unbalance of momenta in the heavy and light holes are respectively given by

$$\Delta k_h = k_{2h} + k_{1h} = - 2q/1-z \quad (45a)$$

$$\Delta k_\ell = k_{2\ell} + k_{1\ell} = - 2zq/1-z \quad (45b)$$

It is this asymmetry in momentum between the "left" and "right" holes, with respect to $k = 0$, that, as will be shown later, produces the measured signal.

The group velocity of each carrier with a perturbed momentum in bands V_h and V_ℓ is defined as

$$v_h = \frac{\hbar \Delta k_h}{2 m_h} = \frac{- \hbar q}{m_h - m_\ell} \quad (46a)$$

$$v_\ell = \frac{\hbar \Delta k_\ell}{2 m_\ell} = \frac{- \hbar q}{m_h - m_\ell} \quad (46b)$$

The factor 1/2 arises from the fact that we considered two holes simultaneously to obtain the momenta unbalance Δk in Equations 45.

Now the generation rate equations for the holes with perturbed momentum are as follows:

$$\frac{d(\Delta p_h)}{dt} = -K\left(\frac{W}{\hbar\omega}\right) - \frac{\Delta p_h}{\tau_h} \tag{47a}$$

$$\frac{d(\Delta p_\ell)}{dt} = K\left(\frac{W}{\hbar\omega}\right) - \frac{\Delta p_\ell}{\tau_\ell} \tag{47b}$$

where W is the laser power density within the material, and Δp_h, Δp_ℓ are the concentrations of holes with momentum different from that at thermal equilibrium in the heavy and light hole valence bands respectively. It is important to note that τ_h and τ_ℓ are the times necessary to achieve momentum equilibrium in the two systems of holes and not the energy relaxation time for recombination transitions between the two bands. A detailed discussion of the effective values of τ_h and τ_ℓ is given in Section VII 7.3.

The solution of Equation (47) under steady state condition is

$$\Delta p_h = -KW\tau_h/\hbar\omega \tag{48a}$$

$$\Delta p_\ell = KW\tau_\ell/\hbar\omega \tag{48b}$$

It follows that the directional flux of holes or equivalently the total photon drag current J, consisting of current contributions from both heavy and light holes in the sample under short circuit conditions, is obtained as

$$J = J_h + J_\ell = e\Delta p_h v_h + e\Delta p_\ell v_\ell \tag{49}$$

Using Equations (45) and (48)

$$J = \frac{eKW\hbar q}{\hbar\omega} \frac{\tau_h - \tau_\ell}{m_h - m_\ell} \tag{50a}$$

or $$J = \frac{eKW}{c} \frac{\tau_h - \tau_\ell}{m_h - m_\ell} \tag{50b}$$

where τ_h, τ_ℓ are respectively evaluated at an energy

$$E_h(k_o) = \frac{\hbar^2 k_o^2}{2m_h} \tag{51a}$$

and $$E_\ell(k_o) = \frac{\hbar^2 k_o^2}{2m_\ell} + \Delta E \tag{51b}$$

where k_o is given by Equation (44).

Thus it is seen that the net induced current is the sum of two oppositely flowing currents with the heavy hole current being in the direction of light propagation. Since the light holes are at a higher energy, therefore, usually it is expected that $\tau_h > \tau_\ell$ and consequently the photon drag current is dominated by the heavy holes and is in the direction of light propagation.

The induced electric field $\mathcal{E}$ in the sample under open circuit conditions is

$$\mathcal{E} = -\rho J = -\rho \frac{eKW}{c} \frac{\tau_h - \tau_\ell}{m_h - m_\ell} \tag{52}$$

where the resistivity

$$\rho = Pe^2\tau^*/m^* \tag{53}$$

and τ^* and m^* are the momentum scattering time and effective mass of the holes used in determining the resistivity of the material. Thus Equation (52) becomes

$$\mathcal{E} = - \frac{KW}{ecP} \left[\frac{m^*}{m_h(1-z)} \times \frac{\tau_h(1 - \tau_\ell/\tau_h)}{\tau^*} \right] \tag{54}$$

Due to the Fermi distribution function, the resistivity is mainly governed by the larger number of heavy holes with energies within k_BT of the band extremum. Therefore, $\tau^* \simeq \tau_h$, $m^* \simeq m_h$, and thus the above equation can be written as

$$\mathcal{E} = - \frac{KW}{ecP} \left[\frac{1 - \tau_\ell/\tau_h}{1-z} \right] \tag{55}$$

It follows that the factor in the brackets is in the order of unity if $\tau_h > \tau_\ell$ and $z < 1$ and the expression of relation (55) reduces to

$$\mathcal{E} = - \frac{KW}{ecP} \tag{56}$$

At any point x within the sample

$$W = (1-R)W_0 \exp - Kx \tag{57}$$

$$\therefore \quad \mathcal{E}(x) = - \frac{(1-R)W_0K \exp - Kx}{ecP} \tag{58}$$

and thus the open circuit voltage across the sample is given by

$$V = - \int_0^L \mathcal{E}(x)\, dx \qquad (59a)$$

$$\therefore V = \frac{(1-R)W_0}{ecP} \left\{ \frac{1 - \exp - KL}{1 + R \exp -KL} \right\} \qquad (59b)$$

where multiple reflections at the ends of the sample have also been taken into account. It is noted that the above expression is identical to that of the induced voltage in the simple formulation of the problem in Section VII 3.0 in the case when holes are considered to be the dominant carriers. The correspondence of the two expressions is only accidental due to the assumed relative values of the parameters involved in the microscopic treatment.

VII 4.3 The Special Case where $\hbar\omega \leq \Delta E$

In the microscopic derivation for the photon drag current due to direct interband transitions, it has been assumed that the photon energy is greater than the valence band energy separation in which case the possible transitions are shown to occur at two values in k-space about k = 0 whose values are approximated by Equations (42) to (44) which are in the form

$$k = \pm k_o + \delta k$$

where k_o is considered to be greater than δk. But when

$\hbar\omega = \Delta E$, $k_o = 0$ from Equation (44), and thus in order to determine the k-values at which the transitions occur, the exact Equations (40) and (41) must be used. With $\hbar\omega = \Delta E$, the latter equations yield that

$$k_{1h} = - 2q/1-z \tag{60a}$$

$$k_{2h} = 0 \tag{60b}$$

$$k_{1\ell} = - \frac{1+z}{1-z} q \tag{61a}$$

$$k_{2\ell} = q \tag{61b}$$

However, the unbalance of the momenta in the heavy and light hole bands which actually produce the photon drag current are respectively given by

$$\Delta k_h = k_{2h} + k_{1h} = - 2q/1-z$$

and $$\Delta k_\ell = k_{2\ell} + k_{1\ell} = - 2zq/1-z$$

which are still identical to Equations (45a,b) which were derived for the case when $\hbar\omega > \Delta E$. The photon drag current expression thus, remains unaltered even for $\hbar\omega = \Delta E$. Finally, due to the band broadening effects discussed in Section III 6.2.3 the case where $\hbar\omega < \Delta E$ can be assumed to be identical to that of $\hbar\omega = \Delta E$.

VII 5.0 Exact Formulation

VII 5.1 Introduction

In the above analysis it has been assumed that the rate of radiation induced transitions of both the "left" and "right" holes are equal. In actuality, as seen from Equation (40), the transitions of the holes on the left side of $k = 0$, occur at slightly higher k-values, and thus energies, than their counterparts on the right side. This fact causes a difference in the concentrations of the "working" holes on the left and right. The difference in the concentration arises from the following considerations:

a) Since the transitions on the left side occur at a higher energy, the density of available states for such holes is higher than on the right side.

b) On the other hand, the probability of a hole actually occupying the corresponding state is lower than on the right.

c) The momentum scattering times are a function of energy, and thus, are different for the two sets of "working" holes.

d) For crystals such as germanium, where the transition matrix M between the two valence bands is a function of the quasi-momentum k, e.g. $|M|^2 = k^2 |A|^2$ {41}, the transition matrix element for the left holes is higher than for those on the right side.

Since we were dealing with small asymmetries in the first place, these above mentioned additional perturbations, which affect the final concentrations of nonequilibrium holes, can play an important role in forecasting the exact behaviour of the photon drag signal especially as the temperature is varied. In this section a rigorous treatment will be presented where the generated current density is obtained by solving Boltzmann's transport equation where the explicit forms of the transition probabilities and hole scattering mechanisms are incorporated.

VII 5.2 Solution of Boltzman's Equation

In terms of f(k), the solution of Boltzman's transport equation, the current density is given as {32}

$$J_i = \frac{e}{4\pi^3} \sum_{\alpha} \int \hat{f}^{\alpha}(k)\, v_i^{\alpha}\, d\vec{k} \qquad (62)$$

where $\hat{f}(k) = f - f_o$ is the non-equilibrium part of the distribution function for holes, and

$$v_i^{\alpha} = \frac{1}{\hbar} \frac{\partial E_k^{\alpha}}{\partial k_i} \qquad (63)$$

is the group velocity of holes with an energy E_k^{α}.
$\alpha = h$ for heavy holes and $\alpha = \ell$ for light holes.

Now in the steady state, the rate of change of f due to generation by photon excitation $\left(\frac{\partial f}{\partial t}\right)_{phot}$ is set equal to $\hat{f}/\tau(E_k)$ in the standard relaxation time approximation

where $\tau(E_k)$ is the total scattering time of holes including collisions with acoustic and optical phonons, if we restrict ourselves to a linear approximation with respect to the intensity of light. Therefore,

$$\left(\frac{\partial f^{\alpha}}{\partial t}\right)_{phot} = \hat{f}^{\alpha}(k)/\tau^{\alpha}(E_k) \tag{64}$$

and thus using Equations (63) and (64), Equation (62) becomes

$$J_i = \frac{e}{4\pi^3\hbar}\sum_{\alpha}\int\left(\frac{\partial f^{\alpha}}{\partial t}\right)_{phot}\tau^{\alpha}(E_k)\,\frac{\partial E_k^{\alpha}}{\partial k_i}\,d\vec{k} \tag{65}$$

It is now assumed that the rate of change with time of the distribution functions f^{α} due to the absorption of photons with frequency ω, unit polarization vector $\vec{e}$, and wave vector $\vec{q}$, have the following form {42}:

$$\left(\frac{\partial f^{h}}{\partial t}\right)_{phot} = -|M|^2\left[f^{h}(E^{h}_{\vec{k}}) - f^{\ell}(E^{h}_{\vec{k}}+\hbar\omega)\right]\delta(E^{h}_{\vec{k}}+\hbar\omega - E^{\ell}_{\vec{k}+\vec{q}}) \tag{66a}$$

$$\left(\frac{\partial f^{\ell}}{\partial t}\right)_{phot} = |M|^2\left[f^{h}(E^{\ell}_{\vec{k}}-\hbar\omega) - f^{\ell}(E^{\ell}_{\vec{k}})\right]\delta(E^{h}_{\vec{k}-\vec{q}}+\hbar\omega - E^{\ell}_{\vec{k}}) \tag{66b}$$

where in general the transition probability matrix element {41}

$$|M| = |\vec{e}\cdot\vec{H}| + (\vec{e}\cdot\vec{k})\,A + \ldots \tag{67}$$

and H, A are proportional to the intensity of light and the magnitude of the interband dipole moment.

The calculation of the photon drag current will now

be continued for crystals like Te in which $|H| > 0$ {43} due to the finite separation ΔE between the valence bands; in this case the second term in Equation (67) can normally be neglected compared to the first. For materials such as Ge where $\Delta E = 0$, i.e., where the valence bands are degenerate at $k = 0$, $|H| = 0$ and the second term is dominant in the absorption process. This case has been dealt with by other authors {42}, {44} and their results will be presented at the end of this section for the sake of comparison.

Substituting Equations (66) into Equation (65), we get

$$J_i = -\frac{e}{4\pi^3\hbar}\int \tau^h(E_{\vec{k}}^h)\frac{\partial E_k^h}{\partial k_i}\left|\vec{e}\cdot\vec{H}\right|^2\left[f^h(E_{\vec{k}}^h) - f^\ell(E_{\vec{k}}^h + \hbar\omega)\right]\delta(E_{\vec{k}}^h + \hbar\omega - E_{\vec{k}+\vec{q}}^\ell)d\vec{k}$$

$$+\frac{e}{4\pi^3\hbar}\int \tau^\ell(E_{\vec{k}}^\ell)\frac{\partial E_k^\ell}{\partial k_i}\left|\vec{e}\cdot\vec{H}\right|^2\left[f^h(E_{\vec{k}}^\ell - \hbar\omega) - f^\ell(E_{\vec{k}}^\ell)\right]\delta(E_{\vec{k}-\vec{q}}^h + \hbar\omega - E_{\vec{k}}^\ell)d\vec{k} \quad \ldots (68)$$

In order to evaluate the above integrals, it is first necessary to find the values of k which will set the arguments of the delta functions equal to zero, i.e.

$$E_{\vec{k}}^h + \hbar\omega - E_{\vec{k}+\vec{q}}^\ell = 0 \qquad (69a)$$

and

$$E_{\vec{k}-\vec{q}}^h + \hbar\omega - E_{\vec{k}}^\ell = 0. \qquad (69b)$$

For parabolic and isotropic valence bands in which it is once again assumed that the energy dispersion relations are in the form

$$E_k^\alpha = \frac{\hbar^2 k_\alpha^2}{2m_\alpha} \tag{70}$$

Equations (69) become

$$\frac{\hbar^2 k_h^2}{2m_h} + \hbar\omega - \Delta E - \frac{\hbar^2(k_h^2 + 2(\vec{k}_h \cdot \vec{q}) + q^2)}{2m_\ell} = 0 \tag{71a}$$

and

$$\frac{\hbar^2(k_\ell^2 - 2(\vec{k} \cdot \vec{q}) + q^2)}{2m_h} + \hbar\omega - \Delta E - \frac{\hbar^2 k_\ell^2}{2m_\ell} = 0 \tag{71b}$$

For the case when $\hbar\omega > \Delta E$, the roots of the two equations up to terms linear in the photon wave vector q can be shown to be respectively

$$k_h = \pm k_o + \delta k_h \quad \text{and} \quad k_\ell = \pm k_o + \delta k_\ell \tag{72}$$

where

$$k_o \equiv \left[\frac{2m_\ell(\hbar\omega - \Delta E)}{\hbar^2(1-z)}\right]^{1/2} \tag{73}$$

$$\delta k_h = -\frac{\vec{a}\cdot\vec{q}}{1-z} \quad ; \quad \delta k_\ell = -\frac{z}{1-z}\,\vec{a}\cdot\vec{q} \tag{74}$$

and

$$\vec{a} = \frac{\vec{k}}{|k|} \tag{75}$$

For small perturbations the distribution functions $f^\alpha(E_{\vec{k}})$ in Equation (68) are considered to have the form of the equilibrium functions $f_o(E_{\vec{k}})$.

Next a Taylor series expansion of all functions under the integral sign is performed around the wave vector k_o up to terms linear in δk. The results of these expansions are

listed below: (See Appendix I for detailed derivations)

$$\tau_\alpha(E_k) = \tau_\alpha(E_{k_o}) + \frac{\partial \tau_\alpha}{\partial k_o}\ \delta k_\alpha \tag{76}$$

$$\frac{\partial E_k^\alpha}{\partial k_i} = \frac{\hbar^2 a_i}{m_\alpha}\ [\ k_o + \delta k_\alpha\ ] \tag{77}$$

$$\left[\ f_o(E^h_{\vec{k}}) - f_o(E^h_{\vec{k}} + \hbar\omega)\ \right] = \left[\ f_o(E^h_{k_o}) - f_o(E^h_{k_o} + \hbar\omega)\ \right]\left[\ 1+\delta k_h(-\frac{2\varepsilon_h}{k_B T k_o})\right] \tag{78}$$

$$\delta(E^h_{\vec{k}} + \hbar\omega - E^\ell_{\vec{k}+\vec{q}}) = \delta(k_h - k_o - \delta k_h) \Big/ \frac{\hbar^2 k_o(1-z)}{m_\ell} \tag{79}$$

$$\delta(E^h_{\vec{k}-\vec{q}} + \hbar\omega - E^\ell_{\vec{k}}) = \delta(k_\ell - k_o - \delta k_\ell) \Big/ \frac{\hbar^2 k_o(1-z)}{m_\ell} \tag{80}$$

$$\left[\ f_o(E^\ell_{\vec{k}} - \hbar\omega) - f_o(E^\ell_{\vec{k}})\ \right] = \left[\ f_o(E^\ell_{k_o} - \hbar\omega) - f_o(E^\ell_{k_o})\right]\left[\ 1 + \delta k_\ell(-\frac{2\varepsilon_\ell}{k_B T k_o})\right] \tag{81}$$

After substituting Equations (72) to (75) into Equations (76) to (81), then these results into Equation (68), and subsequently retaining only the terms linear in q, we get

$$J_i = J_h + J_\ell \tag{82}$$

where

$$J_h = \frac{e}{4\pi^3}\ \frac{z}{(1-z)^2}\ \frac{k_o}{\hbar}\left[\ f_o(E^h) - f_o(E^h + \hbar\omega)\ \right][\vec{e}\cdot\vec{H}]^2 \left\{ 3\tau_h - \frac{2\tau_h \varepsilon_h}{k_B T} + k_o \frac{\partial \tau_h}{\partial k_o} \right\} q_j \int a_i a_j d\Omega_k \tag{83}$$

$$J_\ell = -\frac{e}{4\pi^3}\,\frac{z}{(1-z)^2}\,\frac{k_o}{\hbar}\,\left[\, f_o(E^\ell - \hbar\omega) - f_o(E^\ell)\,\right]\,\left[\vec{e}\cdot\vec{H}\right]^2\left\{3\tau_\ell - \frac{2\tau_\ell\varepsilon_\ell}{k_B T} + \frac{k_o\,\partial\tau_\ell}{\partial k_o}\right\} q_j \int a_i a_j d\Omega_k \qquad (84)$$

All quantities are evaluated at $k = k_o$; Ω_k is the solid angle in k-space introduced by the change into spherical coordinates. It is noted that

$$E^h_{k_o} + \hbar\omega = E^\ell_{k_o} \qquad (85)$$

Thus

$$J_i = \frac{e}{4\pi^3}\,\frac{z}{(1-z)^2}\,\frac{k_o}{\hbar}\,\left[\, f_o(E^h) - f_o(E^\ell)\,\right]\,\left[\vec{e}\cdot\vec{H}\right]^2\left\{\tau_h\left(3-\frac{2\varepsilon_h}{k_B T}\right) - \tau_\ell\left(3-\frac{2\varepsilon_\ell}{k_B T}\right) + k_o\,\frac{\partial(\tau_h-\tau_\ell)}{\partial k_o}\right\} q_j \int a_i a_j d\Omega_k \qquad (86)$$

Equation (86) is put into a form easier to interpret and use by noting that the radiation absorption coefficient K is defined as [43],

$$K = \frac{1}{4\pi^3}\left(\frac{\hbar\omega}{W e_m e_n}\right)\int\left[\, f_o(E^h) - f_o(E^\ell)\,\right]\left[\vec{e}\cdot\vec{H}\right]^2\,\delta(E^\ell - E^h - \hbar\omega)\,d^3k \qquad (87)$$

where $$\left[\vec{e}\cdot\vec{H}\right]^2 = e_m H_m e_n H_n \equiv \phi^2_{mn} e_m e_n\,, \qquad (88)$$

therefore $$K = \frac{4\pi}{4\pi^3}\left(\frac{\hbar\omega}{W}\right)\phi^2_{mn}\left[\, f_o(E^h) - f_o(E^\ell)\,\right]\frac{k_o}{\hbar^2}\,\frac{m_\ell}{1-z} \qquad (89)$$

Thus substituting Equation (89) into Equation (86), the expression for the photon drag current density becomes,

$$J_i = \left\{ y \frac{eKW}{c(m_h - m_\ell)} \left[\tau_h \left(3 - \frac{2\varepsilon_h}{k_B T}\right) - \tau_\ell \left(3 - \frac{2\varepsilon_\ell}{k_B T}\right) + k_o \frac{\partial(\tau_h - \tau_\ell)}{\partial k_o} \right] \right\} \hat{q}_j e_m e_n \quad (90)$$

where $y = \frac{1}{4\pi} \int a_i a_j d\Omega_k$, a factor less than unity since any $a_i \leq 1$.

Since K is a function of the polarization directions m and n through the transition matrix element ϕ^2_{mn} and y is a function of the directions i and j through the directional cosines a_i, a_j, it clearly follows that the factor in the curly brackets of Equation (90) is dependent on all four directions; consequently it can be written as a tensorial coefficient — T_{ijmn}; Thus the current density is in the form

$$J_i = T_{ijmn} \hat{q}_j e_m e_n \quad (91)$$

which obviously confirms the fourth rank tensorial nature of the photon drag effect.

VII 6.0 Comparison with the Simple Microscopic Expression

When any current component of Equation (90) is written in the following form,

$$J = \frac{eKW}{c(m_h - m_\ell)} y \left[(\tau_h - \tau_\ell) + \left(2 - \frac{2\varepsilon_h}{k_B T} + k_o \frac{\partial}{\partial k_o}\right)\tau_h - \left(2 - \frac{2\varepsilon_\ell}{k_B T} + k_o \frac{\partial}{\partial k_o}\right)\tau_\ell \right] \quad (92)$$

it is generally identical to Equation (50b) in Section VI 4.2, derived utilizing the simple microscopic viewpoint, with a number of additional terms. It is to be noted that the extra

terms in Equation (92) are the result of the detailed considerations, mentioned in the introduction of Section VII 5.0, concerning the difference in the transition processes characterizing the "left" and "right" holes; thus,

a) the two $2\zeta_\alpha$ additional terms arise from the difference in the available density of states between the "left" and "right" holes.

b) the two terms $2\varepsilon_\alpha/k_BT$ arise from distribution function asymmetry for "left" and "right" holes.

c) the $k_o \frac{\partial \tau_\alpha}{\partial k_o}$ terms arise from the difference in the scattering times between the "left" and "right" holes.

d) the factor y occurs because only those holes, which have components of their initial momenta parallel to both the photon momentum $\hbar q$ and the measurement direction, contribute to the photon drag current.

The importance of these additional terms will depend on the particular material and radiation wavelength under consideration. In the following section the special case of tellurium exposed to the 10.6 μ, CO_2 laser radiation is discussed.

VII 7.0 Special Case of Tellurium

VII 7.1 Introduction

Recalling that in tellurium, direct transitions between the H_4 and H_5 {see Figure 7} valence sub-bands are allowed only for radiation polarized parallel to the 3 axis, i.e. m = n = 3, it is found that for longitudinal measurements of electric signals along the 1, 2 or 3 directions, e.g. i = j = 1,2, or 3, y = 1/3; therefore this combination of measurement and propagation directions correspond to the photon drag tensor coefficients $T_{1133} = T_{2233}$ and T_{3333}; in this case,

$$J = \frac{eKW}{3c(m_h - m_\ell)} \left\{ \left(3 - \frac{2\varepsilon_h}{k_B T} + k_o \frac{\partial}{\partial k_o}\right)\tau_h - \left(3 - \frac{2\varepsilon_\ell}{k_B T} + \frac{k_o \partial}{\partial k_o}\right)\tau_\ell \right\} \quad (93)$$

It is interesting to note that when $i \neq j$, y = 0 and consequently the photon drag signal in transverse measurements is zero. This is consistent with the fact that transverse signals are not expected when the energy bands are isotropic as has been assumed in our treatment for the theoretical derivation of the photon drag current.

In order to evaluate the relative contributions of the various terms in the curly brackets of Equation (93) to the photon drag current in tellurium, one must obtain the magnitudes of the corresponding parameters. In the following sections the magnitude and the relative importance of the latter quantities are estimated.

VII 7.2 Evaluation of $2\varepsilon_\alpha/k_BT$

The first terms to be evaluated in expression (93) are $2\varepsilon_\alpha/k_BT$ which characterize the asymmetry of the distribution function about $k = 0$. From infrared absorption data of tellurium {24}, it is known that the energy separation ΔE of the valence sub-bands is equal to 0.114 eV at room temperature, whilst the CO_2 laser photon energy $\hbar\omega = 0.117$ eV; correspondingly the photon momentum vector $q = \hbar\omega/\hbar c = 6 \times 10^5\ m^{-1}$. On the other hand for the latter values of ΔE, $\hbar\omega$, and for $m_\ell = .07\ m_o$, $m_h = .23\ m_o$, $z = .3$, Equation (73) yields $k_o = 9.3 \times 10^7\ m^{-1}$; this shows that the assumption that $k_o >> q$ is generally valid provided $\hbar\omega$ is not identically equal to ΔE. Furthermore, for the above value of k_o, since $\varepsilon_\alpha = \hbar^2k_o^2/2m_\alpha$, $\varepsilon_h = 1.5$ meV and $\varepsilon_\ell = 5$ meV which implies that, at room temperature, $2\varepsilon_\alpha/k_BT < 1$; this factor will approach zero as k_o, and therefore ε_α tend toward zero as $\Delta E \to \hbar\omega$ at lower temperatures {refer to Section III 6.2.3}; thus the terms $2\varepsilon_\alpha/k_BT$ can generally be neglected in Equation (93).

VII 7.3 The Momentum Scattering Time τ

VII 7.3.1 Introduction

As stated in Section VII 4.2, τ_α is time necessary to achieve hole momentum equilibrium in each valence sub-band. This equilibrium is achieved via scattering processes which

redistribute isotropically the directional momentum which was originally produced by the transfer of photon momentum to holes in the valence bands. The total momentum scattering time generally consists of the contributions from the common intraband type of scattering mechanisms as well as by interband scattering characterized by scattering times $\tau_{\alpha\alpha}$ and $\tau_{\ell,h}$ {see Figure 23} respectively. Thus the total momentum scattering time τ_α is commonly written as

$$\tau_\alpha^{-1} = \tau_{\alpha\alpha}^{-1} + \tau_{\ell,h}^{-1} \qquad (94)$$

VII 7.3.2 Evaluation of τ_h

In the temperature range below 300 K, the Fermi distribution function dictates that the population of holes, p_ℓ, in the valence sub-band H_5 is negligible compared to the population p_h in band H_4, indeed $p_\ell/p_h = \exp - \Delta E/k_B T < 10^{-2}$, thus the total momentum scattering time derived from available data on hole mobility μ, in tellurium is that of the upper or heavy hole valence band, i.e.

$$m^*\mu/e = \tau_h \qquad (95)$$

Before τ_h can be evaluated, the magnitude of the effective mass m^* must be known. Since the band structure in tellurium is actually non-parabolic, the effective mass is not constant over all of k-space and thus an average effective mass $m^* = 0.23\ m_o$ is used which best fits experimental

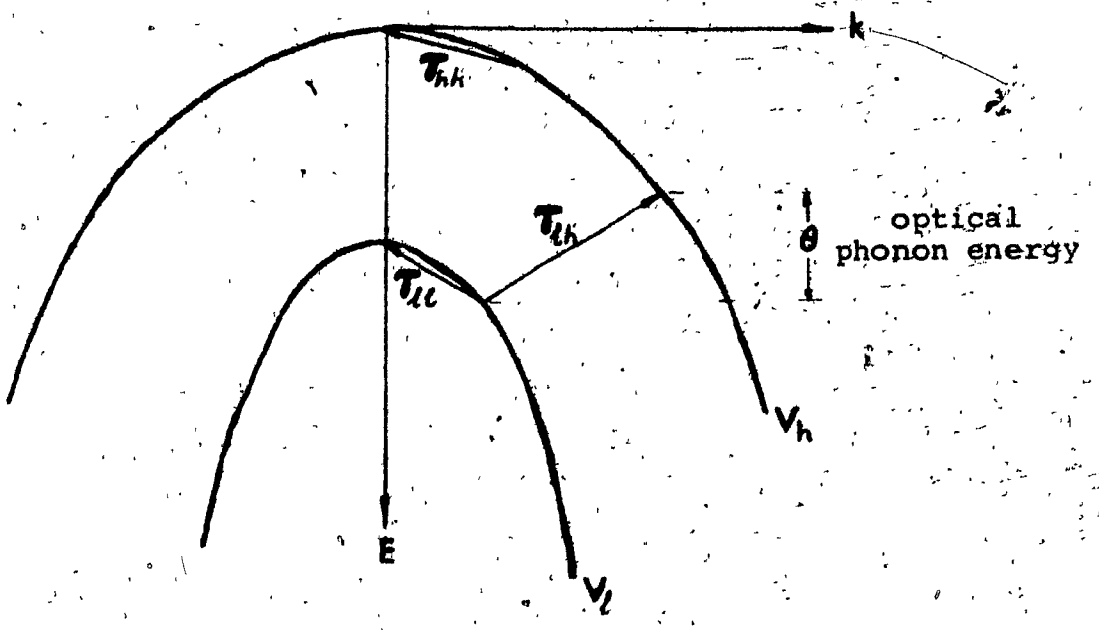

Figure 23. Scattering Mechanisms in the Valence Bands of Tellurium.

mobility data {9}. This value is in agreement with the value m_h, obtained by using Equation (38) and the values of $m_{\parallel}$ and $m_{\perp}$ which were evaluated in Section III 6.2.1 from the actual energy dispersion relations of the valence bands.

At 297 K, it is found that $\mu_h \simeq 700\ cm^2\ Vs^{-1}$ {45} which yields $\tau_h \simeq 10^{-13}s$. Since the mobility is found to have approximately a $T^{-3/2}$ temperature dependence {11}, it is estimated that at 100 K, $\tau_h \simeq 5 \times 10^{-13}s$.

VII 7.3.3 Evaluation of $k_o \frac{\partial \tau_h}{\partial k_o}$

It is considered that, at room temperature, τ_h is mainly determined by the acoustic phonon scattering mechanisms {46}, {47}. The acoustic scattering time τ_{ac} varies as the half power of the hole kinetic energy ε_h {48}. Thus

$$\tau_h = \tau_{ac} = A' \varepsilon_h^{-1/2} \qquad (96a)$$

and to the extent of parabolic energy dispersion characteristic validity,

$$\tau_h = A\ k_o^{-1} \qquad (96b)$$

It is found that the term $k_o \frac{\partial \tau_h}{\partial k_o}$ is of the order of τ_h and actually using Equation (96b)

$$k_o \frac{\partial \tau_h}{\partial k_o} = -\tau_h \qquad (97)$$

However, at temperatures below 150 K, the magnitude of τ_h in tellurium is largely governed by the polar optical scattering mechanism {9}. In this type of hole-phonon interaction, the scattering time for hole energies $\varepsilon_h \to 0$, as is our case at low temperatures {refer to Section VII 7.2}, becomes independent of the carrier energy {48}; consequently, it follows that

$$k_o \frac{\partial \tau_h}{\partial k_o} \to 0 \quad \text{for} \quad T < 150 \text{ K} \ .$$

VII 7.3.4 Evaluation of τ_ℓ, $k_o \frac{\partial \tau_\ell}{\partial k_o}$

For the holes in the light hole valence band H_5, the momentum scattering time τ_ℓ is not precisely known from any experimental data. Intuitively, it can be assumed that since the light holes are at a higher energy, their momentum scattering time τ_ℓ is shorter than the scattering time associated with the heavy holes. An estimatation for the value of τ_ℓ is now attempted by employing the following considerations.

While the scattering of the heavy holes is considered to be governed to a large part by intraband phonon scattering, it is believed that for the non-equilibrium or excess light holes, the dominant process is the $H_5 \to H_4$ interband scattering by Γ_1 polar optical phonons with an energy $\theta = 0.012$ eV {43}. The scattering time τ_{po} due to polar

optical phonons is given as {48}.

$$\tau_{po}^{-1} = \frac{2eF_o}{(2m_\alpha E_\alpha)^{1/2}} \frac{1}{\exp(x_o) - 1} \left[\sinh^{-1}\left(\frac{E_\alpha}{\theta}\right)^{1/2} + \exp(x_o) \sinh^{-1}\left(\frac{E_\alpha}{\theta} - 1\right)^{1/2} \right] \quad \ldots (98)$$

where $eF_o \equiv \frac{m_\alpha e^2 \theta}{h^2} \left(\frac{1}{\varepsilon(\infty)} - \frac{1}{\varepsilon(0)} \right)$

$x_o = \theta / k_B T$

E_α is the proper hole energy.

$\varepsilon(\infty), \varepsilon(0)$ are the high and low frequency dielectric constants respectively.

m_α is the appropriate effective mass.

The evaluation of Equation (98) for the case of light holes in tellurium, in which

$E_\ell \simeq \hbar\omega = .117$ eV (10.6 μ radiation)

$\varepsilon(\infty) = 36$, $\varepsilon(0) = 54$

$m_\ell = .07\ m_o$ (from Equation (38) and Section III 6.2.1),

gives a value of $\tau_\ell \simeq \tau_{po} \simeq 10^{-14}$s at room temperature and equals 2.7×10^{-14}s at 100 K. Since the light hole energy $E_\ell \simeq \hbar\omega$ and thus is independent of k_o, this implies that τ_{po} is also independent of k_o {refer to Equation (98)}, and consequently it follows that $k_o \frac{\partial \tau_\ell}{\partial k_o} = 0$.

VII 7.4 Simplification of the Expression for the Photon Drag Signal in Tellurium

In comparing the estimated numerical values of the momentum scattering times in the two valence sub-bands of tellurium it is seen from Section VII 7.3.2 and VII 7.3.4 that τ_h is estimated to be an order of magnitude larger than τ_ℓ which implies that the terms involving τ_ℓ can be neglected in Equation (93); consequently the photon drag current, according to the present treatment, is mainly governed by the heavy holes in band H_4. Furthermore, recalling that $k_o \frac{\partial \tau_h}{\partial k_o} \simeq - \tau_h$ {Section VII 7.3.3} and $2\varepsilon_h/k_B T \to 0$ {Section VII 7.2}, the exact expression for the photon drag effect given by Equation (93) reduces simply to

$$J = \frac{2}{3(1-z)} \frac{e\tau_h}{cm_h} KW = \frac{2}{3} \frac{\mu_h K}{(1-z)c} W \qquad (99)$$

where μ_h is the observable hole mobility. This expression gives the expected longitudinal photon drag current density in tellurium with $E \parallel c$ as a function of the radiation power density within the sample.

VII 7.5 Comparison with the Macroscopic Result

It is now possible to compare expression (99), obtained from detailed considerations of the microscopic processes involved in the photon drag effect with expression (33) which is obtained from a simple consideration of radiation

momentum exchange with the charge carriers in the given material.

From the values of the effective masses evaluated in Section III 6.2.1 and with the application of Equation (38), we get that $m_h = .23\ m_o$, $m_\ell = .07\ m_o$ and $z \equiv m_\ell/m_h = .3$. Consequently, Equation (99) becomes

$$J = \frac{\mu_h KW}{c} \tag{100}$$

Under open circuit conditions and neglecting diffusion effects, a local electric field

$$\mathcal{E} = -\rho J \tag{101}$$

must exist within the sample to inhibit the current flow. Now

$$\rho^{-1} = e\,\mu_h(P + bN) \tag{102}$$

where b is the ratio of electron to hole mobilities and thus

$$\mathcal{E} = -\frac{KW}{ec(P+bN)} \tag{103}$$

Now, the power density W at each point x within the sample is given by

$$W = W_0(1-R)\exp - Kx \tag{104}$$

where W_0 is the incident power density and R is the reflection coefficient at the air - Te interface. Therefore,

$$\mathcal{E}(x) = \frac{(1-R)\ W_0 K \exp - Kx}{ec(P+bN)} \qquad (105)$$

and consequently the measured voltage across a sample of length L is

$$V = - \int_0^L \mathcal{E}(x)\ dx \qquad (106)$$

$$\therefore \quad V = \frac{(1-R)W_0}{ec(P+bN)} \quad \frac{1 - \exp - KL}{1+R \exp - KL} \qquad (107)$$

where multireflection at the two ends of the sample have been taken into account.

It must be noted that, only as a result of the specific numerical values assigned to the various parameters such as m_h, m_ℓ, τ_h, and τ_ℓ in tellurium, the results of our exact microscopic treatment for the determination of the photon drag voltage in tellurium are essentially identical to the macroscopically derived expression, Equation (33) for the case when holes are considered to be the dominant free carrier in the absorption process, i.e. $a << 1$; this is the case in tellurium when the radiation is polarized parallel to the c-axis and only holes are involved in direct transitions between energy bands. A factor b appears in Equation (107) and not in Equation (33) because in the present derivation of the induced voltage from the photon drag current, the effects of carrier diffusion have been neglected. When this macroscopic effect is considered according to the treatment of Moss {4}, the factor b no longer appears in the final

expression for the induced photon drag voltage.

VII 8.0 Comparison with the Photon Drag Signal in Germanium

For the calculation of the photon drag current in Ge, the same procedure is used as in Section VII 5.2 for Te but in this case since $\Delta E = 0$, $|M|^2 = (\vec{e}\cdot\vec{k})^2 A^2$. The final result is {42} that in germanium

$$J_i = \frac{y^* eKW}{c(m_h - m_\ell)} \left\{ \tau_h\left(5 - \frac{2\varepsilon_h}{k_B T}\right) - \tau_\ell\left(5 - \frac{2\varepsilon_\ell}{k_B T}\right) + k_o \frac{\partial}{\partial k_o}(\tau_h - \tau_\ell) \right\} \hat{q}_j e_m e_n \quad (108)$$

where $y^* = \dfrac{\int a_i a_j a_m a_n \, d\Omega_k}{\int a_m a_n \, d\Omega_k}$

In the case of germanium, the k^2 dependence of the transition probability matrix $|M|^2$ yields that the above expression differs from Equation (90) by the extra terms $2\tau_\alpha$. In addition, the factor y is somewhat modified as only those holes with momentum components parallel to the polarization vector, as well as the measurement and light propagation directions contribute to the photon drag current.

In germanium, the dominant mechanism determining τ_h and τ_ℓ is non polar scattering, thus $k_o \dfrac{\partial \tau_\alpha}{\partial k_o} \simeq -\tau_\alpha$ {refer to Section VII 7.3.3} Since the energy of the light holes is greater than the energy of the heavy holes, τ_h is again substantially larger than τ_ℓ. Thus Equation (108) is reduced to the form:

$$J \simeq \frac{eKW\ \tau_h(4-2\varepsilon_h/k_BT)}{5c(m_h - m_\ell)} \qquad (109)$$

for the currents corresponding to the components T_{iijj} with $i \neq j$. A complete derivation of the photon drag effect in germanium is given in {42}, where band anisotropy is also taken into account.

The most important difference between the photon drag currents of Te and Ge is the magnitude of the factor $2\varepsilon_h/k_BT$. Recalling that {see Equations (A9) and (73)} $\varepsilon_h = (\hbar\omega - \Delta E)z/(1-z)$ and since $\Delta E = 0$ for Ge, it is seen that ε_h for Ge is much greater than ε_h for Te. In particular, in the case of CO_2 laser radiation, in Te $\hbar\omega \simeq \Delta E$ and thus $\varepsilon_h \simeq 0$, while in the case of Ge with $z = .14$ {49}, $\varepsilon_h = \hbar\omega z/(1-z) \simeq .02$ eV. Thus for Ge, $2\varepsilon_h/k_BT \simeq 1.6$ at 300 K, but more critically, at 100 K $2\varepsilon_h/k_BT \simeq 5$. Consequently, it is seen from Equation (109), that as the temperature is lowered, the photon drag current in germanium decreases and in fact eventually reverses its polarity, whereas no such behaviour is expected to occur in tellurium.

VII 9.0 The Photon Drag Signal due to Intraband Transitions

The preceding analysis derived the photon drag current for the case when direct intervalence band hole transitions are the dominant process by which the radiation is absorbed as is the case in tellurium for radiation polarized parallel

to the c-axis. In addition to direct hole transitions, all semiconductors, including tellurium for any radiation polarization, also absorb infrared radiation via free carrier intraband transitions, i.e., electrons and holes are excited by radiation photons to a higher energy within the same band (see Figure 8). In the case of tellurium, for radiation polarized parallel to the c-axis, in the radiation wavelengths of interest, the direct transitions dominate, and thus the contribution due to intraband transitions can be neglected; on the other hand, for radiation polarized perpendicular to the c-axis, the direct transitions between the H_4 and H_5 valence bands are forbidden, and consequently, the intraband type of transitions must be considered in the evaluation of the radiation induced photon drag signal.

The excitation of a free charged carrier to a higher energy level within the same band must be accompanied by a change in the k-value of the hole or electron; thus in order to acquire this additional momentum, the free charged particles must be simultaneously scattered by a phonon during the photon absorption process. Since in this type of absorption process the simultaneous interaction of three particles is necessary, namely, a photon, a free carrier, and a phonon, the absorption coefficient for intraband transitions is generally smaller in magnitude than for direct interband transitions. Indeed, it is found that in the particular case of Te at 10.6 μ, the absorption coefficient due to

intraband transitions is a factor of 30 smaller than that corresponding to intervalence band transitions {see Figures 4 and 5}.

Several authors have derived the generated photon drag signal due to intraband transitions {44}, {50}, where the details of the interaction mechanisms, including carrier scattering, by acoustic and optical phonons {51}, by polar optical phonons {52}, by charged impurities {51}, and by piezoelectric scattering {53}, have been considered. The mathematical formulae for the induced photon drag current resulting from these derivations are generally complex and depend greatly on the type of scattering mechanisms considered. These expressions can be summarized by expressing the photon drag current due to one type of charged carrier in an analogous form to Equation (99), as

$$J = \pm \frac{KeW}{cm} << \tau_{\pm} >> \qquad (110)$$

where $<< \tau_{\pm} >>$ has dimensions of an effective momentum scattering time for the charged carriers; the sign is taken to be + for holes and - for electrons consistent with the charge of the carrier. It is important to note that $<< \tau_{\pm} >>$ can itself be a positive or negative quantity. The total photon drag current in the sample is the algebraic sum of the contributions from the holes and electrons.

Following the same procedure as presented in Section VII 7.5, yields an open circuit photon drag voltage for

intraband transitions which can be written in the form

$$V = \eta \frac{(1-R)\ W_0 (P-a\gamma N)}{ec(P+aN)(P+N)} \left\{ \frac{1 - \exp - KL}{1 + R \exp - KL} \right\} \qquad (111)$$

where $\gamma = << \tau_- >> / << \tau_+ >>$, and η is proportional to $<< \tau_+ >> / \tau_h$, which can be considered as an efficiency factor determining the fraction of the photon's momentum collected by a hole in the radiation induced indirect transition. The factor η can be evaluated from experimental data; it has been found that in germanium η is less than 50% for electrons in samples with carrier concentrations below 10^{16} cm^{-3} {54}. The factor η in tellurium is expected to be evaluated from the experimental results of this work.

VII 10.0 Speed of Response of Photon Drag Detectors

The previous discussion of the photon drag effect shows that the speed of response in a practical photon drag detector will be limited by the following factors:

a) Momentum relaxation time

As the photon drag effect is a manifestation of the radiation induced disturbance of the carrier momenta, the time necessary to re-establish momentum equilibrium, i.e. the momentum relaxation or scattering time $\tau_h \approx 10^{-13}$s {Section VII 7.3.2}, is a fundamental speed limitation of this effect.

b) Dielectric relaxation time

Under open circuit conditions the photon drag effect, like any other photocurrent generating mechanism, manifests itself by setting up an electric polarization field in the volume between the contacts; this then naturally leads to an induced internal electric field and correspondingly, a measured voltage. The time necessary to redistribute the excess polarization charge associated with the dipole, called the dielectric relaxation time $= \varepsilon\rho \simeq 10^{-12}$s, is another fundamental limitation to the speed of response.

c) Light propagation time

The transit time of light through the sample, given by nL/c is clearly also a limitation for the speed of response; this time is typically $\simeq 10^{-10}$s for a detector length of 1 cm.

In summary, the fundamental response time is limited and determined by the longest of the three above mentioned characteristic times, namely the momentum relaxation time, the dielectric relaxation time, and the transit time. However, in normal practical measurements, the RC time constants of the external electric circuitry are usually even longer and, therefore, constitute the limit to the overall detection system's response time.

VII 11.0 Conclusion

A theoretical treatment of the photon drag effect has been presented in this chapter in three stages: First a macroscopic description was given to introduce such important parameters as the free carrier concentrations and the absorption coefficient which are shown to govern primarily the magnitude of the photon drag effect; next, a simple microscopic treatment shows the actual physical process by which the photon momentum produces a momentum unbalance in the hole ensemble, thus resulting in the photon drag current; finally, a rigorous mathematical derivation is presented where the exact formulation of the absorption and momentum scattering processes are taken into account.

It is shown that in the special case of CO_2 laser radiation in tellurium, the expression obtained from the rigorous microscopic theoretical treatment predicts signal magnitudes similar to those obtained from the simple macroscopic treatment, only as a result of the numerical values of the different parameters involved. The longitudinal photon drag signal in undoped samples at room temperature is expected to be 10 mV for an incident power density of $1 MW\ cm^{-2}$.

The fundamental speed of response of the photon drag effect is shown to be limited by the longest of either of the momentum scattering, dielectric relaxation, and light transit times within the sample.

CHAPTER VIII

INTERPRETATION OF THE PHOTON DRAG RESULTS

VIII 1.0 Introduction

The experimental results for the photon drag effect in tellurium, under various combinations of directions of, potential measurement, radiation propagation and polarization, were given in Chapter VI, whereas Chapter VII presented the theory and the derivation of the mathematical expressions for the radiation induced electric signals. The experimental data is now interpreted and compared with the expected behaviour of the photon drag signal as predicted by the proposed theory.

VIII 2.0 Longitudinal Measurement with E || c

As shown in Chapter VII, the radiation induced longitudinal photon drag current in tellurium with E || c configuration is expected to follow essentially relation (112) {see Section VII 7.4}

$$J \doteq \frac{2eKW}{3m_h(1-z)} (\tau_h - \tau_\ell) \qquad (112)$$

In addition, it was shown that, employing the estimated value of z and particularly the fact that τ_h is evaluated to be much greater than τ_ℓ, Equation (112) leads to an open circuit voltage described by Equation (113), {see Section VII 7.5}:

$$V = \frac{(1-R)(P-aN)W_0}{ec(P+aN)(P+N)} \left\{ \frac{1- \exp(-KL)}{1+R \exp(-KL)} \right\} \qquad (113)$$

In the case of tellurium when $E \parallel c$, the radiation absorption by holes is much greater than by electrons {refer to Section III 6.2.2}; consequently, $a << 1$ and thus the above expression reduces to the form:

$$V \approx \frac{(1-R)W_0}{ec(P+N)} \left\{ \frac{1- \exp(-KL)}{1+R \exp(-KL)} \right\} \qquad (114)$$

VII 2.1 Undoped Samples

VIII 2.1.1 Room temperature behaviour

Using the parameter values for undoped intrinsic tellurium crystals at room temperature given in Section VII 3.0, the expected signal magnitude from Equation (114) is 10 mV/MW cm^{-2}, this value is very closely confirmed by the experimental results described in Section VI 4.2.1.

The polarity of the measured electric signal corresponds to a short circuit current flow in the direction of light propagation; this result confirms, referring to Equation (112), that $\tau_h > \tau_\ell$ as discussed in Section VII 7.3.

VIII 2.1.2 Variation with temperature

The expected variation of the photon drag voltage with temperature, as depicted by Equation (114), depends on the carrier concentration explicitly through the (P+N) term,

and implicitly through the exponential terms involving the absorption coefficient K; it should be noted that both P, N, and K are functions of temperature; also, since the radiation absorption is due to free holes for $E \parallel c$, the absorption coefficient K is directly related to the hole concentration P.

a) Variation of the resistivity

Curve b in Figure 17 shows the measured sample resistance as a function of temperature. The sample resistance is theoretically inversely proportional to both the carrier concentrations, which in intrinsic semiconductors varies exponentially with temperature, and to the mobility which has approximately a $T^{-3/2}$ dependence; clearly the exponential dependence on temperature of the intrinsic carrier concentration is expected to dominate; thus, from 300 K to 180 K, the resistance in Figure 17 is seen to have an exponential dependence and is essentially proportional to $(P+N)^{-1} \approx (2n_i)^{-1} \approx \exp E_G/2k_BT$. From the slope of this curve, a valence - conduction band energy separation of approximately 0.35 eV is obtained which agrees favourably with the accepted value of 0.34 eV. Below 180 K the material becomes extrinsic as shown by the essentially constant measured resistance.

b) Variation of the photon drag signal

The temperature dependence of the measured voltage in undoped samples is shown in Figure 17a. For simplicity of interpretation, it is noted that the curve can be divided into three temperature regions, according to the rate at which the signal changes with temperature, namely 300-250 K, 250-180 K, and finally below 180 K.

i) The temperature range 300-250 K

Between 300 and 250 K, the measured open circuit voltage, curve a, is found to increase and is proportional to the sample resistance; it follows from the above arguments that the photon drag signal is inversely proportional to (P+N): this is consistent with Equation (114) where $KL > 2$ and the exponential terms in this equation are, therefore, much smaller than unity; specifically, at room temperature $KL = 7$, i.e. total radiation absorption takes place within the sample.

ii) The temperature range 250-180 K

Since K is a linear function of the hole concentration, below 250 K, KL is expected to gradually diminish below the value of 2 and consequently, the exponentials in Equation (114) begin to approach unity which causes the factor in Equation (114) involving the exponentials to become less than unity. Consequently, the voltage is no longer expected to be solely

proportional to $(P+N)^{-1}$ and thus the rate of increase of the voltage with temperature is decreased as is verified by the measurements.

iii) The temperature range below 180 K

Below 180K, as seen from the nearly constant portion of the resistance curve, the material becomes extrinsic implying that $P >> N$ and that the hole concentration becomes essentially constant and equal to the acceptor concentration. Consequently, the photon drag voltage is also expected to be essentially constant in this range of temperature. The slight decrease in the actual observed signal is due to the further decrease in K with decreasing temperature due to the increase in the energy separation between the valence sub-bands {24}; the latter is in fact larger than the incident photon energy of the CO_2 laser radiation. Note that the slight decrease in resistance observed in the same temperature range is a result of a hole mobility increase with decreasing temperature {12}.

VIII 2.2 Doped Samples

In the doped samples, the responsivity was measured at room temperature to be 7 mV/MW cm^{-2}. To obtain the theoretically expected magnitude of this signal, the hole concentration in the sample must be known. The hole concentration in the extrinsic crystals was determined indirectly

by taking an average of the ratios of the measured absorption coefficients for doped and undoped crystals with $E \parallel c$ for all wavelengths between 7 and 14 μ. It was found that the absorption coefficient in the doped sample was 2.1 times that in the undoped sample. Since for $E \parallel c$, the absorption is entirely dominated by holes, it is concluded that in the doped crystal $P = 2.1\, n_i = 10^{16} cm^{-3}$ and $N = n_i^2/P = 2.35 \times 10^{15} cm^{-3}$; substitution of these values into Equation (114) leads to a responsivity of 8 mV/MW cm^{-2} which is in a good agreement with the measured result considering the indirect method used in evaluating the carrier concentrations.

The temperature dependence of the measured photon drag signal in our extrinsic samples is shown in Figure 17c where it is seen that the signal is essentially constant with temperature, as expected, since the hole concentration, being equal to the acceptor concentration, remains unchanged with temperature. The observed slight increase of the voltage at low temperatures is not predicted by Equation (113) since it was derived from Equation (93) using the approximation that the magnitude of the factor within the curly brackets could be taken, for all temperatures, as being equal to $2\tau_h$ {refer to Section VII 7.4}. In fact, however, when the specific numerical values of the various parameters, as evaluated in Section VII 7.2 to VII 7.3.4 inclusive, are employed, it is found that this factor varies more exactly from a value of $1.6\tau_h$ at room temperature to $2.9\tau_h$ at 100 K;

therefore the induced signal is expected to increase by almost a factor of two over this temperature range which agrees favourably with the observed increase in the measured photon drag signal (see Figure 17c).

It was noted (see Section VI 4.2.2) that a similar increase in the measured photon drag voltage is also evident in undoped samples; this observable increase in the signal commences at a temperature of about 220 K (see Figure 17a) which is essentially identical to that seen in our doped crystal measurements.

Thus our rigorous mathematical solution of Boltzman's transport equation for the photon drag effect, based on direct hole transitions between parabolic valence bands, is verified in tellurium and the derived expressions explain fully all aspects of the experimental results.

VIII 3.0 Longitudinal Measurements with $E \perp c$

For polarizations perpendicular to the c-axis, the measured induced photon drag voltages, as presented in Section VI 6.0, were generally found to be small or below the measurability level of the experimental instrumentation. These low values for the generated voltages are explained with the help of the theory by examining the expression derived for the longitudinal photon drag signal when $E \perp c$ (see Section VII 9.0) where, in this case, the radiation is absorbed in

tellurium by electron and hole intraband transitions, such that

$$V = \eta \frac{(1-R)W_0(P-a\gamma N)}{ec(P+aN)(P+N)} \left\{ \frac{1- \exp - KL}{1+R \exp - KL} \right\} \qquad (115)$$

It is clear from the above expression that the contributions of holes and electrons, to the induced signal, tends to cancel each other. In addition, since for $E \perp c$ it is known that tellurium is relatively transparent at 10.6 μ, total absorption is not achieved, and therefore the exponentials in Equation (115) are near unity in magnitude. Thus, it is expected a priori that the photon drag effect for radiation polarized perpendicular to the c-axis is small.

In order to evaluate the magnitude of the photon drag signal for $E \perp c$, the values of a, γ and η in tellurium are required. Since no direct information on the latter parameters was found in the literature, we, therefore, now attempt to evaluate these parameters from our experimental results for the two independent longitudinal components consisting of the two pairs of equal matrix elements $T_{3311} = T_{3322}$ and $T_{2211} = T_{1122}$, respectively.

VIII 3.1 The Equal Components T_{3311}, T_{3322}

It is more convenient to start this discussion in terms of the results obtained from doped samples where larger signals were measured.

VIII 3.1.1 Doped samples

In our extrinsically doped crystals where K was measured to be 0.27 cm^{-1} {21}, P = $10^{16} cm^{-3}$, R = 0.43, L = 1.2 cm, and W_0 = 330 KW cm^{-2}, and if it is assumed that P >> N, $(P-a\gamma N)/(P+aN) \approx 1$, then Equation (115) predicts at room temperature an induced voltage of $.8\eta$ mV; when this value is compared with the measured voltage of 0.7 mV, it implies that for longitudinal measurements parallel to the c-axis, $\eta \approx 0.85$. With decreasing temperature, since P and K are expected to remain unchanged, the induced signal according to Equation (115) is also expected to remain constant; this is consistent with the experimental results shown in Figure 20.

VIII 3.1.2 Undoped samples

In intrinsic samples no measurable induced emfs were observed in our samples; thus in Equation (115) if η is assumed to remain of the same order of magnitude as in doped samples, it is concluded that the product $a\gamma$ is very close to unity.

a) Determination of the parameter "a" and "γ" from room temperature measurements

The parameter "a", which is the ratio of the radiation absorption cross-sections of the electrons and holes, is now estimated by using the absorption data given in Figure 5.

The total absorption coefficient K due to free carriers can be put in the form

$$K = \beta_n N + \beta_p P \tag{116}$$

and $a \equiv \beta_n/\beta_p$ where β_n, β_p are the absorption cross-sections for electrons and holes respectively.

Considering intrinsic materials first, where $N = P = n_i$, the absorption coefficient

$$K_i = \beta_p\, n_i (1+a) \tag{117}$$

In our doped material, on the other hand, $P = 2.1/n_i$, $N = n_i/2.1$ {refer to Section VIII 2.2}; thus, the absorption coefficient K_d, in this case, is given by

$$K_d = \beta_p\, n_i (2.1 + a/2.1) \tag{118}$$

Thus $$\frac{K_d}{K_i} = \frac{2.1 + a/2.1}{1 + a} \tag{119}$$

From Figure 5, the ratio of absorption coefficients for $E \perp c$ of our doped and undoped samples at 10.6 μ, is seen to be

$$\frac{K_d}{K_i} = \frac{.270}{.185} = 1.46 = \frac{2.1 + a/2.1}{1 + a} \tag{120}$$

and thus it follows that $a = 0.65$. However, it should be noted that a few percent uncertainty in both the ratio K_d/K_i and P/n_i can result in an up to 50% uncertainty in the

evaluated value of "a". With "a" taken to be 0.65, it clearly follows that $\gamma \simeq 1.5$.

The value of γ, which was defined as $\langle\langle \tau_- \rangle\rangle / \langle\langle \tau_+ \rangle\rangle$, the ratio of the effective scattering times of electrons and holes for the photon drag effect in intraband transitions, is now compared with τ_e/τ_h, the ratio of electron and hole momentum scattering times associated with mobility, i.e.

$$\frac{\tau_e}{\tau_h} = \frac{\mu_e}{\mu_h} \frac{m_e}{m_h} \tag{121}$$

From the literature {45}, {55}, in tellurium $\mu_e/\mu_h \simeq 2$ and since $m_e/m_h \simeq .5$ {refer to Section III 6.3} it follows from Equation (121) that $\tau_e/\tau_h \simeq 1$ which is consistent with our derived value of γ.

b) Expected magnitude at low temperatures

At low temperatures where the undoped material becomes extrinsically p-type, the cancellation effect of the electrons is no longer important; however, the induced signal is expected to remain small since the absorption coefficient K decreases substantially with a decrease in total carrier concentration and temperature; our resistance measurement indicates that at approximately 100 K, $P \simeq 10^{14} cm^{-3}$ and since {56}

$$K \propto (P + N)T \tag{122}$$

it therefore follows that

$$K(100\ K) \simeq \frac{10^{14}}{10^{16}} \times \frac{100}{300}\ K(300) \simeq 0.5 \times 10^{-3} cm^{-1} ;$$

thus from Equation (115), the expected open circuit voltage $V = 0.1$ mV results in a measurable voltage lower than the lower limit of measurability of 50 μV of our apparatus due particularly to the sample resistance becoming greater than the 50 Ω input resistance of the preamplifier.

VIII 3.2 The Equal Components T_{2211}, T_{1122}

In this case, since for both intrinsic and doped samples any possible induced signal was found to be below the lower limit of measurability of 50 μV, it is assumed that η for these tensor components is less than 0.2. This value is comparable to that found in similar experiments in n-type germanium by Gibson {54}

Our results, therefore, indicate an anisotropy in the value of η with different values for directions perpendicular and parallel to the c-axis; such behaviour is generally true for all properties of tellurium.

VIII 4.0 Transverse Measurements

As seen from Section V 4.0, the only finite transverse fourth rank tensorial components which may be measured separately namely T_{2311}, T_{2322}, T_{3211}, all involve

polarizations perpendicular to the c-axis. Since transverse photon drag voltages appear only as a result of anisotropies in the energy band, the corresponding generated signals are generally expected to be only a fraction ($\simeq$ 16% in Ge {57}) of the longitudinal components corresponding to the same radiation polarization. Thus, coupled with the arguments of the previous section which predict generally small longitudinal voltages with $E \perp c$, it is well expected that for both undoped and doped tellurium crystals, the transverse induced voltages due to the photon drag effect be very small as confirmed by our experimental results, presented in Chapter VI.

VIII 5.0 The Other Fourth Rank Tensor Components

The remaining four sets of independent tensor components are not separately measurable; their determination requires oblique and complex sample geometries where the induced signals are always the result of contributions from a combination of several independent tensor components, and are, consequently, extremely difficult to interpret.

Since for both electric transport and radiation propagation properties, the tellurium crystal directions 1 and 2 are known to be equivalent, it is expected that the equal matrix elements T_{1111} and T_{2222} are of the same magnitude as $T_{1122} = T_{2211}$; since the latter were measured and found to be small, the same is assumed to be the case for the former.

Also since the two sets of equivalent matrix elements $T_{2323} = T_{1312}$, and $T_{3232} = T_{3131}$ correspond to transverse measurements with, in addition, a component of radiation polarized perpendicular to the c-axis, they are also expected to be of small magnitude.

The last independent fourth rank tensor component T_{3333}, however, is expected to be of similar magnitude as the matrix elements $T_{1133} = T_{2233}$ as all three correspond to longitudinal measurements with polarization parallel to the c-axis. Since the induced voltages corresponding to the latter tensor coefficients are relatively large, an attempt was made to measure also T_{3333}; the sample geometry used is shown in Figure 24; this sample configuration is necessary so that we have a component of the radiation electric field as well as a component of the propagation direction simultaneously parallel to the 3-axis. No signal which could be attributed to the photon drag effect was monitored; this fact is explained by noting that since E_3, the component of the electric field parallel to the c-axis, is strongly absorbed and thus is of significant magnitude only near the surface of incidence, consequently, E_3 is negligibly small in the area of the sample falling directly between the electrical contacts across which the desired voltage corresponding to T_{3333} is expected to be measured.

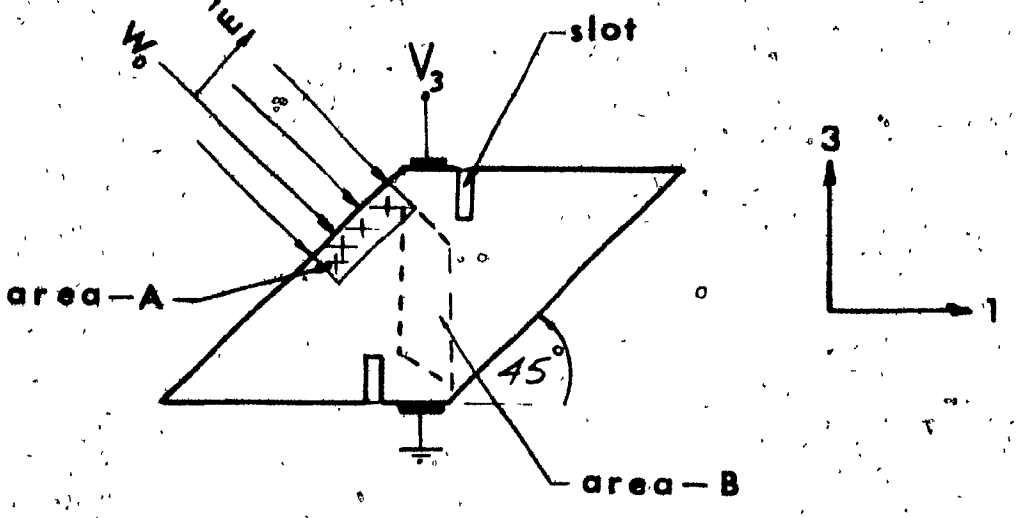

Figure 24. Sample Geometry for the Measurement of T^*_{3333}.

Slots are cut to ensure voltage measurements in the 3-direction.

area-A: actual region of absorption for E_3;
area-B: desired illuminated region.

VIII 6.0 Conclusions

In this chapter we have shown that, for the photon drag effect, a very favourable agreement, between the experimental results presented in Chapter VI and the theory formulated in Chapter VII, exists for all tensor components characterizing the various combinations of directions of radiation propagation, polarization, and voltage measurement. In particular, the theoretically predicted dependence of the open circuit photon drag voltage on such parameters as carrier type and concentration, absorption coefficient, temperature, and momentum scattering times has been verified by careful analysis of the experimental results. In the process of interpreting our results, the values of such quantities as the ratio of absorption cross-sections for electrons and holes, the ratio of the photon drag effective momentum scattering times for electrons and holes, and the efficiency of the photon momentum transfer to holes, have been evaluated.

In summary, it is concluded that the obtained photon drag signals are successfully interpreted by the theoretical presentation of the photon drag effect given in this work.

CHAPTER IX

THE SIGNAL WITH THE THIRD RANK TENSORIAL BEHAVIOUR

IX 1.0 Introduction

Optical rectification, as described by third rank tensorial coefficients which relate the measured rectified signal to the square of the radiation electric field, has been attributed to the interaction of light with either free {58} or bound charges {59}, {60}. In order to determine the nature of the generating mechanism for the presently observed signal that follows a third rank tensorial behaviour, an analysis of the expected characteristics of the induced signal is carried out for each of the two above mentioned interactions acting as the source.

IX 2.0 Light Interaction with Bound Charge

IX 2.1 Effect Due to Non-Linear Polarization

The square law response of bound charge to an incident radiation is described by non-linear polarization {61}. In general, the induced non-linear polarization P is related to the radiation electric field E at frequency ω by the relation

$$P_i(2\omega,0) = B'_{irs}\, E_r(\omega)\, E_s(\omega) \qquad (123)$$

where naturally the resulting induced polarization is composed of, first, a d.c or, in the case of a pulsed laser, a relatively slow time varying component proportional to the power pulse envelope, and in addition, a component varying at twice the radiation frequency ω.

The d.c or slowly varying component P_o of the polarization $P(2\omega,0)$ corresponds to optical rectification; it is only this component which is measurable in our case, and consequently of interest in the following analysis. It follows that

$$P_o = B' \tilde{E}^2 = BW \tag{124}$$

where W is the slow time varying amplitude of the laser power density and is directly related to $\tilde{E}^2$, the square of the radiation electric field amplitude.

From Maxwell's equations, the rectified current J in a material is given by

$$J = \frac{\partial D}{\partial t} + \rho^{-1}\mathcal{E} \tag{125}$$

with $$D = P_o + \varepsilon\mathcal{E} \tag{126}$$

where $J, D, \mathcal{E}$ are the locally induced d.c or, for the pulsed laser, the slowly varying components of the current density, dielectric displacement, and electric field respectively. Substituting Equations (124) and (126) into Equation (125) yields

$$J = \frac{\partial}{\partial t}(BW + \varepsilon \mathcal{E}) + \rho^{-1}\mathcal{E} \tag{127}$$

Assuming now that W, and consequently $\mathcal{E}$ and J can be written in a Fourier series expansion with frequency components ω_n, Equation (127) written for a particular Fourier component ω_n, becomes,

$$J_n(\omega_n) = j\omega_n B W_n(\omega_n) + [\, j\omega_n \varepsilon + \rho^{-1} \,]\, \mathcal{E}_n(\omega_n) \tag{128}$$

In conductors, i.e. for materials such as tellurium where $\rho^{-1} >> \omega_m \varepsilon$, ω_m being the maximum frequency component of W, it clearly follows that under open circuit conditions where J = 0,

$$\mathcal{E}_n(\omega_n) = - \rho B j\omega_n W_n \tag{129}$$

and upon transformation back into the time domain,

$$\mathcal{E}(t) = - \rho B \frac{\partial W}{\partial t} \tag{130}$$

Thus the measured signal, if due to bound charge is expected to follow expression (130) which shows that the observed generated signal should be proportional to the time derivative of the incident amplitude of the radiation power; this clearly disagrees with the experimental results where a true reproduction of the laser power is observed. It is therefore concluded that optical rectification in semiconductors via a non-linear polarization effect due to bound charge cannot be the source of the observed signals characterized by

the third rank tensorial coefficient χ contrary to the suggestion made in Reference {59}.

IX 2.2 Induced Signals Due to the Contribution of Electrostrictive Stress and Piezoelectric Polarization

Another mechanism that can be invoked to explain the induced emf characterized by the third rank coefficient χ, is the combination of electrostrictive stress and the resultant piezoelectric polarization.

It is known that a radiation electric field induces in all materials an electrostrictive stress which is a quadratic function of the electric field {62}. This stress displaces the atoms of a solid and also the electrons within the atoms themselves; when the material is also piezoelectric, these displacements produce microscopic dipoles which combine to give an average measurable macroscopic moment known as electrical polarization {63}.

Mathematically, this electrostrictive effect is described as follows:

$$T_{rs}(2\omega,0) = \gamma_{rsmn} E_m(\omega)\ E_n(\omega) \qquad (131)$$

where $T(2\omega,0)$ is the induced electrostrictive stress composed of a d.c or a relatively slow time varying component $T_{rs}(0)$ as well as a component varying at twice the radiation frequency ω; γ_{rsmn} is the fourth rank electrostriction coefficient.

Now the stress $T_{rs}(0)$, through the piezoelectric coefficient d_{irs}, yields the polarization

$$P_i(0) = d_{irs} T_{rs}(0) \tag{132}$$

Substituting Equation (131) into Equation (132) and using the appropriate transformation to express the induced stress in terms of the power density W, and combining all the coefficients into the parameter C, we get an expression for the polarization P of the form:

$$P = CW \tag{133}$$

This relation is identical to Equation (124), derived for the ordinary non-linear polarization effect discussed in Section IX 2.0, which would lead, in this case as well, to the conclusion that the generated signal resulting from induced polarization in a highly conductive material, such as tellurium, would manifest itself as an induced emf proportional to the time derivative of the laser power density which is clearly contrary to experimental observations.

IX 3.0 Light Interaction with Free Charged Carriers

A square-law current response, resulting from the interaction of the radiation electric field with the free charged carriers in a semiconductor, can be described as non-linear conductivity. The conduction current J in a material,

arising from the motion of N carriers with a velocity v is generally given as

$$J = eN(F)v(F) \tag{134}$$

The current J becomes non-linear with respect to the electric field F when v is non-linear in F or when N depends on F. These two cases are now considered in turn.

IX 3.1 Non-Linear Carrier Velocity

We first consider the case when the velocity depends non-linearly on the incident radiation electric field $F(\omega)$; particularly the motion of free charged carriers, characterized by a non-parabolic energy band, under the influence of the radiation field will be discussed.

For this situation Butcher {64} has shown that the current is given by Equation (135), where the radiation frequency ω is much larger than τ^{-1}, the reciprocal of the carrier momentum scattering time.

$$J_i = \sum_k f(k) \left[\frac{e^2}{j\omega m^*} F_r(\omega) - \frac{e^3}{2\hbar^3\omega^2} \frac{\partial E(k)}{\partial k_i \partial k_r \partial k_s} F_r(\omega) F_s(\omega) \right] \tag{135}$$

where $E(k)$ is the quantum mechanical energy of a carrier obtained from the appropriate solution of Schrodingers equation in the given material.

It is clearly seen that the first term corresponds to the well-known linear complex conductivity for $\omega >> \tau^{-1}$; the second term, being quadratic in $F(\omega)$, yields a rectified current component proportional to the third order derivative of the carrier energy and consequently to a cubic term in the momentum vector k in the energy dispersion relation.

For the case of the valence band in tellurium such a cubic term is known to exist, namely $C_1 k_x (k_x^2 - 3k_y^2)$ {see Equation (4)}, which then seems at first glance and as assumed by Herrmann {58} to imply that a quadratic response is possible due to non-parabolic energy bands. However, the application of the fundamental principle of time reversal symmetry which requires that $E(k) = E(-k)$, indicates that for every valence band maximum having a third order term with the coefficient C_1, there must exist another equivalent band extremum in which the third order term has a coefficient with the value $-C_1$. In fact, the two valleys involved correspond to the H and H' points of the tellurium Bruilloin zone {23}.

Thus the required summation of the second term in Equation (135) over all of k-space will result in an identically zero contribution to the total current. Therefore, it is concluded that time reversal symmetry prevents second order non-linear effects due to a non-linear velocity of charged carriers, from taking any finite magnitude in homogeneous materials {60}.

The above discussion shows clearly that the interpretation given by Herrmann, to the observation in tellurium of an induced signal with a third rank tensorial behaviour, as resulting from non-linear conductivity in that material is not acceptable.

IX 3.2 Effects Describable by an Electric Field Induced Variation of the Free Carrier Density

As stated previously, non-linear currents are also produced when the carrier concentration is itself a function of the electric field.

This type of non-linearity is known to occur in piezoelectric semiconductors when an acoustic wave of frequency ω, is propagating in such materials {65}, {66}. Such an acoustic wave, due to the piezoelectric effect, produces strongly coupled electric field and space charge waves, where electron-electric field non-linear interactions result in the simultaneous generation of new electrical and acoustical signals at the sum and difference values of the original frequencies.

A theoretical analysis of this interaction mechanism, initiated from the non-linear part of the cross-term $n(F)\,\mu F$ in the current density Equation (134), yields Equation (136) {66} which describes the d.c acoustoelectric field $\mathcal{E}_{ac}$, arising from the original acoustic wave of frequency ω,

interacting with the free carrier electrons;

$$\mathcal{E}_{ac} = - \frac{\mu e_p^2 \tilde{S}^2}{2\epsilon^2 v_s [1 + \omega_c/\omega + \omega,/\omega_D]^2} \qquad (136)$$

where:

$\tilde{S}$ is the magnitude of the strain in the material associated with the acoustic wave of frequency $\omega,$;

e_p is the appropriate component of the piezoelectric constant;

v_s is the phase velocity of the sound in the material at frequency $\omega,$;

$\omega_c = (\rho\epsilon)^{-1}$ is the dielectric relaxation frequency;

$\omega_D = v_s^2 e/k_B T\mu$ is the diffusion frequency.

It is to be noted that in acoustoelectric effects, electrons and holes produce signals of opposite polarity {67}; consequently the minus sign in Equation (136) becomes plus when evaluating the contribution to the induced field from free carrier hole-acoustic wave interactions.

Although in our present experiments no acoustic waves are introduced in a conventional way into the tellurium samples, the radiation electric field transmitted through the material can generate, via piezoelectric coupling, a strain corresponding to a strain wave of frequency equal to that of the incident radiation {68}, described by a strain component

$$S(\omega) = \frac{\varepsilon}{e_p} F(\omega) \qquad (137)$$

To our knowledge, acoustic waves, at the high frequencies involved in this discussion, have previously not been considered and dealt with in the acoustoelectric effect. In view of this fact, we now develop a description of the likely behaviour and propagation characteristics of such high frequency generated strain waves in a material.

At any particular instant of time t_1, a strain is expected to be induced at each point within the illuminated part of the sample with an instantaneous amplitude which is directly proportional to the amplitude of the radiation electric field as described in Equation (137); thus this strain has the spatial pattern and correspondingly an apparent wavelength equal to that of the radiation (see Figure 25).

Subsequently, as time progresses, such as at $t_2 > t_1$, the mechanical disturbance in the material is expected to be the resultant of the two following effects:

a) the radiation, which has propagated in the material at the speed of light, correspondingly induces instantaneously and at each point, a strain which at t_2 results in a strain pattern similar to that existing at t_1, but displaced synchronously with the radiation field as shown in the Figure 25.

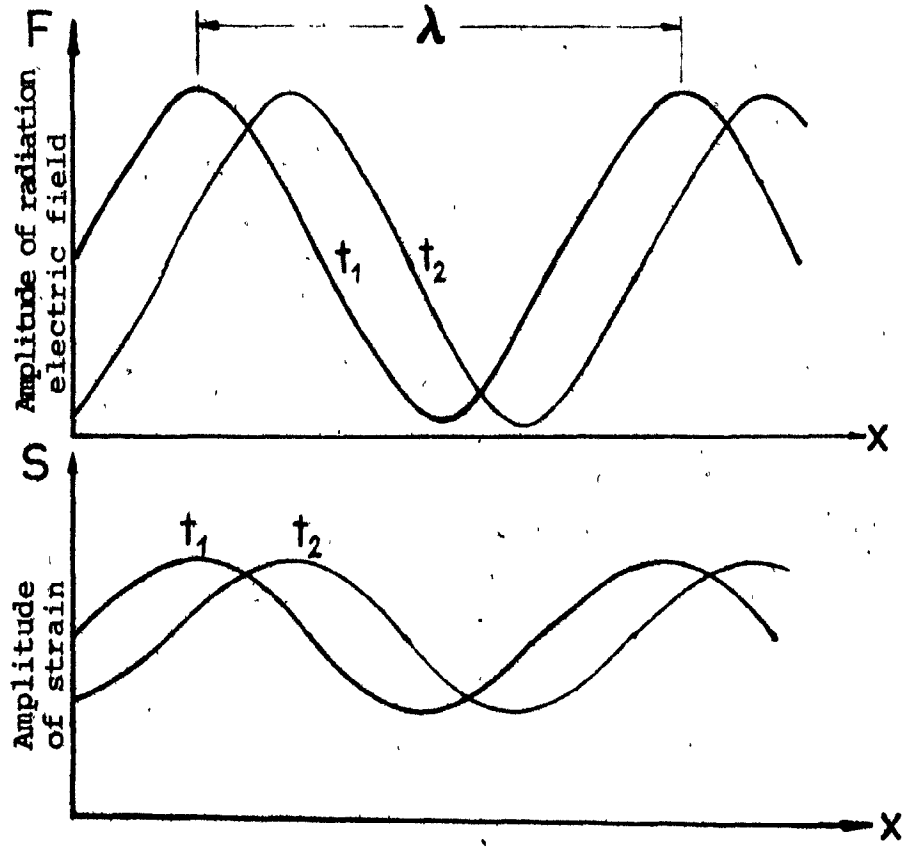

Figure 25. Radiation Electric Field and Corresponding Induced Strains at Two Instances of Time t_1 and t_2 Within the Material.

b) the strains induced previously at each point at the instant t_1, will naturally tend themselves to initiate, from each point, strain waves at frequency ω of the radiation field which would tend to propagate through the sample; however, at these high frequencies, these latter strain waves, originating at each point, are expected at best to be highly attenuated, and not to propagate any appreciable distance, compared to the radiation wavelength. In fact, information available on phonon frequencies in tellurium {69}, indicate that no phonons are known to be sustained in this material at frequencies above $3 \times 10^{13} s^{-1}$.

Therefore, at any time, the total strain within the sample consists solely of that which is instantaneously generated by the radiation. Thus the net effect within the material, is that an acoustic disturbance exists which appears to be directly coupled or locked to the applied electromagnetic radiation, having an identical amplitude variation in time and, therefore, the same wavelength and phase velocity.

Having thus established the characteristics of the acoustic wave-like disturbance present in tellurium exposed

to the laser radiation, we are now in a position to evaluate the induced measurable acoustoelectric signal by using the appropriate values of the parameters in Equation (136). Thus, for a radiation power density of 165 KW cm^{-2}, the amplitude of the radiation electric field in tellurium is calculated to be 5.1×10^5 V/m; it follows that, with $\varepsilon = 23\ \varepsilon_o$ and $e_p = .6 c/m^2$ [13], Equation (137) yields that $\tilde{S} = 1.7 \times 10^{-4}$. Now for this magnitude of strain at frequency $\omega_1 = \omega = 1.9 \times 10^{14} s^{-1}$, with $v_s = 3 \times 10^8 ms^{-1}$ and $\mu \simeq .1/m^2V^{-1}s^{-1}$, Equation (136) predicts, for the acoustoelectric induced electric field, a value of $\mathcal{E}_{ac} = 0.4$ V/cm.

It is to be noted, however, that Equation (136) was derived with trapping effects neglected; in fact some of the space charge produced by the strain wave may be trapped at states within the forbidden energy gap. These immobile charges do not participate in conduction and thus the resultant induced signal may be appreciably reduced from the value evaluated above. Also, it must be noted that the value assigned to the piezoelectric effect in the previous numerical evaluation was that associated with microwave frequencies; it is expected that at the optical frequencies involved, the effective piezoelectric coefficient ε/e_p will be smaller in magnitude.

As stated previously, electrons and holes produce acoustoelectric signals of opposite polarity, and therefore,

the net induced emf is expected to be the algebraic sum of contributions from both types of carriers.

IX 4.0 Interpretation of the Present Experimental Results

In the previous sections, we have presented the theories of four different types of mechanisms by which radiation induced emfs may occur in tellurium. Before we may relate the observed signal, that follows a third rank tensorial behaviour, to one of the latter mechanisms, our experimental results, presented in Section VI 3.0, must be analyzed, interpreted, and summarized. It may be deduced from Figure 13 that in undoped crystals the signal with the third rank tensorial behaviour remains constant from room temperature down to 220 K, then increases in magnitude down to 180 K and remains essentially constant at lower temperatures; it is noted that in these three temperature ranges the relative concentrations of holes and electrons are as follows: in the upper temperature range the material is intrinsic with equal hole and electron concentrations; in the intermediate temperatures the electron minority carrier concentration decreases more rapidly compared to the majority carrier concentration of holes; and at the lowest temperature range the material becomes extrinsic with a constant concentration of holes which is several orders of magnitude above that of the further decreasing concentration of electrons.

Considering now the results in a doped sample shown in Figure 16, the coefficient χ^* at room temperature in doped samples is evaluated to be three times its value in the undoped material; also, in this case, the induced voltage is found to be fairly constant with temperature; the slight decrease with lower temperatures is noted to be essentially proportional to the corresponding decrease in resistivity of the material.

Thus our experimental results seem to indicate that the induced signal depends on the carrier type and concentration, with holes and electrons producing emfs of opposite polarity. These observations lead us to believe that the source of the generated emfs is most closely related to a non-linear conductive effect.

IX 5.0 Conclusions

In this chapter, four different mechanisms have been considered and critically discussed as the possible sources for the observed signal exhibiting third rank tensorial behaviour.

The first two mechanisms, known respectively as non-linear polarization and electrostrictive-piezoelectric effects, involve the interaction of the laser radiation with bound charges; it has been concluded that these mechanisms could not be the source of the measured emfs since they are clearly

independent from the type of free carrier present; furthermore, bound charge dependent signals have been shown to result in signals proportional to the time derivative of the laser power density which is contrary to our experimental observations.

The remaining two mechanisms involve interaction with free charged carriers. In the first of these effects, the application of the fundamental principle of time reversal symmetry, resulted in the conclusion that the existence of non-linear velocity of free charged carriers due to non-parabolic energy bands in a material, cannot manifest itself in any second order non-linear conductive effects.

The non-linear acoustoelectric effect involving the presence of radiation generated high frequency acoustic disturbances via piezoelectric coupling, has the necessary features leading to an induced emf which is linearly related to the laser power density and such that holes and electrons produce signals of opposite polarity.

However, the following discrepancies are noted in this proposed mechanism: the calculated magnitude of the expected signal is about forty times larger than observed in our extrinsic samples where the electron-hole cancellation effects are negligible; furthermore, Equation (136) predicts that the generated signal is directly proportional to the mobility and thus, in extrinsic material, the measured signal

is expected to increase with the mobility as the temperature is lowered, which is contrary to our observations. Both discrepancies in magnitude, and temperature dependence, however, between theory and experimental results, may be explained by invoking the idea of trapping effects; the presence of trapping would indeed reduce the expected signal magnitude; also, its effect is known to generally increase strongly with decreasing temperature, thereby over-riding the temperature dependence of the mobility. Furthermore, it was noted in Section IX 3.2 that the effective piezoelectric coefficient at the very high frequency involved, in this phenomenon, is expected to be reduced below its low frequency value given by Reference {13}. It seems thus possible to propose that the acoustoelectric effect is responsible for the observed emf characterized by the coefficient χ .

CHAPTER X

PRACTICAL DETECTOR CONFIGURATIONS

X 1:0 Introduction

From the experimental results presented in Chapter VI, it follows that the photon drag effect and the mechanism characterized by third rank tensorial behaviour are sufficiently intense and fast in a tellurium sample to be used as mechanisms for the detection of pulsed CO_2 laser radiation. In this chapter, various practical detector configurations are discussed so that optimum device performance is achieved. In general, the devices used to measure laser output power fall into two classes:

a) Detectors, where all the laser radiation is absorbed.

b) Monitors, which are traversed by the laser beam and allow most of the incident radiation to be transmitted.

The performance of tellurium in such devices, utilized for CO_2 laser radiation, is now presented in both detector or monitor configurations, and compared with other existing devices.

X 2.0 Tellurium CO_2 Laser Detectors

The radiation induced electric field $\mathcal{E}$ within the sample can be written from Equation (14) in the form:

$$\mathcal{E}_i = [\, T^*_{ijmn}\, \hat{q}_j + \chi^*_{imn}\,] W e_m e_n \qquad (138)$$

It has been shown {Section VI 2.1} that the longitudinal voltage across a sample of length L, neglecting multiple reflections is given by

$$V_i = [\, T^*_{ijmn}\, \hat{q}_j + \chi^*_{imn}\,] \frac{W_o(1+R)}{K} \quad (1 - \exp - KL)\, e_m e_n \qquad (139)$$

where K, R are the radiation polarization dependent absorption and reflection coefficients, respectively.

From experimental results, it is found that only T^*_{1133}, T^*_{2233} and χ^*_{111}, χ^*_{212}, χ^*_{122} are of significant magnitude to be of practical interest for radiation detecting devices. By inspection of the subscripts associated with each of above tensor coefficients, it is seen that the T's are non-zero for $E \parallel 3$ or c whereas the third rank tensors involve polarization components of $E \perp c$. Thus Equation (139) can clearly be rewritten in the form:

$$V_i = \frac{T^*_{\parallel}}{K_{\parallel}} (1-R_{\parallel}) W_{\parallel} \quad (1 - \exp - K_{\parallel} L) + \frac{\chi^*_{\perp}}{K_{\perp}} (1-R_{\perp})\, W_{\perp} \quad (1-\exp-K_{\perp} L) \qquad (140)$$

where the values of all parameters are finite only for the radiation polarization indicated by their subscripts.

Since it was found that in tellurium at 10.6 μ, the magnitudes of $T_{\parallel}^{*}$ and $\chi_{\perp}^{*}$, $R_{\parallel}$ and $R_{\perp}$ are approximately equal, but $K_{\parallel} >> K_{\perp}$, it can easily be estimated that the third rank tensorial effect induces larger voltages for sample lengths $L > 0.5$ cm. Therefore it is more appropriate to use the emf generating mechanism characterized by χ than the photon drag effect when high responsivity is desired. However, when ultra-fast detectors are required, the photon drag effect becomes of interest, as will be discussed in Section X 2.2.

X 2.1 Detection Using the Third Rank Tensorial Effect

a) Responsivity

Considering now, detectors using the third rank tensorial effect, it was found from experimental results {Section VI 3.2} that at room temperature, for extrinsic material, χ^{*} is threefold larger than in an intrinsic material. Thus a longitudinal detector cut from such a material to a typical length of 2 cm, as is commonly used for germanium photon drag detectors, and oriented with the long dimension in the direction of the 1 axis, with the incident light beam polarized parallel to the 2 direction, generates a voltage given by

$$V_1 = \frac{\chi^{*}}{K_{\perp}} (1-R)W_0 \frac{(1- \exp- K_{\perp}L)}{(1-R \exp- K_{\perp}L} \qquad (141)$$

where the effect of multiple reflections has been included. With $\chi^* = 0.7 \times 10^{-7}$ cm/A, $R_\perp = 0.43$, and $K_\perp = 0.27$ cm^{-1}, Equation (145) yields that

$$V_1/W_0 = 80 \ \mu V/KW \ cm^{-2} .$$

Thus, a detector of 4 x 4 mm^2 cross-section has a responsivity of 0.5 mV/KW which is almost four times better than for commercially available germanium photon drag detectors of the same dimensions, for example Oriel Model 7411 (imported from Rofin Ltd., England).

It must be noted that the tellurium detector just described absorbs only half of the incident radiation; if total absorption was allowed either by increasing fourfold the absorption coefficient employing more highly doped material, or by increasing the length of the sample fourfold, the responsivity would have been increased almost twofold. Antireflection coatings on the incident surface will increase the magnitude of the signal by an additional factor of two.

Finally, it must be noted that the quoted responsivities are for linearly polarized light; the use of unpolarized radiation would reduce the signal induced in this detector by a factor of two.

b) Noise and detectivity

Since the described detector is a photo-voltaic device used without any electric current being applied, the

only source of noise within the material is thermal or Johnson's noise; the magnitude of the noise rms voltage $\bar{v}$ per unit bandwidth is given by

$$\bar{v} = \left[4 k_B T R_s \right]^{1/2} \qquad (142)$$

where $k_B T$ is the thermal energy and R_s is the sample resistance. The resistance R_s of the sample, with the previously stated dimensions and cut from our extrinsic material whose measured resistivity is 0.75 ohm-cm, is calculated to be 10 Ω, which then yields at room temperature a noise voltage

$$\bar{v} = 4 \times 10^{-10} V \quad .$$

Using the previously calculated detector responsivity of 0.5 mV/KW, an NEP {see Section II 2.0} of 8×10^{-4} W/Hz$^{1/2}$ is evaluated, which then corresponds, for the detector area of 16 mm^2, to a detectivity D^* {see Section II 2.0} of 500 cm Hz$^{1/2}$/W.

It is noted that the above performance parameters are appreciably better than for the Molectron Model P5, 500 ps rise time pyroelectric detector, which has a given NEP of 10^{-1} W/Hz$^{1/2}$ and a D^* of 3 cm Hz$^{1/2}$/W.

c) Speed of response

As discussed in Section VII 9.0 for the case of the photon drag effect, the speed of response of any photodetector

is generally limited by the following three fundamental times: the dielectric relaxation time, the light transit time through the sample, and a characteristic response time of the emf generating mechanism.

If the acoustoelectric effect is taken to be the mechanism responsible for producing the signal characterized by the third rank tensor coefficient χ, the fundamental response time for this effect would involve the decay rate of the radiation induced strains. On the basis of the previously discussed assumption, that the acoustoelectric strains decay within a distance much smaller than the wavelength of light, it is inferred that the decay time is shorter than the propagation time of the light beam within the material. Also, for a sample length of 2 cm, the light transit time in tellurium for $E \perp c$ is 3.3×10^{-10}s, which is much longer than the dielectric relaxation time of 1.2×10^{-12}. It thus follows that the light transit time through the sample is the fundamental limitation in the speed of response for the described tellurium detector. If faster response speeds are desired, shorter sample lengths must be used which then result in a loss in the responsivity {refer to Equation (141)}.

X 2.2 Comparison of Tellurium Photon Drag and Third Rank Tensorial Effect Detectors

From our experimental results, it was found that the

responsivity at room temperature of the tellurium photon drag detector with a sample length greater than 5 mm is 10 $\mu V/KW^{-2}$, which, although eight times smaller than in a device of 2 cm length employing the third rank tensorial effect, is sufficient to detect high power pulsed CO_2 laser radiation. Furthermore, when response times of less than 10^{-10}s are required, sample lengths of less than 5 mm are necessary; in this case, the emf induced by the photon drag effect becomes comparable to that associated with the third rank coefficient χ. In addition, since the photon drag effect was found important only for radiation polarized parallel to the c-axis, and recalling that χ involves polarizations only perpendicular to the c-axis, it can be seen that when such short devices are used to detect unpolarized radiation, both the photon drag and third rank tensorial effects will contribute to the output voltage of the device; consequently, the responsivity of these detectors can be made to be practically independent of the incident radiation polarization.

X 3.0 Tellurium CO_2 Laser Monitors

X 3.1 Single Element Monitors

In certain applications, where it is necessary to detect the laser beam without affecting its intensity or geometry, a device must be used which transmits undisturbed essentially all the incident radiation power. Samples with

the geometries shown in Figure 26 can be used for such devices which are normally of large area and are called "beam monitors". These sample configurations require the voltage to be measured transverse to the laser beam propagation direction; since the transverse photon drag effect was found to be negligible in tellurium, only the third rank tensorial effect is applicable for such devices. Furthermore, as this mechanism generates finite emfs only for radiation polarized perpendicular to the c-axis, the amount of radiation lost due to absorption within these samples is negligible; in addition by employing antireflection coatings on the surfaces, the samples, should transmit essentially all the laser power.

From Equation (19), when $R = 0$ due to the anti-reflection coatings, the voltage induced by the third rank tensorial effect is given by

$$V = \chi^* W_o d \qquad (143)$$

where d is the illuminated distance between the contacts.

Thus for an extrinsic tellurium monitor having a 23 mm diameter clear aperture a responsivity of 39 mV/MW is expected to be achieved which is a factor of 7 larger than the commercially available germanium transverse photon drag beam monitor, Oriel Model 7412, known to transmit 95% of the radiation.

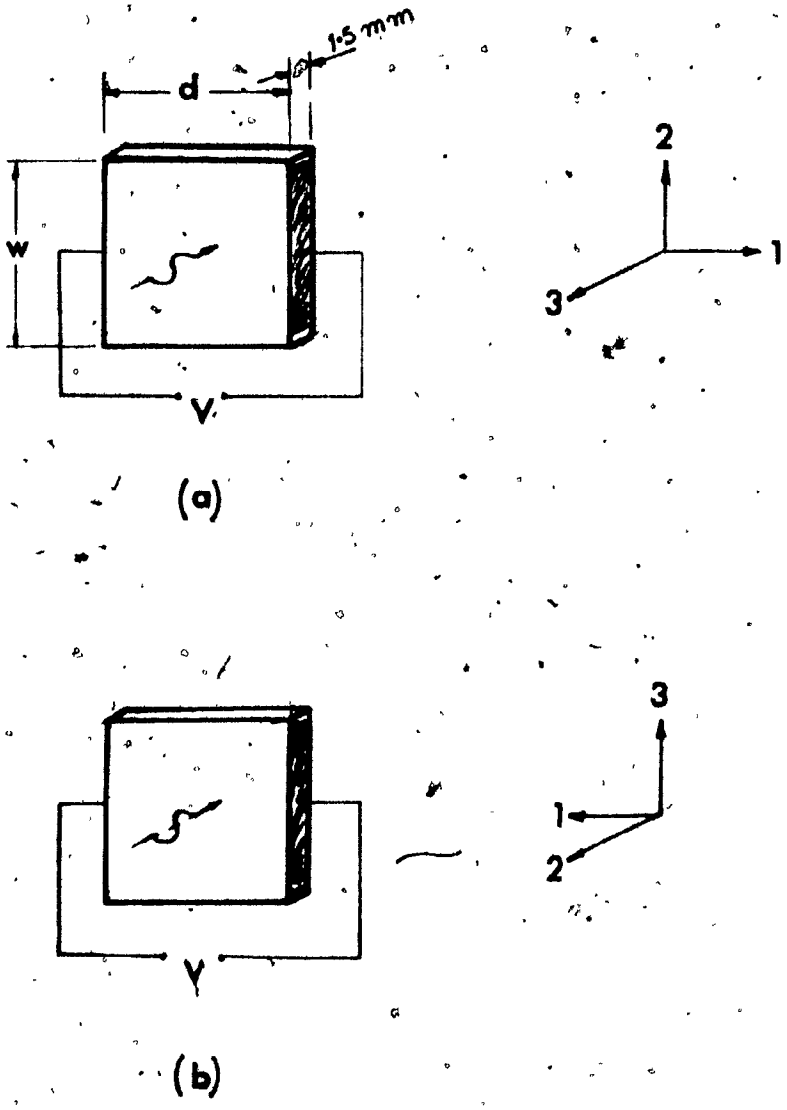

Figure 26. Practical Tellurium "Laser Beam Monitor" Device Configurations.

a) Maximum signals obtained with E || 1 or 2 directions;

b) Maximum signal obtained with E || 1 direction.

X 3.2 Multi-Element Monitors

It is noticed in Equation (143) that only the illuminated distance, d, between the contacts (see Figure 26) affects the magnitude of the induced voltage and the width of the sample is immaterial. In other words, a sample with a decreasing width $w \to 0$ produces an identical signal to a sample with $w \to \infty$. It follows that the responsivity of large area monitors can be increased by cutting the original area into multi-element strips and electrically connecting them in series as shown in Figure 27a. Thus if we cut n such strips of length d and of width w/n, the induced open circuit voltage and correspondingly the responsivity becomes n times larger than that of a single sample of the same overall dimensions.

Experimentally, this expected increase in responsivity has been verified by constructing a three element device (see Figure 27b).

X 4.0 Conclusions

It has been shown that tellurium is an attractive material to use for the detection and monitoring of pulsed CO_2 laser radiation. Although the photon drag effect in tellurium is of sufficient magnitude to be used as the source for the detection of high power pulsed CO_2 laser radiation, it is found that the mechanism characterized by the third

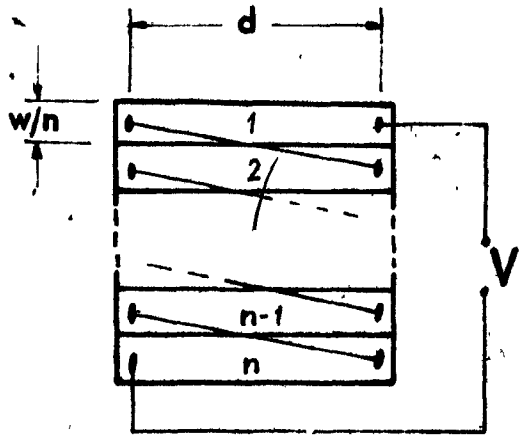

(a)

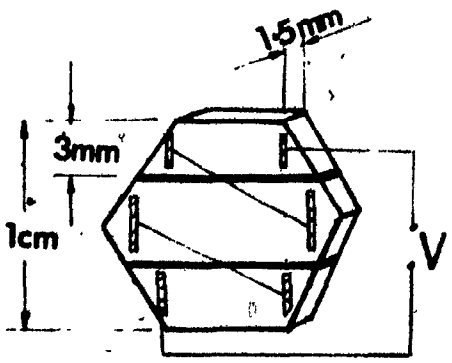

(b)

Figure 27: Multi-element Monitors.

a) a proposed n-element device.
b) an actually constructed 3-element device.

rank tensorial coefficient induces larger emfs. In fact, the responsivities of the tellurium devices employing the latter effect are superior to those of commercially available germanium photon drag devices.

CHAPTER XI

CONCLUSION

This thesis has presented the first comprehensive set of measurements and interpretation of the fast emfs generated in single crystal tellurium by pulsed CO_2 laser radiation.

Three distinct mechanisms have been identified as the sources responsible for inducing the fast signals in tellurium; these mechanisms are characterized respectively by a fourth rank tensor coefficient corresponding to the photon drag effect, a third rank tensorial coefficient that can be attributed to a carrier concentration dependent non-linear conductive effect, finally the third signal is attributed to spurious behaviour that is significant only in undoped samples at low temperatures and is observed to be related in general to imperfections in the tellurium single crystal structure.

A phenomenological tensorial analysis was first given which defined the particular combinations of the measurement, radiation propagation and polarization directions so that the third and fourth rank tensor components could be identified and measured separately. Using the above analysis, the magnitudes of the induced open circuit voltages associated with the various third and fourth rank tensor matrix elements in both undoped and doped tellurium samples have been

determined in the temperature range between 115 and 300 K.

The experimental results showed that for the photon drag effect, the only tensor components of significance are those corresponding to longitudinal measurements with radiation polarized parallel to the c-axis, i.e. $T^*_{1133} = T^*_{2233}$ which in undoped and doped crystals are respectively equal to 0.85×10^{-7}cm/A and 1.1×10^{-7}cm/A at room temperature. In the case of the third rank tensor coefficient, only the equivalent components $\chi^*_{122} = \chi^*_{212} = -\chi^*_{111}$ are large with room temperature magnitudes of 0.25×10^{-7}cm/A and 0.7×10^{-7}cm/A in undoped and doped tellurium crystals respectively.

In order to acquire a thorough understanding of the photon drag effect in tellurium such that an interpretation of the experimental results could be given, a theoretical analysis of this effect has been carried out: the analysis was developed in three stages leading from a macroscopic to a detailed microscopic discussion of the generating mechanism and its dependence on the various physical parameters of tellurium. A very favourable agreement between the experimental results and theory has been found to exist for all the photon drag tensor components. Furthermore, in the process of interpreting the results, information on the electron and hole absorption cross-sections and momentum scattering times were obtained.

In the case of the signal exhibiting third rank

tensorial behaviour, four different mechanisms were critically discussed as possible sources: non-linear polarization, the combination of electrostriction and piezoelectricity, non-linear carrier velocity, and non-linear acoustoelectric effects, have been investigated; it has been shown that only the latter effect can be proposed as the possible source responsible for the observed emf characterized by the third rank coefficient.

The third of the emf generating mechanisms is deemed spurious in nature as the magnitudes of the corresponding induced signals vary substantially from sample to sample. Also, it cannot be described by a tensor coefficient of any specific rank. However, a correlation between the presence and magnitude of this signal, and crystal imperfections has been observed to exist.

In conclusion, it is shown that tellurium is an attractive material to be used for the detection and monitoring of pulsed CO_2 laser radiation. The performance of tellurium devices, in various sample configurations, and using particularly the third rank tensorial effect, are found to be superior in general to commercially available germanium photon drag devices, and even to pyroelectric detectors when ultrafast response times are desired.

APPENDIX I

Taylor Series Expansions

In general, the first two terms of the Taylor series expansion for a function $\psi(x)$ around the point x_o is given by

$$\psi(x) = \psi(x_o) + \frac{\partial \psi}{\partial x_o}\, \delta(x) \qquad \text{(A1)}$$

where $\psi(x_o) \equiv \psi(x)\Big|_{x = x_o}$

$$\frac{\partial \psi}{\partial x_o} \equiv \frac{\partial \psi}{\partial x}\Big|_{x = x_o}$$

and $\delta(x) = x - x_o$

a) Expansion of $\tau_\alpha(E_k)$

Using Equation (A1), the Taylor series expansion of $\tau_\alpha(E_k)$ about k_o becomes,

$$\tau_\alpha(E_k) = \tau_\alpha(E_{k_o}) + \frac{\partial \tau_\alpha}{\partial k_o}\, \delta k_\alpha \qquad \text{(A2)}$$

b) Expansion of $\frac{\partial E_k^\alpha}{\partial k_i}$

Since it is assumed that

$$E_k^\alpha = \hbar^2 k_\alpha^2 / 2 m_\alpha$$

it follows that

$$\frac{\partial E_k^\alpha}{\partial k_i} = \frac{\hbar^2 k_{\alpha i}}{m_\alpha} \tag{A3}$$

where $k_{\alpha i}$ is the component of k_α in the i^{th} direction. From Equation (75) we now get that

$$k_{\alpha i} = a_i k_\alpha \tag{A4}$$

Thus $$\frac{\partial E_k^\alpha}{\partial k_i} = \frac{\hbar^2 a_i k_\alpha}{m_\alpha} = \frac{\hbar^2 a_i}{m_\alpha} \left[k_o + \delta k_\alpha \right] \tag{A5}$$

c) Expansion of $f_o(E_k^\alpha)$

From Equation (A1)

$$f_o(E_k^\alpha) = f_o(E_{k_o}^\alpha) + \frac{\partial f_o(E_{k_o}^\alpha)}{\partial k_o} \delta k_\alpha \tag{A6}$$

Assuming now that Boltzman's statistics are applicable

$$f_o(E_{k_o}^\alpha) = \exp -(E_{k_o}^\alpha - E_F)/k_B T \tag{A7}$$

$$\frac{\partial f_o(E_{k_o}^\alpha)}{\partial k_o} = - \frac{\exp - (E_{k_o}^\alpha - E_F)}{k_B T} \frac{\partial E_{k_o}^\alpha}{\partial k_o}$$

$$= - \frac{f_o(E_{k_o}^\alpha)}{k_B T} \frac{\hbar^2 k_o}{m_\alpha}$$

$$\frac{\partial f_o(E_{k_o}^\alpha)}{\partial k_o} = - \frac{2\varepsilon_\alpha}{k_B T k_o} f_o(E_{k_o}^\alpha) \tag{A8}$$

where $$\varepsilon_\alpha \equiv \frac{\hbar^2 k_o^2}{2m_\alpha} \tag{A9}$$

Substituting Equation (A8) into (A6), yields that

$$f_o(E_k^\alpha) = f_o(E_{k_o}^\alpha) \left[1 - \frac{2\varepsilon_\alpha}{k_B T k_o} \delta k_\alpha \right] \qquad \text{(A10)}$$

d) Expansion of the Dirac delta functions

From the properties of the δ function given in Reference {71}, it is found that

$$\delta(r(t)) = \sum_i \frac{1}{\left| \frac{\partial r(t_i)}{\partial t_i} \right|} \delta(t - t_i) \qquad \text{(A11)}$$

where t_i are the zeroes of $r(t)$.

The zeroes of $E^h_{\vec{k}} + \hbar\omega - E^\ell_{\vec{k}+\vec{q}}$, from Equation (71) are

$$k_h = k_o + \delta k_h .$$

Since

$$\left| \frac{\partial (E^h_{\vec{k}} + \hbar\omega - E^\ell_{\vec{k}+\vec{q}})}{\partial k_o} \right| = \left| \hbar^2 k_o \left[\frac{1}{m_h} - \frac{1}{m_\ell} \right] \right|$$

$$= \frac{\hbar^2 k_o}{m_\ell} (1-z) \quad \text{for } z < 1 \qquad \text{(A12)}$$

$$\therefore \quad \delta(E^h_{\vec{k}} + \hbar\omega - E^\ell_{\vec{k}+\vec{q}}) = \delta(k_h - k_o - \delta k_h) \Big/ \frac{\hbar^2 k_o (1-z)}{m_\ell} \qquad \text{(A13)}$$

Similarly

$$\delta(E^h_{\vec{k}+\vec{q}} + \hbar\omega - E^\ell_{\vec{k}}) = \delta(k_\ell - k_o - \delta k_\ell) \Big/ \frac{\hbar^2 k_o (1-z)}{m_\ell} \qquad \text{(A14)}$$

e) Expansion of k^3

The use of Equation (A1) yields that

$$k^3 = k_o^3 + 3k_o^2\,\delta k \qquad \text{(A15)}$$

REFERENCES

(1) A.J. Beaulieu, "Transversely excited atmospheric pressure CO_2 lasers," Appl. Phys. Letters 16, 504 (1970).

(2) A.F. Gibson, M.F. Kimmitt, and A.C. Walker, "Photon Drag in Germanium," Appl. Phys. Letters 17, 75 (1970).

(3) A.M. Danishevskii, A.A. Kastal'skii, S.M. Ryvkin, and I.D. Yaroshetskii, "Dragging of Free Carriers by Photons in Direct Interband Transitions in Semiconductors," JETP 31, 292 (1970).

(4) T.S. Moss, "Photon Pressure Effects in Semiconductors," Phys. Stat. Solidi (a) 8, 223 (1971).

(5) E.H. Putley, "Modern Infrared Detectors," Phys. Tech. (G.B.) 4, 202 (1973).

(6) W.C. Cooper ed., "Tellurium," Van Nostrand Reinhold Co., Chap. 3, 1971.

(7) D.A. Abokarov, E.Y. Banyulis, G.B. Bagduev, G.A. Ivanov, N.G. Polikhronidi, and V.I. Chernobai, "Acceptor Action of Dislocations in Pure Tellurium," Sov. Phys. Semicond. 7, 402 (1973).

(8) A.D. Riccius, "Vergleich der optishen and elekrishen Eigenschaften von Tellur," Ph'D Thesis, Koln University, (1964).

(9) W. Hoerstel, D. Kusnick, and M. Spitzer, "High-Field Transport and Low-Field Mobility in Tellurium Single Crystals," Phys. Stat. Solidi (b) 60, 213 (1973).

(10) J.C. Doukhan, R. Drope, J.L. Farvacque, E. Gerlach, and P. Grosse, "The Hole Mobility in a - Edge Dislocated Tellurium Crystals," Phys. Stat. Solidi (b) 64, 237 (1974).

(11) E. Thalymayr, H. Kahlert, and H. Kazmany, "Ohmic and Non-Ohmic Transport in Undeformed and Plastically Deformed Tellurium," Phys. Stat. Solidi (b) 65, 729 (1974).

(12) C.H. Champness and A.L. Kipling, "Transport Measurements in Annealed Single Crystal Tellurium, "Can. J. Phys. 48, 3038 (1970).

(13) J.V. Arnold, G. Nimtz, and E.P. Roth, "Anisotropic Current Decay in Tellurium due to the Acousto-Electric Effect," Phys. Stat. Solidi (b) 44, 469 (1971).

(14) G. Arlt and K. Reiber, "Ultrasonic Amplification in Tellurium Along the z-axis with Longitudinal and Transverse Electric Drift Fields," Solid State Commun. 7, (1969).

(15) A. Muller, "The Incubation Time of Acoustoelectric Effect in Te," Phys. Stat. Solidi (a) 4, K119 (1971).

(16) J.D.H. Donnay, "Crystal Data Determination Tables," (American Crystallographic Assoc.), Oak Ridge, Ten. (1963).

(17) J.H. McGee, G.D. Boyd, and P.H. Schmidt, "Redetermination of the Nonlinear Optical Coefficients of Te and GaAs by Comparison with Ag_3SbS_3," Appl. Phys. Letters 17, 57 (1970).

(18) J. Taynai, R. Targ, and W. Tiffany, "Investigation of Tellurium for Frequency Doubling with CO_2 Lasers," IEEE J. Quantum Electronics 7, 412 (1971).

(19) C.K.N. Patel, "Parametric Amplification in the Far Infrared," App. Phys. Letters 9, 332 (1966).

(20) E.L. Ivchenko and G.E. Pikus, "Natural Optical Activity of Semiconductors (Tellurium)," Sov. Phys. Solid State 16, 1261 (1975).

(21) S. Ades, M. Eng. Thesis, McGill University, 1975.

(22) S. Tutihasi, Phys. Rev. 177, 1143 (1969).

(23) R. Enderlein and A. Hache, "Valence and Conduction Band Structure and Infrared Optical Properties of Tellurium in the Presence of Pressure," Phys. Stat. Solidi (b) 60, 739 (1973).

(24) D. Fischer, E. Bangert, and P. Grosse, "Intervalence Bank Transitions in Tellurium," Phys. Stat. Solidi (b) 55, 527 (1973).

(25) M.S. Bresler, I.I. Farbstein, D.V. Mashovets, Yu. V. Kosichkin, and V.G. Veselago, "Phys. Letters A29, 23 (1969).

(26) H. Kohler, "Trigonal Warping of the Valence Band Fermi Surfaces of Tellurium," Phys. Stat. Solidi (b) 65, 603 (1974).

(27) E. Bangert, D. Fischer and P. Grosse, "Intervalence Band Transitions in Tellurium," Phys. Stat. Solidi (b) 59, 419 (1973).

(28) H. Shinno, R. Yoshizaki, S. Tanaka, T. Doi, and H. Kaminimura, "Conduction Band Structure of Tellurium," J. Phys. Soc. Japan 35, 525 (1973).

(29) D. Maltz, M. Pohler, and G. Staupendahl, "Multi-Photon Absorption in Tellurium by Irradiation of CO_2 Laser Pulses," Phys. Stat. Solidi (b) 58, K35 (1973).

(30) W.B. Gandrud and R.L. Abrams, "Reduction in SHG Efficiency in Tellurium by Photoinduced Carriers," Appl. Phys. Letters 17, 302 (1970).

(31) A.C. Walker and D.R. Tilley, "The Photon Drag Tensor in p-type Germanium," J. Phys. C 4, L376 (1971).

(32) A.C. Smith, J.F. Janak, and R.B. Adler, "Electronic Conduction in Solids," (McGraw-Hill, 1967).

(33) R.S. Caldwell and Y.H. Fan, "Optical Properties of Tellurium and Selenium," Phys. Rev. 114, 664 (1959).

(34) B.F. Levine, "Calculation of the Direct Acoustically Induced Optical Harmonic Generation Coefficient," Phys. Rev. Lett. 30, 171 (1973).

(35) V.V. Lemanov and N.K. Yushin, "Nonlinear Effects in the Propagation of Elastic Waves in Piezoelectric Crystals," Sov. Phys. Solid State 15, 2140 (1974).

(36) A.A. Grinberg, D.S. Bulyanitsa, and E.Z. Imamov, "Drag Current Due to the Momentum of Photons Participating in Interband Optical Transitions," Sov. Phys. Semiconductors 7, 29 (1973).

(37) P.M. Valov, B.S. Ryvkin, S.M. Ryvkin, E.V. Titova, and I.D. Yaroshetskii, "Drag of Electrons by Photons in the Photoionization of Impurity Centers," Sov. Phys. Semiconductors 5, 1545 (1972).

(38) J. Auth, D. Genzow, K.H. Herrmann, and M. Wendt, "Anisotropic Photon Drag in p-Type Tellurium," Proc. XII Int. Conference on the Physics of Semiconductors, Stuttgart, 1974 (B.G. Teubner, Stuttgart, 1974), p. 1252.

(39) S. Panyakeow, J. Shirafuji and Y. Inuishi, "Efficient Photon Drag Detector Using p-Type Tellurium," J. Japan Soc. Appl. Phys. 42, 227 (1973); also, "High-performance Photon Drag Detector for a CO_2 Laser Using p-Type Tellurium," Appl. Phys. Lett. 21, 314 (1972).

(40) J. Auth, D. Genzow, K.H. Herrmann, and M. Wendt, "Longitudinal Photon Drag in p-Type Tellurium," Phys. Stat. Solidi (b) 65, 293 (1974).

(41) Robert L. White, "Basic Quantum Mechanics," (McGraw-Hill, 1966) Chap. 11.5.

(42) E.Z. Imamov, "Theory of the Drag of Holes by Photons in Semiconductors with Cubic Symmetry," Sov. Phys. Semiconductors 6, 1462 (1973).

(43) D. Hardy and C. Rigaux, "Optical and Magnetooptical Studies of the Interband Transitions of Holes in Tellurium," Phys. Stat. Solidi 38, 799 (1970).

(44) A.A. Grinberg, "Theory of the Photoelectric and Photomagnetic Effects Produced by Light Pressure," Sov. Phys. JETP 31, 531 (1970).

(45) C.H. Champness, "Calculation of Intrinsic Carrier Concentration in Tellurium Taking Anisotropy into Account," Can. J. Phys. 54, 967 (1976).

(46) I.P. Zhad'ko, L. S. Solonchuk, and Yu. G. Yurov, "Combined Investigation of Transverse Dember Effect and Photomagnetic Effect in Tellurium Single Crystals," Sov. Phys. Semiconductors 8, 65 (1974).

(47) D. Genzow, K.H. Herrmann, and R. Vogel, "Photoconductivity of Tellurium by CO_2 Laser," Phys. Stat. Solidi (A) 23, 51 (1974).

(48) E.M. Conwell, "High Field Transport in Semiconductors," Solid State series (Academic Press, 1967).

(49) A.F. Gibson and A.C. Walker, "Sign Reversal of the Photon Drag Effect in p-Type Germanium," J. Phys. C: Solid State Phys. 4, 2209 (1971).

(50) N. A. Brynskikh, A.A. Grinberg, and E.Z. Imamov, "Classical Theory of the Drag of Free Carriers by Photons," Sov. Phys. Semiconductors 5, 1516 (1972).

(51) A.S. Baltenkov, N.A. Brynskikh, V.B. Gilerson, and N.I. Kramer, "Photon Drag of Free Carriers Interacting with Phonons and Impurity Centers," Sov. Phys. Semiconductors 4, 1589 (1971).

(52) V.G. Agafonov, P.M. Valov, B.S. Ryvkin, and I.D. Yaroshetskii, "Drag of Electrons by Photons in Intraband Absorption of Light by Free Carriers in $A^{III}B^{V}$-Type Semiconductors," Sov. Phys. Semiconductors 6, 783 (1972).

(53) J.H. Yee, "Theory of Photon-Drag Phenomena in Polar and Piezoelectric Crystals," Optics Communications 6, 333 (1972).

(54) A.F. Gibson, M.F. Kimmitt, and A.C. Walker, "Photon Drag in Germanium," Procv X Int. Conf. Phys. Semicon., Cambridge, Mass. 1970. p. 690.

(55) W. Bohmeyer and W. Hoerstel, "High-Field Hall Effect in Extrinsic and Intrinsic Tellurium at Room Temperature," Phys. Stat. Solidi (a) 25, 489 (1974).

(56) G. Ribakovs and A. Gundjian, "Proposed Measurement of the Acoustoelectric Effect of Electron-Photon-Phonon Interaction for Hypersonic Phonons in Semiconductors," J. Acoustic Society of America 52, 1385 (1972).

(57) H. Hattori, M. Umeno, T. Timbo, O. Fujitani, and S. Miki, " Anisotropic Properties of Photon Drag Effect in p-Type Germanium," J. Phys. Soc. Japan 35, 826 (1973).

(58) K.H. Herrmann and R. Vogel, "CO_2 Laser Induced Photo-Effects in Tellurium," Proceedings of the Eleventh Int. Conference on the Physics of Semiconductors, Warsaw, 1972 (Polish Scientific Publishers, Warsaw, 1972), p. 870.

(59) C.R. Hammond, J.R. Jenkins, and C.R. Stanley, "Optical Rectification in Tellurium from 10.6μ," Opto-Electronics 4, 189 (1972).

(60) J.M. Doriak and S. Kothari, "Optical Rectification and Photon Drag in p-Type GaAs at 10.6μ and 1.06μ," Proceedings of the Twelfth Int. Conference on the Physics of Semiconductors, Stuttgart, 1974 (B.G. Teubner, Stuttgart, 1974), p. 1257.

(61) M. Blass, P.A. Franken, and J.F. Ward, "Optical Rectification," Phys. Rev. 138, A534 (1965).

(62) G. Cachier, "Laser Excitation of Microwave Sound in Solids," J. Acoustical Society of America 49, 974 (1969).

(63) B.A. Auld, "Acoustic Fields and Waves in Solids," Vol. 1 (John Wiley & Sons, New York, 1973) p. 102.

(64) P.N. Butcher and T.P. McLean, "The Non-Linear Constitutive Relation in Solids at Optical Frequencies," Proc. Phys. Soc. 81, 219 (1963).

(65) B. Tell, "Piezoelectric Ultrasonic Harmonic Generation in Cadmium Sulfide," Phys. Rev. 136, A772 (1964).

(66) R. Mauro and W.C. Wang, "Acoustoelectric Interactions in Piezoelectric Semiconductors," Phys. Rev. B, 1, 683 (1970).

(67) A. Arnaud, M. Fink and G. Quentin, "Movement of Acoustoelectric Domains in Tellurium in the Temperature Range (77 K - 250 K)," Phys. Letters 33A, 3, 167 (1970).

(68) H.E. Bommel and K. Dransfeld, "Excitation and Attenuation of Hypersonic Waves in Quartz," Phys. Rev. 117, 1245 (1960).

(69) G. Dresselhaus and M.S. Dresselhaus, "Electron and Phonon Dispersion Relations in Tellurium," Proceedings of the Tenth Int. Conference on the Physics of Semiconductors, Cambridge, Mass. 1970, p. 338.

(70) P.H. Carr, "Harmonic Generation of Microwave Phonons by Radiation Pressure and by Phonon Phonon Interaction," IEEE Trans. Sonics and Ultrasonics 13, 103 (1966).

(71) Zadeh and Desoer, "Linear System Theory," (McGraw-Hill 1963), Appendix A2.